Spring 2018

Analysis of DC microgrids as stochastic hybrid systems

Jacob Andreas Mueller

Department: Electrical and Computer Engineering

ANALYSIS OF DC MICROGRIDS AS STOCHASTIC HYBRID SYSTEMS

by

JACOB ANDREAS MUELLER

A DISSERTATION

Presented to the Graduate Faculty of the

MISSOURI UNIVERSITY OF SCIENCE AND TECHNOLOGY

In Partial Fulfillment of the Requirements for the Degree

DOCTOR OF PHILOSOPHY

in

ELECTRICAL ENGINEERING

2018

Approved by

Jonathan Kimball, Advisor
Mariesa Crow
Mehdi Ferdowsi
Bruce McMillin
Pourya Shamsi

PUBLICATION DISSERTATION OPTION

This dissertation consists of the following four articles which have been submitted for publication, or will be submitted for publication as follows:

Paper I: Pages 15–53 have been accepted by IEEE Transactions on Power Electronics.

Paper II: Pages 54–80 have been submitted to IEEE Transactions on Power Electronics.

Paper III: Pages 81–115 have been accepted by IEEE Transactions on Smart Grid.

Paper IV: Pages 116–148 are intended for submission to IEEE Transactions on Control Systems Technology.

ABSTRACT

A modeling framework for dc microgrids and distribution systems based on the dual active bridge (DAB) topology is presented. The purpose of this framework is to accurately characterize dynamic behavior of multi-converter systems as a function of exogenous load and source inputs. The base model is derived for deterministic inputs and then extended for the case of stochastic load behavior. At the core of the modeling framework is a large-signal DAB model that accurately describes the dynamics of both ac and dc state variables. This model addresses limitations of existing DAB converter models, which are not suitable for system-level analysis due to inaccuracy and poor upward scalability. The converter model acts as a fundamental building block in a general procedure for constructing models of multi-converter systems. System-level model construction is only possible due to structural properties of the converter model that mitigate prohibitive increases in size and complexity.

To characterize the impact of randomness in practical loads, stochastic load descriptions are included in the deterministic dynamic model. The combined behavior of distributed loads is represented by a continuous-time stochastic process. Models that govern this load process are generated using a new modeling procedure, which builds incrementally from individual device-level representations. To merge the stochastic load process and deterministic dynamic models, the microgrid is modeled as a stochastic hybrid system. The stochastic hybrid model predicts the evolution of moments of dynamic state variables as a function of load model parameters. Moments of dynamic states provide useful approximations of typical system operating conditions over time. Applications of the deterministic models include system stability analysis and computationally efficient time-domain simulation. The stochastic hybrid models provide a framework for performance assessment and optimization.

ACKNOWLEDGMENTS

First and foremost I would like to thank my advisor, Dr. Jonathan Kimball, for always knowing exactly what I needed to hear at exactly the moment I needed to hear it. He has been a formational influence in my life, both personally and professionally. Without his support none of this would be possible.

I am also grateful to the rest of my committee, all of whom have provided useful insights and advice over the past six years.

Several of my peers at Missouri S&T have assisted me in building hardware experiments and collecting results, but none more than Johann Voigtlander. His efforts have significantly improved the quality of this work, and it has been a privilege to work with him.

This work was funded by the National Science Foundation, award 1406156, and by a fellowship from the NASA-Missouri Space Grant Consortium.

Finally, I am grateful to my family for their patience, encouragement, and understanding. I am especially thankful for Kelsey and Finn, who stayed by my side for every step of this journey. When I was lost, when I was tired, and when I was trapped by my own doubts, their companionship kept me moving forward. They turned every insurmountable obstacle into just another adventure.

TABLE OF CONTENTS

Page

LIST OF ILLUSTRATIONS

LIST OF TABLES

SECTION

1. INTRODUCTION

1.1. OVERVIEW

Power electronics are indispensable components of modern power systems. The range of applications for power electronic energy conversion is constantly expanding, driven by advances in semiconductor technology. Power electronic interfaces are the connective elements behind smart grids [1], microgrids [2], transportation electrification [3], and dc power systems [4, 5]. However, converter circuits and control systems are inherently nonlinear, and accurate models of their behavior are complex. When constructing models of multi-converter systems, it is often difficult to obtain a usable balance of accuracy and complexity. In some cases, tractable system-level representations are not possible without simplifying assumptions that affect model validity. These challenges exist at the intersection of power electronics and power systems, and require solutions that draw on methods from both disciplines.

The objective of this work is develop accurate and computationally efficient models of dc microgrids and distribution systems. Systems based on the dual active bridge (DAB) topology are the specific focus. The modeling challenges for DAB converters are emblematic of larger fundamental problems in modeling multi-converter systems. While DAB converters are used in all the systems under consideration, the system-level modeling solutions apply equally to other dc-dc converter topologies. The final models are intended for system-level design and analysis tasks, namely time-domain simulation, stability assessment, and performance optimization.

Time-domain simulation is an important tool in power system analysis. For conventional power systems, simulation consists of numerical integration of a nonlinear, large-signal model [6, 7]. Simulation of power electronics is more complex due to the inherent discontinuities of switched-mode converters. The most accurate simulations involve switched models, wherein the active switch configuration determines the model used in the integration routine [8, 9, 10]. However, discontinuities at switch transitions cause complications for numerical integration algorithms, ranging from difficulties in step size selection to numerical convergence issues [11]. As a result, switching simulations are slow, and scale poorly with the number of switched-mode devices in a given system [12, 13]. To address this issue, the average modeling approach (both in the classical low-frequency and generalized sense) consolidates models associated with each switch configuration into a single representation [14, 15, 16, 17]. The averaging process eliminates switching discontinuities and improves the efficiency of numerical simulations [13, 12, 18]. However, averaging introduces an approximation, which may affect the accuracy of the final model [19, 12]. Average models of DAB converters are affected by errors due to averaging [20, 21]. To produce accurate and efficient system-level models, these errors must be eliminated without increasing model complexity.

Small-signal stability assessment is another essential analysis task. Small-signal stability of dc systems is typically assessed by comparing converter input and output impedances [22, 23, 24, 25, 26, 27]. Impedance critera do not require a full system-level model, but become increasingly complicated as the number of connections between converters increases. Moreover, for some converters, such the DAB converter, straightforward impedance expressions are not always possible [28]. In power system analysis, small-signal stability is assessed by linearizing a system model and inspecting eigenvalues [29, 7]. This is a more flexible and scalable approach, but it requires a system-level model.

Performance optimization is a more open-ended task, but equally relevant to both power electronics and power systems. In this context, performance optimization refers to system design practices or control strategies that maximize some performance metric (e.g. overall efficiency) or minimize some cost (e.g. total loss). When the mechanism through which rewards (or costs) are incurred depends on the operating conditions of the system, the process of constructing and solving an optimization problem requires quantitative descriptions of the range of system operating conditions. These descriptions necessarily involve detailed characterization of sources of uncertainty. For the systems under consideration, uncertainty is introduced through load and source behavior. In order to assess and improve system performance, load and source randomness—and the effect of random behavior on system operation—must be properly specified.

Solutions to the problems above are presented here in four papers, organized as follows. The first two papers focus on the derivation of accurate and computationally efficient dynamic models with deterministic load and source inputs. Paper I describes improvements to generalized average models of dc-dc DAB converters. Paper II extends the modeling improvements to multi-converter systems, and introduces a new harmonic reconstruction method for predicting transformer currents. The second half of the dissertation considers the effects of randomness in the load inputs. Paper III presents a method of generating stochastic models of composite electrical loads. The load models are presented as an element of a nonintrusive load monitoring algorithm, but are directly applicable to modeling loads in dc distribution systems as well. In Paper IV, load and microgrid models are joined together using the formalism of stochastic hybrid systems.

The models proposed in Paper I and Paper II describe dynamic behavior of converters and systems as a function of external inputs. In the case of a dc microgrid, the inputs of interest are loads and sources (or simply loads, understood to be possibly bidirectional). Together, Paper III and Paper IV widen the scope of the models to include load behavior.

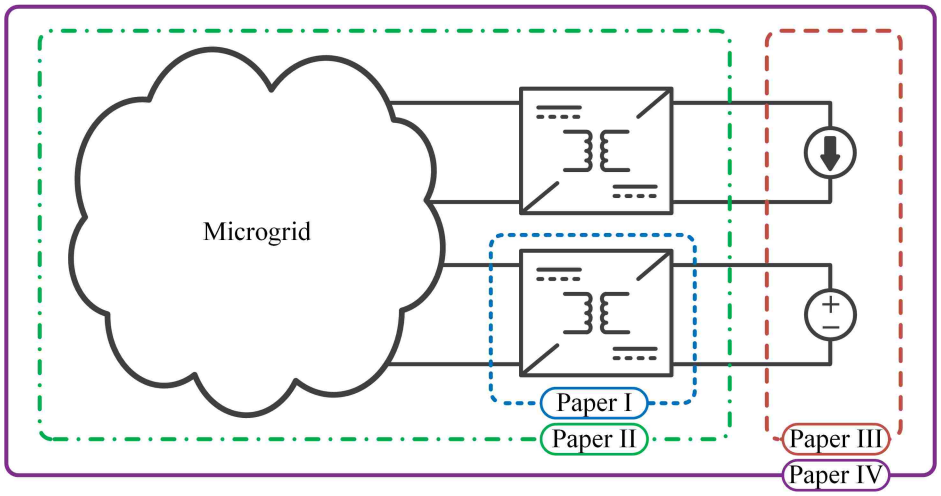

Figure 1.1. Modeling scope for each paper.

Paper III describes a method for building probabilistic load models; Paper IV merges these load descriptions with the deterministic framework established in Paper I and Paper II. A graphical representation of the modeling scope of each paper is shown in Fig. 1.1.

1.2. DETERMINISTIC MICROGRID MODELS

Accurate dynamic models are critical to analysis and design procedures, both for individual converters and full microgrid systems. This section describes challenges involved in modeling DAB converters and the important characteristics of system-level models. Challenges and objectives outlined in this section set the stage for the modeling solutions proposed in Paper I and Paper II.

1.2.1. Dual Active Bridge Converters. The DAB topology [30, 31, 32] consists of two H-bridge circuits separated by a high-frequency transformer. The transformer is the most important component of the converter: the transformer's leakage inductance is the primary energy storage element in the converter and the turns ratio is a significant factor in determining voltage gain. The H-bridge circuits apply modulated voltages on either side of the transformer, such that the transformer current is periodic at the converter switching

frequency. The actual shape of the current waveform is determined by the modulation scheme; a variety of modulation strategies have been proposed to accentuate performance strengths or minimize weaknesses [33]. In the simplest case, square wave voltage pulses with 50% duty ratio are applied on either side of the transformer. The phase shift between the primary and secondary voltages determines the power transferred through the converter. This is referred to as single phase shift modulation. Alternative schemes, such as dual [34], extended [35], and triple [36] phase shift modulation, improve on single phase shift by reducing circulating currents in the high-frequency transformer.

The DAB topology's high-frequency ac conversion stage is the source of desirable performance characteristics, including galvanic isolation, high power density, soft-switching capabilities, and bidirectionality. Applications of DAB converters follow from these attributes. DAB converters are an attractive solution for applications in which physical size is a primary constraint, such as vehicular power systems. DAB converters have been studied in diverse range of vehicular applications including aerospace [37], automotive [38], and marine power systems [39, 40]. The topology's zero voltage switching capabilities and bidirectionality have led to applications in smart grids and conventional power systems [41]. The DAB has also been identified as a candidate topology for solid state transformers [42, 43, 44]. These applications all share a common element: the DAB converter is used as one element of a larger integrated system. Almost all important and emerging applications of dc-dc DAB converters are in systems that may broadly be classified as dc microgrids.

1.2.2. DAB Models. This research is concerned with the development of useful models. A successful model should accurately describe the dynamic behavior of the converter as a function of external influences. Beyond this basic functionality, though, the performance characteristics and applications of the DAB topology help to identify some important model attributes. The DAB converter is flexible with respect to modulation schemes. Bearing this flexibility in mind, it is clear that a useful DAB model should

support different modulation strategies without significant rederivation. Furthermore, in consideration of the important applications of the topology, a useful DAB model should mesh seamlessly with high-level representations and support system analysis tasks.

The source of the DAB topology's modeling challenges is the high-frequency ac conversion stage. The most common approach to modeling power electronics is classical average modeling [45, 46]. In classical average modeling, state variables are represented by sliding averages taken over a single switching period [16, 15]. This approach assumes that dynamic states can be described by low-frequency averages, a condition commonly referred to as the "small-ripple" approximation. Since transformer current in a DAB converter is ac, the small-ripple approximation does not hold, and classical average modeling does not apply. Nonetheless, classical average models of DAB converters have been proposed. In [47], a reduced order model of a DAB converter was derived through classical average modeling. The reduction in model order is due to the transformer current state: since the average of the transformer current over a switching period is zero, the current state is eliminated from the average model. However, eliminating the transformer current state removes dynamic infuence of the leakage inductance from the model. Since the leakage inductance is the primary energy storage element of the DAB converter, the accuracy of the reduced order model is affected, particularly at higher frequencies. Classical average modeling was also applied in [20], but instead of eliminating the current state, the entire dual H-bridge block was treated as a single element. Algebraic equations were derived for the average currents flowing into and out of the H-bridge circuits. While this approach includes the effects of transformer parameters in the final model, the average current expression are complicated and nonlinear. As a result of this nonlinearity, small-signal models derived from the approach in [20] lose accuracy at high frequency. More importantly, the derivation is specific to single phase shift modulation. Extensions to advanced modulation schemes would require significant rederivation.

Other modeling efforts have considered more powerful modeling tools to address the deficiencies of classical average DAB models. The sampled-data modeling method from [48] was applied to DAB converters in [49, 50, 38]. This method assumes that the converter transitions cyclically through a set of fully characterized switching modes. Explicit descriptions of each mode and a prespecified base period are required for this approach. Of the existing DAB models, those derived using the sampled-data modeling approach are the most accurate [20]. However, the price of this accuracy is model complexity: each switch configuration is modeled independently. The additional switch configurations present in advanced modulation schemes increase model complexity, and the transitions through switching modes are dependent on the modulation scheme. As a result, new modulation schemes essentially require entirely new models. The most significant problem, however, is how model size and complexity increases for models of multi-converter systems. The modeling requirements–full characterizations of all switching modes and a system-wide base period–quickly become unreasonable as the number of converters included in the system increases.

Another approach to modeling DAB converters employs the generalized average modeling (GAM) [17, 51] framework. GAM generalizes the approach of classical average modeling by expanding state variables into Fourier series components before applying the sliding average operation. An open-loop DAB model derived using GAM was proposed in [21]. The model from [21] is central to this dissertation. All of the improvements and extensions described in the following sections belong to a modeling genealogy that starts with [21].

Like sampled-data modeling, GAM is subject to significant scalability issues. GAM requires the specification of a base period, and involves an inherent tradeoff between accuracy and model complexity [52, 46]. To ensure tractability in the final model, Fourier series expansions of state variables are typically truncated after the first harmonic [21, 53], a practice commonly referred to as the first harmonic approximaton. This approach avoids

prohibitive model complexity but limits accuracy. In particular, DAB models derived with the first harmonic approximation are affected by persistent large-signal error. These errors are especially problematic at the system level, since small errors in bus voltage lead to incorrect power flow predictions. A correction factor was proposed in [53] to eliminate the error, but only for single phase shift modulation. Even in operating regions where the large-signal error has minimal effect, the transformer current predictions of GAM-based models are limited in accuracy. When ac states are limited to first harmonic terms, transformer currents are represented as sinusoids at the switching frequency. Sinusoidal approximations poorly represent the complicated piecewise exponential waveforms observed in simulations and hardware experiments. These deficiencies would seem to preclude the use of GAM for system-level models. However, all of these issues may be addressed through model improvements and manipulations.

1.2.3. Development of a System-Level Model. The most important characteristics of a system-level model are accuracy, scalability, and modularity. The importance of accuracy and scalability are straightforward, but modularity is equally critical. In this context, modularity refers to the ability to combine, separate, and reconfigure the system-level model without requiring full rederivation. That is, when a converter is added to the system, the adjustment to the system-level model should only require operations that act on the existing system model and the model of the newly added converter. Models derived using classical averaged modeling are inherently modular [18, 12]. However, other methods do not guarantee modularity. Both GAM and sampled-data modeling involve the specification of a system-wide base period. If the base period changes when a converter is added to the system, both of these modeling approaches will require ground-up rederivation.

Previous studies have considered the development of system-level models using GAM [54, 55, 39, 56, 57]. The authors of [56] observe that GAM does not naturally support multi-converter systems, and propose an extended averaging scheme that allows for the inclusion of multiple switching frequencies. This approach makes it possible to accurately

model multiple switching frequencies at the cost of complexity: for a system with N states and M dominant harmonics, the final model will include $N(2M-1)$ state equations. A more scalable solution is described in [54]. The approach in [54] involves selecting the number of Fourier series components on a state-by-state basis, rather than setting a globally-consistent number of terms. This "selective averaging" approach assumes preexisting knowledge of dominant system dynamics. To mitigate complexity, dynamic interactions between converters are assumed to exist entirely in dc average states. In relation to the methods here, selective averaging produces the same level of reduction in model complexity. However, the methods described in Paper II achieve this reduction through structural properties of the individual converter models and require no assumptions on the nature of system dynamics.

In summary, two fundamental problems obstruct models of multi-converter systems containing DAB converters. The first problem is the inherent tradeoff between accuracy and model complexity in GAM. Approximations necessary obtain tractable models, namely the first harmonic approximation, limit large-signal accuracy. As a result, the models are not suitable for time-domain simulation or load flow analysis. The second problem is the requirement of a system-wide base period, which prevents modular approaches to system-level modeling. The contributions of Paper I and Paper II are solutions to these two fundamental problems. Paper I introduces a correction factor that eliminates the large-signal error due to the first harmonic approximation without including additional Fourier series terms as dynamic states. Moreover, the existing GAM-based DAB model is extended for general modulation schemes. Paper II addresses frequency dependence and proposes a modular procedure for generating models of multi-converter systems. A decoupling between state variables of the DAB converter, originally noted in [21], is preserved through the model construction process. Because of this decoupling effect it is possible to represent interactions between converters with dc average terms only, eliminating the the need for a system-wide base period. Converter and system models derived using the methods from

Paper I and Paper II are suitable for stability assessments and load flow analyses. Their most important feature, though, is that they enable accurate time-domain simulation at a fraction of the computational cost of switched model alternatives.

1.3. INFLUENCE OF PRACTICAL LOADS

A common approach in modeling power electronics is to represent loads as either fixed impedances or constant voltage/current sources. The parameters of these elements are then defined according to maximum/minimum load power values. This load representation is a practical choice for many anaysis and design objectives, particularly when scope is limited to an individual converter. For instance, simplified load models are useful for analyzing performance under worst-case conditions, where converters are most likely to encounter stability issues. However, as systems increase in size, analysis and design practices based on simplified worst case conditions become less useful. In a system with many independent loads, the likelihood that all loads simultaneously operate at maximum power is small, and designing the system to meet this rare condition is not a viable option. The same situation occurs in conventional power systems, and has motivated a variety of probabilistic load modeling solutions.

Another disadvantage of deterministic load models is that they offer no insight on typical operating conditions over time. Specifications of 'typical' behavior require descriptions of a probabilistic nature. The ability to quantify typical conditions—and the possible deviations from these conditions—is a valuable analytical tool. Many aspects of converter performance depend on system operating conditions. Converter efficiency is perhaps the most obvious (and most important). Another example, one which is particularly relevant to the DAB topology, is zero voltage switching (ZVS). ZVS occurs in a subset of the possible operating space of a DAB converter, but has significant effect on switching loss and semiconductor stresses [31, 37]. It is therefore desirable to operate the converter in the ZVS region whenever possible. More generally, a microgrid may be stable and functional

over a wide range of operating conditions, but it is unlikely that all stable conditions are equally desirable. For a given operating-point-dependent metric (e.g. efficiency, stability margins, power quality, etc.), specifications of typical operating conditions make it possible to assess the actual performance of the system.

The process of obtaining probabilistic operating point descriptions can be broken into two subproblems: modeling practical load behavior and connecting load models to dynamic states. These problems are addressed in Paper III and Paper IV, respectively. Including stochastic load descriptions in the modeling framework is challenging task and requires a more diverse set of tools than used in deterministic modeling efforts. Many of these tools, such as the machine learning algorithms in Paper III and stochastic calculus in Paper IV, are far removed from the skills normally associated with analysis and design of power electronics. The driving motivation behind both of these papers is to provide models and methods which are accessible to practicing engineers. Consequently, in comparison to the first two papers, Paper III and Paper IV include more examples, simplifications, and details related to practical implementation.

1.3.1. Load Modeling. Load modeling is a mature subfield of conventional power system analysis. In large power systems, it is possible to rely on Gaussian process models based on the central limit theorem [58, 59, 60]. Gaussian models are high-level abstractions that apply when loads consist of many individual devices. However, as the size of a system decreases, contributions of a single device become more significant with respect to the total load profile, and Gaussian approximations become less accurate [61].

For loads that do not meet the criteria for Gaussian approximations, i.e. loads that consist of a small number of devices, an alternative strategy is to build models upward from individual device level. This approach is used in nonintrusive load monitoring (NILM) [62, 63, 64]. The objective of NILM is to extract individual device activity from measurements of a composite load profile. To support this extraction, or disaggregation, composite load models must retain the individual characteristics of their constituent devices.

Paper III describes a full NILM procedure. The loads are represented by hidden Markov models (HMMs). HMM-based methods are a particularly successful subset of NILM [65, 66, 67, 68, 69]. The most important contribution of Paper III, in the context of modeling microgrid loads, is the process of constructing models of individual devices and combining them into models of the composite load. In particular, the load modeling approach outlined in Paper III is directly applicable to generating 'typical' load specifications based on either composite load measurements or knowledge of the devices contained in the load.

The scope of Paper III is defined to include "systems of known devices," or systems for which number and nature of loads is fully known. In residential systems, the original target applications of the NILM concept, complete knowledge of system loads is impractical. However, the "known device" criterion is commonly met in dc microgrids and distribution systems. In particular, the criterion is satisfied by industrial systems designed to support a specific set of equipment, and it is inherently met by vehicular power systems. Removing the possibility of unknown devices makes it possible to explore new NILM applications without solving the problem of unmodeled loads. For instance, Paper III proposes a method of device-level energy use estimation that significantly improves on the performance of previous HMM-based algorithms.

The load representations in Paper III are discrete-time HMMs based on steady-state conditions. These models only characterize the randomness in load behavior; they offer no description of load influence on the local power system. In order to describe the effects of load behavior on the system, the stochastic load models must be joined together with the dynamic models proposed in Paper II. The ideal result of a combined model would be closed-form distributions of dynamic states. However, it is only possible to produce full distributions for a very narrow set of circumstances, such as linear systems with Gaussian

inputs [70]. In the present case, dynamic models are nonlinear and load models are not Gaussian, so more powerful modeling methods must be employed to characterize stochastic dynamic behavior.

1.3.2. Stochastic Hybrid System. Stochastic hybrid systems (SHSs) are a general class of stochastic process that include continuous dynamics, instantaneous events, and a wide variety of random effects [71]. The SHS framework is challenging due to its sheer generality (see [72] for a review of models that fall within the SHS scope). However, SHS models provide powerful tools for system analysis. In particular, SHS models describe the evolution of moments of dynamic state variables. Moments provide useful descriptions of dynamic state behavior in lieu of full state distributions.

Previous studies have used SHS models to describe power delivery systems. In [73], the SHS framework was applied to a conventional power system. SHS models of microgrids have been proposed for the purposes of simulation [74] and stability analysis [75]. Although the application is different, the approach used here is heavily influenced by these previous efforts, particularly [73]. The model in [73] consists of an affine power system model and an input process described by a continuous-time Markov chain (CTMC). Key elements of the SHS, namely test functions and reset maps, are defined in [73] such that the equations which describe moment dynamics depend only moments of equal or lower order. The same definitions are used here, and they affect the same simplification. Additionally, [73] describes a general procedure for calculating moments of algebraic states. This procedure forms the basis for a new set equations that encode ZVS conditions into the SHS model.

Paper IV describes an SHS model of a dc microgrid system. The model consists of a CTMC, which is constructed from the stochastic load models in Paper III, and a family of affine microgrid models, which are derived according to the methods in Paper II. The SHS framework is applied according to [71] using the test function and reset maps proposed in [73]. Since the objective of the paper is to provide an accessible tool for practicing engineers, the general forms resulting from the methods of [71] and [73] are

further simplified. In particular, closed-form expressions are derived for the systems of equations that describe first and second moment dynamics. This simplification makes it possible to construct the full SHS model through linear operations. The simplified form also provides useful insights into the relationships between moments and load process parameters.

Paper IV also considers the practical problem of assessing ZVS performance for DAB converters in multi-converter systems. First, ZVS conditions are introduced in the SHS model as functions of the stochastic dynamic state processes. Analytic expressions for the moments of these functions are then derived. Moments of the ZVS condition functions are used to approximate the probability of ZVS for a given set of loads. While the expressions apply for moments of any order, low order moments provide sufficiently accurate approximations in practice. First and second order moments provide enough information to define upper and lower bounds on ZVS probability. The ZVS performance analysis in Paper IV addresses a practical issue specific to single phase shift modulated DAB converters. More importantly, though, the assessments serve as an example of the more general applications of an SHS model.

PAPER

I. AN IMPROVED GENERALIZED AVERAGE MODEL OF DC-DC DUAL ACTIVE BRIDGE CONVERTERS

Jacob A. Mueller and Jonathan W. Kimball

Department of Electrical & Computer Engineering

Missouri University of Science and Technology

Rolla, Missouri 65409–0050

Email: jam8z4@mst.edu

ABSTRACT

Improvements are proposed for generalized average models of dual active bridge (DAB) converters. Generalized average modeling involves a trade-off between accuracy and tractability. To maintain an acceptable level of complexity, existing DAB models are derived using a first harmonic approximation. These models provide accurate small-signal representations, but are limited as large-signal analysis tools due to persistent steady-state error. This study proposes a modeling framework that provides accurate large and small-signal models without significant increases in overall complexity. The framework describes DAB operation with triple phase shift modulation, and is easily simplified for single, dual, or extended phase shift modulation schemes. The special case of single phase shift modulation, which experiences the most significant large-signal error, is given additional consideration. The framework is applied to open and closed-loop operation, and both large and small-signal models are discussed. Models are validated in simulation and hardware experiments using a small scale DAB prototype.

Keywords: average modeling, dual active bridge converter, generalized average model, phase shift modulation

1. INTRODUCTION

The dual active bridge (DAB) topology features desirable performance characteristics including galvanic isolation, high power density, low device stresses, and bidirectional operation [1, 2]. Many of these attributes are due to a high-frequency ac conversion stage. However, the associated ac state variables present challenges when developing models of the converter's behavior. In particular, the transformer current state precludes the "small-ripple" approximation commonly employed in traditional modeling approaches, e.g. state-space averaging and average circuit modeling.

Previous studies have addressed the challenges of modeling DAB converters. The most common strategy uses the sampled-data modeling procedure from [3] to develop discrete-time models. This approach was used in [4] to develop an open-loop DAB model, and again in [5] to develop a more detailed model consisting of a converter, EMI filters, and control system. In these models, the converter transitions through discrete modes of operation, each described by a set of linear time-invariant ordinary differential equations (ODEs). The transition times are either explicitly controlled (e.g. by gate driver signals) or implicitly determined by device thresholds (e.g. by diode current zero crossings). The state solution within each mode is explicitly determined by initial conditions at transition times and state transition matrices consisting of matrix exponentials. In [6], matrix exponential calculations were avoided through the use of bilinear approximations, leading to a simplified discrete-time DAB model.

The advantage of the discrete-time models in [4, 6, 5] is that they explicitly describe state trajectories in all subintervals of converter operation, meaning they are capable of providing exact solutions for ac state variables. In the case of DAB converters, these models are able to accurately predict transformer currents and, as in [4], the current zero crossings

critical to zero voltage switching (ZVS) [7]. The capabilities of discrete-time representations notwithstanding, two factors motivate the development of accurate continuous-time models. First, continuous-time models are still preferred for control design due to the prevalence of simple and powerful design tools. Secondly, DAB converters are well-suited to applications in multi-converter systems, such as solid state transformers [8], microgrids, and dc distribution systems. The framework of [3] assumes cyclic transitions through fully characterized modes of operation, and is not intended to produce models that are modular elements of a larger system. Representing all possible switching modes at the system level quickly becomes infeasible as the number of converters increases. Moreover, differences in converter switching frequencies make it difficult to define a usable system-wide base period. For the purposes of system-level analysis, more scalable alternatives are required.

Continuous-time DAB models have been proposed as well. The simplest model, proposed in [9], essentially results from the application of classical state-space averaging [10]. Since the dc average of transformer current is 0, the state is eliminated in the averaging process, and its dynamics are lost in the final model. A more detailed approach was used in [11] to derive both large and small-signal average models. The ac stage in these models is represented by half period averages of the dc currents into and out of the H-bridges. This allows the models to incorporate effects of transformer core and conduction losses, which are omitted from the models in [9]. A similar procedure was used in [12] for the purposes of steady-state analysis.

A continuous-time DAB model was derived using generalized average modeling (GAM) in [13]. In GAM, state variables are expanded into Fourier series terms at multiples of the converter switching frequency [14], providing straightforward representations of ac states. However, the GAM framework involves a trade-off between accuracy and complexity. Specifically, both accuracy and complexity increase with the number of Fourier series terms included in the model. The model in [13] uses a first harmonic approximation, and truncates the Fourier series at the first harmonic. When linearized, the model accurately

predicts small-signal responses, but the large-signal model is inaccurate at steady-state. The accuracy of the model increases when more Fourier series terms are included (see e.g. [15]), but the number of model states increases rapidly with the number of Fourier series terms considered, so even small accuracy gains require substantial penalties in terms of model complexity.

This steady-state error was previously noted in [11], and a method of correcting the error was proposed [16]. The approach in [16] consists of applying a multiplicative correction factor to the load and state variables. However, the correction factor is only derived for single phase shift operation. Furthermore, the method assumes lossless operation, and neglects the effect of transformer winding resistance, which may be significant in practice. This copper loss is particularly important for single phase shift operation, which produces large circulating currents, or when the ratio of winding resistance to leakage reactance is high [12].

This study presents the following contributions:

- The DAB model from [13] is extended to more general modulation strategies, including dual, extended, and triple phase shift modulation. Both large and small-signal models are described.

- A new method of eliminating the error caused by truncating the Fourier series at the first harmonic is proposed. The method involves deriving the relationship between the equilibrium solution to the model equations and exact steady-state expressions, and then including those relationships in the model itself.

- An additional correction factor that includes copper losses in the transformer is derived for the special case of single phase shift modulation.

The structure of the paper is as follows. Section 2 briefly reviews the DAB model from [13] and describes the steady-state model error in precise terms. The improved DAB model is given in Section 4, starting with the extension to more general modulation

strategies, and then including the large-signal error correction. Model partial derivatives, including those necessary to develop small-signal models, are given in Section 4. Special consideration is given to the single phase shift case in Section 5, including the derivation of a lossy correction factor. Verification experiments are described in Section 6.

2. BACKGROUND

This section reviews the DAB model from [13] to be improved in the following section, establishes important terms and notation, and provides a mathematical description of the steady-state error problem.

2.1. Original DAB Model. The original DAB model proposed in [13] begins with

$$\dot{v}_o = \frac{-1}{R_{sh}C_o}v_o + \frac{1}{C_o}i_t s_2(\tau, d) - \frac{1}{C_o}i_L \tag{1}$$

$$\dot{i}_t = \frac{1}{L_t}v_{in}s_1(\tau, d) - \frac{1}{L_t}v_o s_2(\tau, d) - \frac{R_t}{L_t}i_t \tag{2}$$

where dot notation is used to indicate derivatives with respect to time. The signals and parameters in these equations are identified in Fig. 1. All hardware parameters are referred to the secondary side of the transformer. For simplicity, the derivation shown here assumes a 1:1 turns ratio. The only modification necessary to include non-unity turns ratios in the model is to replace all appearances of v_{in} with $\frac{n_2}{n_1}v_{in}$. This is true for this model and for the models proposed in the following section.

Switching signals $s_1(\tau, d)$ and $s_2(\tau, d)$ are the switching signals that drive the input and output H-bridges, respectively. The model from [13] was derived for single phase shift modulation. For time τ in a switching interval ($0 \leq \tau < T$) and phase shift argument d, the single phase shift switching signals are

$$s_1(\tau, d) = \begin{cases} 1, & 0 \leq \tau < \frac{T}{2} \\ -1, & \frac{T}{2} \leq \tau < T \end{cases} \tag{3}$$

$$s_2(\tau, d) = \begin{cases} 1, & \frac{dT}{2} \le \tau < \frac{dT}{2} + \frac{T}{2} \\ -1, & 0 \le \tau < \frac{dT}{2} \text{ or } \frac{dT}{2} + \frac{T}{2} \le \tau < T \end{cases} \tag{4}$$

At this point the GAM framework and first harmonic approximation are applied. The following equations include a critical change: the phase shift variable, represented as d in the switching signal definitions, becomes a new variable $\hat{d}$. The reasons for this are discussed in the following subsection, but the change first appears here because it is a direct consequence of the first harmonic approximation. The GAM state equations are

$$\langle \dot{v_o} \rangle_0 = \frac{-1}{R_{sh} C_o} \langle v_o \rangle_0 - \frac{4 \sin \pi \hat{d}}{C_o \pi} \langle i_t \rangle_R - \frac{4 \cos \pi \hat{d}}{C_o \pi} \langle i_t \rangle_I - \frac{\langle i_L \rangle_0}{C_o} \tag{5}$$

$$\langle \dot{i_t} \rangle_R = \frac{2 \sin \pi \hat{d}}{L_t \pi} \langle v_o \rangle_0 - \frac{R_t}{L_t} \langle i_t \rangle_R + \omega_s \langle i_t \rangle_I \tag{6}$$

$$\langle \dot{i_t} \rangle_I = \frac{2 \cos \pi \hat{d}}{L_t \pi} \langle v_o \rangle_0 - \omega_s \langle i_t \rangle_R - \frac{R_t}{L_t} \langle i_t \rangle_I - \frac{2 \langle v_{in} \rangle_0}{L_t \pi} \tag{7}$$

The states of the model are the dc average output capacitor voltage and the real/imaginary components of the fundamental harmonic transformer current. The model inputs are the source voltage, phase shift, and load current. A closed-loop voltage-controlled model, described briefly in [17], includes two additional equations:

$$\langle \dot{\gamma} \rangle_0 = k_i \left(v_{ref} - \langle v_o \rangle_0 \right) \tag{8}$$

$$\hat{d} = k_p \left(v_{ref} - \langle v_o \rangle_0 \right) + \langle \gamma \rangle_0 \tag{9}$$

In the closed-loop model, the phase shift is generated internally by (9) and the input is replaced with voltage reference v_{ref}.

2.2. Origin of Steady-State Error. This section describes the origin of the large-signal modeling error. For simplicity, single phase shift modulation is considered in this discussion, since only one control variable is involved. The analysis applies equally to other modulation strategies.

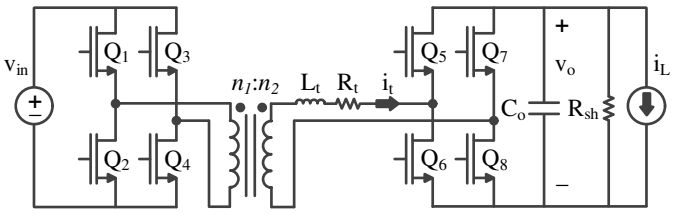

Figure 1. Dual active bridge topology.

The steady-state error manifests differently depending on how the model is used. If a phase shift is specified as an exogenous input (as is the case with the open loop model) the error will affect the output voltage. If an output voltage and load current are specified, the error will affect the phase shift. Similarly, in closed-loop operation, if a voltage reference and load current are specified, the phase shift will be affected.

For simplicity, consider a lossless closed-loop converter with current source load (i.e. $R_t \to 0$, $R_{sh} \to \infty$) in steady-state operation. The action of the controller forces output voltage to the voltage reference at steady-state, so the error will be restricted to the phase shift. The relationship in (7) reduces to $0 = i_t s_2(\tau, d) - i_L$, and the load current can be expanded as an infinite Fourier series:

$$i_L = \sum_{k=-\infty}^{\infty} \langle i_t s_2(\tau, d) \rangle_k = \sum_{k=-\infty}^{\infty} \sum_{i=-\infty}^{\infty} \langle s_2(\tau, d) \rangle_{k-i} \langle i_t \rangle_i \tag{10}$$

Considering only the dc average current, the equation is

$$\langle i_L \rangle_0 = \langle i_t s_2(\tau, d) \rangle_0 = \sum_{i=-\infty}^{\infty} \langle s_2(\tau, d) \rangle_{-i} \langle i_t \rangle_i \tag{11}$$

Switching signal $s_2(\tau, d)$ is a phase-shifted square wave, and only has nonzero Fourier series coefficients at odd harmonics. The coefficients are functions of the phase shift, d.

$$\langle s_2(\tau, d) \rangle_k = \frac{-2 \sin \pi k d}{k\pi} + j \frac{-2 \cos \pi k d}{k\pi} \text{ for } k = 1, 3, \ldots \tag{12}$$

with $\langle s_2(\tau, d)\rangle_{-k} = \langle s_2(\tau, d)\rangle_k^*$. Note that this equation involves functions of d rather than $\hat{d}$, since the first harmonic approximation has not been applied to (7).

Under the same operating conditions, the dc average load current may be determined from the GAM state equations by simplifying and rearranging (5).

$$\begin{aligned}\langle i_L\rangle_0 &= \frac{-4\sin\pi\hat{d}}{\pi}\langle i_t\rangle_R + \frac{-4\cos\pi\hat{d}}{\pi}\langle i_t\rangle_I \\ &= \langle s_2(\tau,\hat{d})\rangle_{-1}\langle i_t\rangle_1 + \langle s_2(\tau,\hat{d})\rangle_1\langle i_t\rangle_{-1}\end{aligned} \tag{13}$$

This expression corresponds exactly to the summation from (11) truncated after $i = \pm 1$, i.e. including the effect of the first harmonic approximation. The value of $\langle i_L\rangle_0$ must be the same in both (11) and (13), since it is specified as a constant, exogenous input. Therefore, the phase shift $\hat{d}$ that satisfies the equilibrium solution of the truncated model equations must be different from the real-world phase shift, d. This is consistent with the observations in both [11] and [16].

The preceding analysis shows that when phase shift is treated as a free variable, a quantifiable difference exists between solutions to the GAM equations and steady-state expressions derived from first principles. In short, the objective of Section 3.2 is to eliminate steady-state error by identifying and correcting for this difference.

3. IMPROVED MODEL

This section describes the derivation of the improved DAB model, starting with an extension to more general modulation schemes. Following the derivation, Sec. 3.2 describes the large-signal error correction. In the interest of notational clarity, the angle-brackets used to denote averaging in the previous section are dropped for the remainder of the paper. The dc average of generic variable x is therefore represented as x_0 rather than $\langle x\rangle_0$. Similarly, real and imaginary components of the fundamental harmonic are $x_R = \langle x\rangle_R$ and $x_I = \langle x\rangle_I$, respectively.

3.1. Modulation Scheme Extension. Applying the GAM framework to (7) and (2) yields

$$\dot{v}_{o0} = -\frac{1}{R_{sh}C_o}v_{o0} + \frac{1}{C_o}i_{t0}s_{20} + \frac{2}{C_o}i_{tR}s_{2R} + \frac{2}{C_o}i_{tI}s_{2I} - \frac{1}{C_o}i_{L0} \tag{14}$$

$$\dot{i}_{tR} = \frac{1}{L_t}v_{in0}s_{1R} + \frac{1}{L_t}v_{inR}s_{10} - \frac{1}{L_t}v_{o0}s_{2R} - \frac{1}{L_t}v_{oR}s_{20} - \frac{R_t}{L_t}i_{tR} + \omega_s i_{tI} \tag{15}$$

$$\dot{i}_{tI} = \frac{1}{L_t}v_{in0}s_{1I} + \frac{1}{L_t}v_{inI}s_{10} - \frac{1}{L_t}v_{o0}s_{2I} - \frac{1}{L_t}v_{oI}s_{20} - \omega_s i_{tR} - \frac{R_t}{L_t}i_{tI}. \tag{16}$$

To prevent saturation of the transformer, switching signals are typically defined such that their dc averages are zero, i.e. $s_{10} = s_{20} = 0$. Under this condition, the equations simplify:

$$\dot{v}_{o0} = -\frac{1}{R_{sh}C_o}v_{o0} + \frac{2}{C_o}i_{tR}s_{2R} + \frac{2}{C_o}i_{tI}s_{2I} - \frac{1}{C_o}i_{L0} \tag{17}$$

$$\dot{i}_{tR} = \frac{1}{L_t}v_{in0}s_{1R} - \frac{1}{L_t}v_{o0}s_{2R} - \frac{R_t}{L_t}i_{tR} + \omega_s i_{tI} \tag{18}$$

$$\dot{i}_{tI} = \frac{1}{L_t}v_{in0}s_{1I} - \frac{1}{L_t}v_{o0}s_{2I} - \omega_s i_{tR} - \frac{R_t}{L_t}i_{tI} \tag{19}$$

The preceding equations are applicable to any modulation strategy, provided that the dc average of the switching signals is zero. In the case of triple phase shift modulation, the switching signals are functions of three control arguments: d_ϕ, d_p, and d_s. These variables are contained in vector $D = [d_\phi \quad d_p \quad d_s]^T$. The switching signals are:

$$s_1(\tau, D) = \begin{cases} 1, & 0 \le \tau < \frac{d_p T_s}{2} \\ 0, & \frac{d_p T_s}{2} \le \tau < \frac{T_s}{2} \text{ or } \frac{(1+d_p)T_s}{2} \le \tau < T_s \\ -1, & \frac{T_s}{2} \le \tau < \frac{(1+d_p)T_s}{2} \end{cases} \tag{20}$$

$$s_2(\tau, D) = \begin{cases} 1, & \frac{d_\phi T_s}{2} \le \tau < \frac{(d_s+d_\phi)T_s}{2} \\ 0, & 0 \le \tau < \frac{d_\phi T_s}{2} \text{ or } \frac{(d_s+d_\phi)T_s}{2} \le \tau < \frac{(1+d_\phi)T_s}{2} \text{ or } \frac{(1+d_s+d_\phi)T_s}{2} \le \tau < T_s \\ -1, & \frac{(1+d_\phi)T_s}{2} \le \tau < \frac{(1+d_s+d_\phi)T_s}{2} \end{cases} \tag{21}$$

This switching scheme is very general; single, dual, and extended phase shift are special cases of triple phase shift modulation [18]. A visual representation of the triple phase shift scheme is shown in Fig. 2. The three control variables describe the duty ratio of the voltages applied to the primary winding (d_p), secondary winding (d_s), and the phase shift between them (d_ϕ). An additional phase shift defined by the distance between center points of the primary and secondary voltage pulses is d. This is an important parameter for describing triple phase shift operation [18], and is critical to the large-signal error correction method. It may be be derived from the control variables as

$$d = d_\phi - \frac{d_p}{2} + \frac{d_s}{2}. \tag{22}$$

Switching signals for dual phase shift modulation may be recovered by fixing $d_p = d_s$, and single phase shift may be recovered by further constraining $d_p = d_s = 1$. In both of these cases, it is clear from (22) that $d = d_\phi$.

Taking the Fourier series of these signals, the real and imaginary components of the switching functions are:

$$s_{1R}(D) = \frac{\sin(d_p\pi)}{\pi} \tag{23}$$

$$s_{1I}(D) = -\frac{2\sin\left(d_p\frac{\pi}{2}\right)^2}{\pi} \tag{24}$$

$$s_{2R}(D) = -\frac{\sin(d_\phi\pi) - \sin\left(\left(d_s + d_\phi\right)\pi\right)}{\pi} \tag{25}$$

$$s_{2I}(D) = -\frac{\cos(d_\phi\pi) - \cos\left(\left(d_s + d_\phi\right)\pi\right)}{\pi} \tag{26}$$

Substituting the switching signal harmonic components above into state equations (17)–(19) produces a generalized average model for a DAB with triple phase shift modulation. Again, other modulation strategies can be recovered from these equations. For instance, applying the single phase shift condition ($d_p = d_s = 1$) in the general equations yields the original DAB model, i.e. (5)–(7).

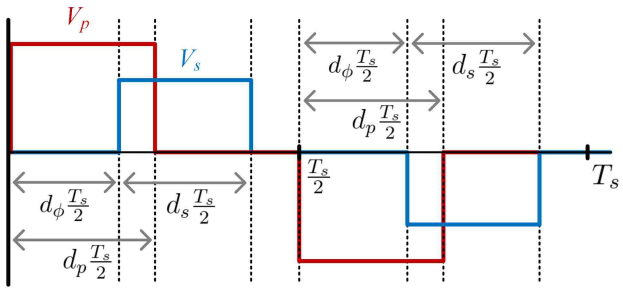

Figure 2. Triple phase shift modulation scheme. V_p and V_s denote voltages applied to the primary and secondary windings of the transformer, respectively.

3.2. Correction of Large-Signal Error. The second improvement involves correcting the large-signal modeling error due to the truncation of the Fourier series. In Sec. 2.2, the error was discussed in terms of a difference between the exact phase shift, d, and the model phase shift, $\hat{d}$. The objective of the correction method is to include a description of the relationship between these two variables in the model framework, and use this expression to correct the large-signal error. This is done by introducing $\hat{d}$ in the model as an algebraic state. Adjusted control variables $\hat{D} = [\hat{d}_\phi \quad \hat{d}_p \quad \hat{d}_s]^T$ are derived from $\hat{d}$, and are used as arguments for the switching harmonic functions in (23)–(26). The evolution of $\hat{d}$ is governed by an algebraic equation that forces normalized power transfer expressions from the model to equal corresponding expressions derived from first principles.

The correction procedure is presented as follows. First, an expression for normalized power transfer (in terms of $\hat{D}$) is derived from the GAM state equations. Next, corresponding expressions (in terms of D) from existing literature are discussed. The difference between the two expressions is included in the final model as an algebraic constraint. Finally, the actual construction of $\hat{D}$ from $\hat{d}$ is described.

The correction factor is derived from lossless model equations, i.e. state equations with $R_t \to 0$. There are two reasons for this. First, for a well-designed transformer, R_t is small, and has little effect on the steady-state power transfer. An exception to this is the case of single phase shift modulation, for which R_t plays a more significant role due to

high circulating currents. This is considered in Section 5. Second, the objective is to relate power relationships that are derived under the same conditions. Lossless power transfer equations are simple, and are readily available in the literature. Including the effect of R_t would involve a substantial increase in complexity, with only marginal benefit in terms of accuracy.

With $R_t \rightarrow 0$, a general power transfer expression is easily determined from the steady-state equations of the model. Equations (18) and (19) may be rearranged for i_{tI} and i_{tR}, respectively, and substituted into (17). The substitution results in

$$i_{L0} = \frac{2v_{in0}}{X_t}\left(s_{2R}s_{1I} - s_{1R}s_{2I}\right) \tag{27}$$

where $X_t = \omega_s L_t$ is the transformer reactance. All switching signal harmonics in (27)–and in all equations henceforth–are functions of $\hat{D}$. The transferred power is then

$$P = v_{o0}i_{L0} = \frac{v_{in0}v_{o0}}{X_t}P_N \tag{28}$$

where P_N is the normalized power, and can be expressed as

$$P_N = 2\left(s_{2R}s_{1I} - s_{1R}s_{2I}\right) \tag{29}$$

Note that this formulation assumes a current source load, i.e. $R_{sh} \rightarrow \infty$, such that the dc average current through the secondary H-bridge is equal to the load current. This assumption serves only to prevent the need for an additional current term definition; including a finite resistive load term does not change the power transfer analysis.

Next, a steady-state power transfer equation must be determined using a method that does not include the first harmonic approximation. Suitable expressions are readily available in the literature, since power transfer equations are central to converter analysis.

For instance, [18], [19], and [20] provide appropriate equations for triple, dual, and extended phase shift modulation, respectively. This function for power transfer is referred to as P^*, to distinguish from the expression determined from model equations.

Because of the wide range of operating cases that occur in triple phase shift modulation, no single expression for P^* is sufficient. In [18], five separate modes of operation are defined, each with their own power transfer expression. For full generality, P^* is defined as a piecewise function that selects between components according to the control inputs of the model. Table 1 shows the five power transfer equations and the operating conditions under which each is active. The active mode is determined by d, and is easily identified from the control inputs.

The expressions in Table 1 are the same as those in [18], but are given in the terminology used in this study, and are normalized as:

$$P^* = \frac{v_{in0} v_{o0}}{X_t} P_N^* \tag{30}$$

The reason for this normalization is to simplify expressions when relating P^* to P. Clearly, when P^* and P are set equal, the leading fractional terms cancel out.

Table 1. Triple Phase Shift Operating Modes and Power Transfer Equations

Mode	Operating Region	Normalized Power Expression
I	$0 \le d \le \frac{d_s}{2} - \frac{d_p}{2}$	$P_N^* = \pi d_p \left(d_\phi - \frac{d_p}{2} - \frac{d_s}{2} \right)$
II	$0 \le d \le \frac{d_p}{2} - \frac{d_s}{2}$	$P_N^* = \pi d_s \left(d_\phi - \frac{d_p}{2} - \frac{d_s}{2} \right)$
III	$\left\lvert \frac{d_p}{2} - \frac{d_s}{2} \right\rvert \le d \le \min \left\{ \frac{d_p}{2} + \frac{d_s}{2}, 1 - \frac{d_p}{2} - \frac{d_s}{2} \right\}$	$P_N^* = \frac{\pi}{2} \left(d_p (d_s + 2 d_\phi) - d_p^2 - d_\phi^2 \right)$
IV	$1 - \frac{d_p}{2} - \frac{d_s}{2} \le d \le \frac{d_p}{2} + \frac{d_s}{2}$	$P_N^* = \frac{\pi}{2} \left[2 d_\phi (1 - d_\phi - d_s + d_p) + d_s (2 + d_p - d_s) - d_p^2 - 1 \right]$
V	$\frac{d_p}{2} + \frac{d_s}{2} \le d \le 1 - \frac{d_p}{2} - \frac{d_s}{2}$	$P_N^* = \frac{\pi}{2} d_p d_s$

The final part of the correction procedure is determining how $\hat{D}$ is generated from $\hat{d}$. Because of the multiple degrees of freedom involved in triple phase shift modulation, there are several viable ways to do this. The simplest method is to adjust only $\hat{d}_\phi$. The control variables are then

$$\hat{d}_\phi = \hat{d} + \frac{d_p}{2} - \frac{d_s}{2} \tag{31}$$

$$\hat{d}_p = d_p \tag{32}$$

$$\hat{d}_s = d_s \tag{33}$$

This approach is sufficient for correcting error over the full possible range of control inputs for both single and dual phase shift modulation.

For triple phase shift modulation, an additional adjustment scheme is needed to ensure that a solution to the algebraic power equation exists over the entire operating space. For a solution to exist, the maximum normalized power transfer over the possible range of $\hat{d}$ must exceed the corresponding value of P^*. In addition to the correction applied to d_ϕ, an adjustment can be applied to d_p as

$$\hat{d}_\phi = d_\phi \tag{34}$$

$$\hat{d}_p = 2d_\phi - 2\hat{d} + d_s \tag{35}$$

$$\hat{d}_s = d_s \tag{36}$$

For a given set of control inputs, the correction should be applied to either d_ϕ or d_p. The selection is made according to which choice produces the larger maximum normalized power transfer. This can be determined by the following condition:

$$\sin\left(\frac{d_p\pi}{2}\right) > \sin^2\left(\frac{\pi}{2}\left(\frac{d_s}{2} + d_\phi\right)\right) \tag{37}$$

If this condition is true, the correction should be applied to d_ϕ. If not, the correction should be applied to d_p. This condition may be derived as follows. First, analytical expressions for P_N as functions of $\hat{d}$ are determined for each of the correction schemes. This is done by substituting either (31), (32), and (33) or (34), (35), and (36) into (29). Next, the maximum values of the expressions for P_N are determined by setting derivatives with respect to $\hat{d}$ equal to 0, solving for $\hat{d}$, and substituting the results back into the P_N expressions. The right and left sides of (37) correpond to the two resultant expressions after common coefficients have been eliminated. Therefore, when the inequality is true, applying the correction through d_ϕ yields the higher maximum normalized power. This provides a simple method of identifying the the proper correction scheme using only the control inputs to the model.

3.3. Model Organization. The structure of the proposed model framework is

$$\dot{x} = f(x, \hat{d}, u) \tag{38}$$

$$0 = g(x, \hat{d}, u) \tag{39}$$

where x is the state vector, u is the input vector, and $\hat{d}$ is an algebraic state variable. The model state equations are contained in vector-valued function $f(\cdot)$. The scalar function $g(\cdot)$ is defined as

$$g(x, \hat{d}, u) \triangleq P^* - P \tag{40}$$

Together, $f(\cdot)$ and $g(\cdot)$ define a semi-explicit (or type 1) system of differential algebraic equations (DAEs).

The state equations, state vector, and input vector differ according to whether an open or closed-loop system is being modeled. Both are discussed below. Subscripts ‘o’ and ‘c’ are used to denote whether model elements (namely $f(\cdot)$, x, and u) pertain to the open-loop or closed-loop systems, respectively.

The state and input vectors of the open-loop model are

$$x_o = [v_{o0} \quad i_{tR} \quad i_{tI}]^T \tag{41}$$

$$u_o = [v_{in0} \quad i_{L0} \quad d_\phi \quad d_p \quad d_s]^T. \tag{42}$$

The state equations in $f_o(\cdot)$ are exactly those of the original DAB model, shown in Section 2 as (5), (6), and (7). With respect to large-signal error correction, the critical point of difference between this model and the model in [13] is that d, rather than $\hat{d}$, is defined as an input.

Triple phase shift modulation includes three control variables, and a wide variety of control structures and feedback mechanisms are possible. To limit scope, the closed-loop formulation in the present study considers a single controller that regulates output voltage through the phase shift control variable, d_ϕ. The state and input vectors of the closed-loop model are

$$x_c = [v_{o0} \quad i_{tR} \quad i_{tI} \quad \gamma_0]^T \tag{43}$$

$$u_c = [v_{in0} \quad i_{L0} \quad v_{ref} \quad d_p \quad d_s]^T. \tag{44}$$

The additional state, γ_0, is contributed by the integral of a PI controller. In addition to the open-loop state equations, $f_c(\cdot)$ contains (8), which describes γ_0. In the original model, controller output was defined to be $\hat{d}_\phi$ (or, equivalently $\hat{d}$), as shown in (9). In contrast, controller output is defined in the present model as

$$d_\phi = k_p \left(v_{ref} - v_{o0}\right) + \gamma_0. \tag{45}$$

3.4. Discussion. The system defined by (38) and (39) is a large-signal generalized average model that is accurate in both transient and steady-state conditions. The model is a semi-explicit DAE system. Models of this type are commonly used for describing power

systems [21] and are suitable for all applications expected of power electronics models. In particular, they may be used for time-domain simulations, stability analyses, or linearized to provide small-signal representations.

Both of the model improvements proposed here generalize the original DAB model from [13]. Extension to more advanced modulation strategies is a fairly straightforward improvement, but the inclusion of $g(\cdot)$, too, is a generalization of the original model. The model from [13] implicitly assumes that $\hat{d} = d$. This assumption may be included in the proposed modeling framework by defining $g(\cdot)$ as $0 = \hat{d} - d$. The resulting structure, when used with single phase shift modulation, is identical to the model in [13].

While the general model is a DAE system, in some operating cases (namely single phase shift modulation) it is possible to define $\hat{d}$ as an explicit function of d, i.e. by solving $g(\cdot)$ directly for $\hat{d}$. When an explicit solution is possible, the model may be converted into an equivalent system of ODEs.

In comparison to alternative continuous-time DAB modeling approaches, the primary advantage of the proposed modeling framework is flexibility. The most closely related methods, i.e. [11] and [16], consider only single phase shift modulation. The method in [11] is not affected by large-signal error, but its derivation is inherently tied to the modulation strategy, meaning new modulation schemes would require a full rederivation. In contrast, the proposed method is derived for general switching functions, so different modulation schemes are be included by changing modular elements of the base model. Additionally, the method in [11] models the ac stage by deriving averaged equations for the dc currents into and out of the H-bridge circuits, effectively consolidating the switching circuit as a single averaged element. As a result, frequency domain accuracy is limited to $1/10$ the switching frequency. In contrast, the original DAB model from [13] is accurate up to $1/3$ of the switching frequency. The upper frequency bound is, in general, imposed by the eigenvalues of the dynamic model [10, 22]. The proposed model maintains the small-signal

accuracy of the model from [13]; when linearized, the eigenvalues of the proposed model are very close to those of the original model, meaning their upper-limits are similar as well. This is further illustrated in Sec. 6.

The method from [16] is more closely related to the proposed framework than [11], but differs in how the correction factor is applied. The correction factor in [16] modifies the load and state variables directly, and the modifications required are different for each of the state variables. In this study, error correction is applied through an algebraic equation rather than through the model state variables, so modifications to the correction factor equation do not change the base model. This makes it possible to include more general modulation strategies or lossy correction factors within the same modeling framework.

4. PARTIAL DERIVATIVES AND SMALL-SIGNAL MODELS

Partial derivatives are central to many modeling applications. Partial derivatives are used for calculating steady-state solutions to model equations, time-domain simulation via numerical integration, and linearization for small-signal analysis. The partial derivatives of the models under consideration are given in this section.

4.1. Open-Loop System. The partial derivatives of the open-loop model equations are with respect to converter states are:

$$\frac{\partial f_o}{\partial x_o} = \begin{bmatrix} \frac{-1}{R_{sh}C_o} & \frac{2}{C_o}s_{2R} & \frac{2}{C_o}s_{2I} \\ \frac{-1}{L_t}s_{2R} & \frac{-R_t}{L_t} & \omega_s \\ \frac{-1}{L_t}s_{2I} & -\omega_s & \frac{-R_t}{L_t} \end{bmatrix} \tag{46}$$

$$\frac{\partial f_o}{\partial \hat{d}} = \begin{bmatrix} \frac{2}{C_o}\left(i_{tR}\frac{\partial s_{2R}}{\partial \hat{d}} + i_{tI}\frac{\partial s_{2I}}{\partial \hat{d}}\right) \\ \frac{1}{L_t}\left(v_{in0}\frac{\partial s_{1R}}{\partial \hat{d}} - v_{o0}\frac{\partial s_{2R}}{\partial \hat{d}}\right) \\ \frac{1}{L_t}\left(v_{in0}\frac{\partial s_{1I}}{\partial \hat{d}} - v_{o0}\frac{\partial s_{2I}}{\partial \hat{d}}\right) \end{bmatrix} \tag{47}$$

$$\frac{\partial f_o}{\partial u_o} = \tag{48}$$
$$\begin{bmatrix} 0 & \frac{-1}{C_o} & \frac{2}{C_o}\left(i_{tR}\frac{\partial s_{2R}}{\partial d_\phi} + i_{tI}\frac{\partial s_{2I}}{\partial d_\phi}\right) & \frac{2}{C_o}\left(i_{tR}\frac{\partial s_{2R}}{\partial d_p} + i_{tI}\frac{\partial s_{2I}}{\partial d_p}\right) & \frac{2}{C_o}\left(i_{tR}\frac{\partial s_{2R}}{\partial d_s} + i_{tI}\frac{\partial s_{2I}}{\partial d_s}\right) \\ \frac{1}{L_t}s_{1R} & 0 & \frac{1}{L_t}\left(v_{in0}\frac{\partial s_{1R}}{\partial d_\phi} - v_{o0}\frac{\partial s_{2R}}{\partial d_\phi}\right) & \frac{1}{L_t}\left(v_{in0}\frac{\partial s_{1R}}{\partial d_p} - v_{o0}\frac{\partial s_{2R}}{\partial d_p}\right) & \frac{1}{L_t}\left(v_{in0}\frac{\partial s_{1R}}{\partial d_s} - v_{o0}\frac{\partial s_{2R}}{\partial d_s}\right) \\ \frac{1}{L_t}s_{1I} & 0 & \frac{1}{L_t}\left(v_{in0}\frac{\partial s_{1I}}{\partial d_\phi} - v_{o0}\frac{\partial s_{2I}}{\partial d_\phi}\right) & \frac{1}{L_t}\left(v_{in0}\frac{\partial s_{1I}}{\partial d_p} - v_{o0}\frac{\partial s_{2I}}{\partial d_p}\right) & \frac{1}{L_t}\left(v_{in0}\frac{\partial s_{1I}}{\partial d_s} - v_{o0}\frac{\partial s_{2I}}{\partial d_s}\right) \end{bmatrix}$$

The switching signal derivatives are shown in general form in these equations. The specific derivatives for triple phase shift modulation are given in Sec. 4.3.

The partial derivatives of the algebraic function $g(\cdot)$ are

$$\frac{\partial g}{\partial x_o} = \begin{bmatrix} 0 & 0 & 0 \end{bmatrix} \tag{49}$$

$$\frac{\partial g}{\partial \hat{d}} = 2\left(s_{1R}\frac{\partial s_{2I}}{\partial \hat{d}} + s_{2I}\frac{\partial s_{1R}}{\partial \hat{d}}\right) - 2\left(s_{2R}\frac{\partial s_{1I}}{\partial \hat{d}} + s_{1I}\frac{\partial s_{2R}}{\partial \hat{d}}\right) \tag{50}$$

$$\frac{\partial g}{\partial u_o} = \begin{bmatrix} 0 & 0 & \frac{\partial g}{\partial d_\phi} & \frac{\partial g}{\partial d_p} & \frac{\partial g}{\partial d_s} \end{bmatrix} \tag{51}$$

where $\frac{\partial g}{\partial d_\phi}$, $\frac{\partial g}{\partial d_p}$ and $\frac{\partial g}{\partial d_s}$ are given by

$$\frac{\partial g}{\partial d_\phi} = \frac{\partial P_N^*}{\partial d_\phi} + 2\left(s_{1R}\frac{\partial s_{2I}}{\partial d_\phi} + s_{2I}\frac{\partial s_{1R}}{\partial d_\phi}\right) - 2\left(s_{2R}\frac{\partial s_{1I}}{\partial d_\phi} + s_{1I}\frac{\partial s_{2R}}{\partial d_\phi}\right) \tag{52}$$

$$\frac{\partial g}{\partial d_p} = \frac{\partial P_N^*}{\partial d_p} + 2\left(s_{1R}\frac{\partial s_{2I}}{\partial d_p} + s_{2I}\frac{\partial s_{1R}}{\partial d_p}\right) - 2\left(s_{2R}\frac{\partial s_{1I}}{\partial d_p} + s_{1I}\frac{\partial s_{2R}}{\partial d_p}\right) \tag{53}$$

$$\frac{\partial g}{\partial d_s} = \frac{\partial P_N^*}{\partial d_s} + 2\left(s_{1R}\frac{\partial s_{2I}}{\partial d_s} + s_{2I}\frac{\partial s_{1R}}{\partial d_s}\right) - 2\left(s_{2R}\frac{\partial s_{1I}}{\partial d_s} + s_{1I}\frac{\partial s_{2R}}{\partial d_s}\right) \tag{54}$$

The derivatives of P_N^* with respect to control inputs depend on the operational mode. For all of the cases shown in Table 1, these terms are straightforward derivatives of polynomial functions.

4.2. Closed-Loop System. The partial derivatives of the closed-loop model equations are:

$$\frac{\partial f_c}{\partial x_c} = \begin{bmatrix} \frac{-1}{R_{sh}C_o} & \frac{2}{C_o}s_{2R} & \frac{2}{C_o}s_{2I} & 0 \\ \frac{-1}{L_t}s_{2R} & \frac{-R_t}{L_t} & \omega_s & 0 \\ \frac{-1}{L_t}s_{2I} & -\omega_s & \frac{-R_t}{L_t} & 0 \\ -k_i & 0 & 0 & 0 \end{bmatrix} \tag{55}$$

$$\frac{\partial f_c}{\partial \hat{d}_\phi} = \begin{bmatrix} \frac{\partial f_o}{\partial \hat{d}_\phi} \\ 0 \end{bmatrix} \tag{56}$$

where $\frac{\partial f_o}{\partial \hat{d}_\phi}$ is given in (47), and

$$\frac{\partial f_c}{\partial u_c} = \begin{bmatrix} 0 & \frac{-1}{C_o} & 0 & \frac{2}{C_o}\left(i_{tR}\frac{\partial s_{2R}}{\partial d_p} + i_{tI}\frac{\partial s_{2I}}{\partial d_p}\right) & \frac{2}{C_o}\left(i_{tR}\frac{\partial s_{2R}}{\partial d_s} + i_{tI}\frac{\partial s_{2I}}{\partial d_s}\right) \\ \frac{1}{L_t}s_{1R} & 0 & 0 & \frac{1}{L_t}\left(v_{in0}\frac{\partial s_{1R}}{\partial d_p} - v_{o0}\frac{\partial s_{2R}}{\partial d_p}\right) & \frac{1}{L_t}\left(v_{in0}\frac{\partial s_{1R}}{\partial d_s} - v_{o0}\frac{\partial s_{2R}}{\partial d_s}\right) \\ \frac{1}{L_t}s_{1I} & 0 & 0 & \frac{1}{L_t}\left(v_{in0}\frac{\partial s_{1I}}{\partial d_p} - v_{o0}\frac{\partial s_{2I}}{\partial d_p}\right) & \frac{1}{L_t}\left(v_{in0}\frac{\partial s_{1I}}{\partial d_s} - v_{o0}\frac{\partial s_{2I}}{\partial d_s}\right) \\ 0 & 0 & k_i & 0 & 0 \end{bmatrix} \tag{57}$$

$$\frac{\partial g}{\partial x_c} = \begin{bmatrix} -k_p\frac{\partial P_N^*}{\partial d_\phi} & 0 & 0 & \frac{\partial P_N^*}{\partial d_\phi} \end{bmatrix} \tag{58}$$

The derivative $\frac{\partial g}{\partial \hat{d}_\phi}$ is the same as for the open loop system, as shown in (50). Finally,

$$\frac{\partial g}{\partial u_c} = \begin{bmatrix} 0 & 0 & k_p\frac{\partial g}{\partial d_\phi} & \frac{\partial g}{\partial d_p} & \frac{\partial g}{\partial d_s} \end{bmatrix} \tag{59}$$

where $\frac{\partial g}{\partial d_\phi}$, $\frac{\partial g}{\partial d_p}$ and $\frac{\partial g}{\partial d_s}$ are given (52), (53) and (54), respectively.

4.3. Switching Signal Derivatives. When the correction factor is applied through d_ϕ, switching function s_1 is only a function of control variable d_p. Therefore, the partial derivatives of s_{1R} and s_{1I} with respect to $\hat{d}$, d_ϕ, and d_s are 0. The derivatives with respect to d_p are

$$\frac{\partial s_{1R}}{\partial d_p} = \cos(d_p\pi) \tag{60}$$

$$\frac{\partial s_{1I}}{\partial d_p} = -\sin(d_p\pi) \tag{61}$$

Switching function s_2 is a function of variables $\hat{d}$ (through $\hat{d}_\phi$), d_p, and d_s. Since d_ϕ is replaced, the derivatives with respect to d_ϕ are 0. The remaining derivatives are

$$\frac{\partial s_{2R}}{\partial d_p} = \frac{1}{2}\left(\cos((d_s + \hat{d}_\phi)\pi) - \cos(\hat{d}_\phi\pi)\right) \tag{62}$$

$$\frac{\partial s_{2I}}{\partial d_p} = \frac{1}{2}\left(\sin(\hat{d}_\phi\pi) - \sin((d_s + \hat{d}_\phi)\pi)\right) \tag{63}$$

$$\frac{\partial s_{2R}}{\partial d_s} = \frac{1}{2}\left(\cos((d_s + \hat{d}_\phi)\pi) + \cos(\hat{d}_\phi\pi)\right) \tag{64}$$

$$\frac{\partial s_{2I}}{\partial d_s} = \frac{-1}{2}\left(\sin(\hat{d}_\phi\pi) + \sin((d_s + \hat{d}_\phi)\pi)\right) \tag{65}$$

$$\frac{\partial s_{2R}}{\partial \hat{d}} = \cos((d_s + \hat{d}_\phi)\pi) - \cos(\hat{d}_\phi\pi) \tag{66}$$

$$\frac{\partial s_{2I}}{\partial \hat{d}} = \sin(\hat{d}_\phi\pi) - \sin((d_s + \hat{d}_\phi)\pi) \tag{67}$$

When the correction factor is applied through d_p, switching function s_1 depends on $\hat{d}$ (through $\hat{d}_p$), d_s, and d_ϕ. Input d_1 is replaced, so derivatives with respect to d_1 are 0.

$$\frac{\partial s_{1R}}{\partial d_\phi} = \cos(\hat{d}_p\pi) \tag{68}$$

$$\frac{\partial s_{1I}}{\partial d_\phi} = -\sin(\hat{d}_p\pi) \tag{69}$$

$$\frac{\partial s_{1R}}{\partial d_s} = 2\cos(\hat{d}_p\pi) \tag{70}$$

$$\frac{\partial s_{1I}}{\partial d_s} = -2\sin(\hat{d}_p\pi) \tag{71}$$

$$\frac{\partial s_{1R}}{\partial \hat{d}} = -2\cos(\hat{d}_p\pi) \tag{72}$$

$$\frac{\partial s_{1I}}{\partial \hat{d}} = 2\sin(\hat{d}_p\pi) \tag{73}$$

Lastly, switching function s_2 depends only on d_ϕ and d_s, so derivatives with respect to d_p and $\hat{d}$ are zero.

$$\frac{\partial s_{2R}}{\partial d_\phi} = \cos((d_s + d_\phi)\pi) \tag{74}$$

$$\frac{\partial s_{2I}}{\partial d_\phi} = -\sin((d_s + d_\phi)\pi) \tag{75}$$

$$\frac{\partial s_{2R}}{\partial d_s} = \cos((d_s + d_\phi)\pi) - \cos(d_\phi\pi) \tag{76}$$

$$\frac{\partial s_{2I}}{\partial d_s} = \sin(d_\phi\pi) - \sin((d_s + d_\phi)\pi) \tag{77}$$

4.4. Small-Signal Models. For all models under consideration, the small-signal models have the form

$$\dot{\tilde{x}} = A\tilde{x} + B\tilde{u} \tag{78}$$

where $\tilde{x}$ is a vector of small-signal deviations around a steady-state operating point. Matrices A and B are calculated using matrix operations, give here in terms of generic functions $f(\cdot)$ and $g(\cdot)$.

$$A = \frac{\partial f}{\partial x} - \frac{\partial f}{\partial \hat{d}}\left(\frac{\partial g}{\partial \hat{d}}\right)^{-1}\frac{\partial g}{\partial x} \tag{79}$$

$$B = \frac{\partial f}{\partial u} - \frac{\partial f}{\partial \hat{d}}\left(\frac{\partial g}{\partial \hat{d}}\right)^{-1}\frac{\partial g}{\partial u} \tag{80}$$

The derivation for these linearized matrices is given in the Appendix.

5. CONSIDERATIONS FOR SINGLE PHASE SHIFT MODULATION

Although single phase shift modulation has several performance deficiencies, it is still commonly used in DAB literature due to its overall simplicity. In particular, single phase shift is commonly used in studies that include DAB converters as elements of a larger system [15, 23]. In light of this, a more detailed consideration of the single phase shift case is given here. As a secondary benefit, this section provides a simple illustration of how the general framework outlined in Section 4 may be applied to a specific modulation scheme.

5.1. Model Simplifications. Single phase shift modulation is a subset of triple phase shift, and corresponds to the case in which d_p and d_s are constant and equal to 1. This condition simplifies the model. With d_p and d_s fixed, it is not necessary to include these variables as model inputs, and $d_\phi = d$.

The first harmonic components of switching functions for single phase shift modulation may be recovered by fixing $d_p = d_s = 1$ in (23)–(26).

$$s_{1R}(\hat{d}) = 0 \tag{81}$$

$$s_{1I}(\hat{d}) = -\frac{2}{\pi} \tag{82}$$

$$s_{2R}(\hat{d}) = -\frac{2\sin(\hat{d}\pi)}{\pi} \tag{83}$$

$$s_{2I}(\hat{d}) = -\frac{2\cos(\hat{d}\pi)}{\pi} \tag{84}$$

Furthermore, single phase shift modulation restricts the operating region of the converter. According to Table 1, single phase shift modulation is entirely contained in Mode IV, so only one power transfer equation is necessary.

5.2. Lossless Case. Without including R_t, the procedure begins directly with normalized power:

$$P_N = 2(s_{2R}s_{1I} - s_{1R}s_{2I}) = \frac{8\sin(\hat{d}\pi)}{\pi^2} \tag{85}$$

Next, the power transfer equation from Table 1 is reduced using the same conditions on d_p and d_s. These conditions restrict the operating region to Mode IV, and the corresponding equation simplifies to

$$P_N^* = \pi d(1-d). \tag{86}$$

Therefore, the equation that relates $\hat{d}$ to d is

$$g(x, \hat{d}, u) = \frac{\pi^3 d(1-d)}{8} - \sin \pi \hat{d} \tag{87}$$

5.3. Lossy Case. In the lossy case, R_t is nonzero. The parameter R_t is represents winding losses in the transformer, but it can also be used as a lumped-element parameter to represent conduction losses in the semiconductors as well. Including R_t in the large-signal error correction requires a substantial increase in complexity, and is only necessary when the losses modeled by R_t become significant. One case in which R_t plays an important role is single phase shift modulation with high phase shift values. Under these conditions, the transformer will experience high circulating currents, and conduction losses will be larger. While this issue may be addressed through the use of more advanced modulation schemes, there is still a need to accurately represent converter behavior under these conditions when single phase shift modulation is used. The problem with including R_t in the error correction is that the power transfer equations become dependent on state variables and hardware parameters. In the previous cases, $g(\cdot)$ was only dependent on control variables. This is not the case when R_t is included. Nevertheless, the procedure for deriving the correction equation remains the same. The expression for i_{L0} in terms of $\hat{d}$ given in (27) was derived with $R_t \to 0$. When R_t included in the derivation, the resulting expression is

$$i_{L0} = \frac{2\Big((s_{2R}R_t - s_{2I}X_t)\,(v_{in0}s_{1R} - v_{o0}s_{2R})\Big)}{R_t^2 + X_t^2} + \frac{2\Big((s_{2I}R_t + s_{2R}X_t)\,(v_{in0}s_{1I} - v_{o0}s_{2I})\Big)}{R_t^2 + X_t^2} \tag{88}$$

After applying the simplifications for single phase shift modulation, this may be more conveniently written as

$$i_{L0} = \frac{2X_t}{\pi R_t^2 K}(v_{in0}R_t \cos \pi\hat{d} + v_{in0}X_t \sin \pi\hat{d} - v_{o0}R_t) \tag{89}$$

where K is a hardware constant given by

$$K = \frac{\pi}{4}\frac{X_t(R_t^2 + X_t^2)}{R_t^2}. \tag{90}$$

The definition of K is arbitrary at this point, but substantially simplifies derivative terms when linearizing the model.

The next step is to determine a corresponding expression in terms of d. Average output current equations have previously been derived in the literature. One such equation is used by the average value model proposed in [11]. However, the equation in question (Eq. (19) in [11]) is valid only for unidirectional power flow, i.e. $d > 0$. A more suitable equation is derived in [12] by integrating the instantaneous current terms, which are piecewise exponential, over the switching period. This expression (originally Eq. (6) in [12]) is cumbersome; the authors of [12] spend considerable effort obtaining a more manageable approximation. In this study, we use a simplified form of the exact equation:

$$i_{L0}^* = \frac{(v_{in0} - v_{o0})}{R_t} + \frac{v_{o0}}{\theta R_t}\tanh\theta + \frac{d}{|d|}\left(\frac{v_{in0}}{\theta R_t}\right)\left[1 - 2\theta d - \operatorname{sech}\theta \exp\left(\frac{d}{|d|}\theta - 2\theta d\right)\right] \tag{91}$$

where θ is a hardware constant.

$$\theta = \frac{\pi R_t}{2X_t} \tag{92}$$

The expression in (91) is mathematically equivalent to Eq. (6) in [12]. The only differences are that notational conventions have been changed (e.g. phase shift is defined as a fraction of the switching period rather than an angle) and simplifications have been applied using hyperbolic function identities. The exact conversion consists entirely of standard

algebraic manipulations, and the result is easily verified using a computer algebra system. The final form of (91) is relatively simple. The arguments of hyperbolic functions tanh and sech are hardware constants, so they have very little impact on complexity when applied in the model. Furthermore, the sign factors $\frac{d}{|d|}$ are only necessary to support bidirectional operation. For the unidirectional power flow case these may be eliminated entirely.

The final step is to form the algebraic correction equation. Since $P = v_{o0} i_{L0}$ and $P^* = v_{o0} i_{L0}^*$, the equation may be defined as

$$\begin{aligned} g(x, \hat{d}, u) &= i_{L0}^* - i_{L0} \\ &= -v_{in0} R_t \cos \pi \hat{d} - v_{in0} X_t \sin \pi \hat{d} + v_{o0} R_t \\ &+ K \left(v_{in0} - v_{o0} \right) \theta + K v_{o0} \tanh \theta \\ &+ K v_{in0} \frac{d}{|d|} \left(1 - 2\theta d - \operatorname{sech} \theta \exp \left(\frac{d}{|d|} \theta - 2\theta d \right) \right) \end{aligned} \tag{93}$$

Since (19) includes v_{o0} and v_{in0}, some of the derivatives from Section 4 must be changed. For the open-loop system, the derivatives of $g(\cdot)$ are

$$\frac{\partial g}{\partial x_o} = \begin{bmatrix} R_t - K \left(\theta - \tanh \theta \right) & 0 & 0 \end{bmatrix} \tag{94}$$

$$\frac{\partial g}{\partial \hat{d}} = \pi v_{in0} \left(R_t \sin \pi \hat{d} - X_t \cos \pi \hat{d} \right) \tag{95}$$

$$\frac{\partial g}{\partial u_o} = \begin{bmatrix} \frac{\partial g}{\partial v_{in0}} & 0 & \frac{\partial g}{\partial d} \end{bmatrix} \tag{96}$$

where elements $\frac{\partial g}{\partial v_{in0}}$ and $\frac{\partial g}{\partial d}$ are given by

$$\frac{\partial g}{\partial v_{in0}} = K\theta - R_t \cos \pi \hat{d} - X_t \sin \pi \hat{d} + K \frac{d}{|d|} \left(1 - 2\theta d - \operatorname{sech} \theta \exp \left(\frac{d}{|d|} \theta - 2\theta d \right) \right) \tag{97}$$

$$\frac{\partial g}{\partial d} = \left(\frac{2 d \theta K v_{in0}}{|d|} \right) \left(\operatorname{sech} \theta \exp \left(\frac{d}{|d|} \theta - 2\theta d \right) - 1 \right) \tag{98}$$

For the closed-loop system, the derivatives of $g(\cdot)$ are

$$\frac{\partial g}{\partial x_c} = \begin{bmatrix} R_t - K\left(\theta - \tanh\theta\right) & 0 & 0 & \frac{\partial g}{\partial d} \end{bmatrix} \tag{99}$$

$$\frac{\partial g}{\partial u_c} = \begin{bmatrix} \frac{\partial g}{\partial v_{in0}} & 0 & k_p \frac{\partial g}{\partial d} \end{bmatrix} \tag{100}$$

where the elements $\frac{\partial g}{\partial v_{in0}}$ and $\frac{\partial g}{\partial d}$ are given in (97) and (98), respectively.

6. VERIFICATION

To validate the proposed models, experiments were performed to verify model accuracy both at steady-state and during transient response. The experiments were conducted using a small-scale DAB prototype, shown in Fig. 3. Switching simulations performed in PLECS supplement the hardware results. The prototype converter is controlled by a Texas Instruments TMS320F28377S digital signal processor (DSP). Both the sampling rate and switching frequency of the converter were 80 kHz. Switching dead time was $t_d = 300$ ns. These and other important parameters are given in Table 2.

The effect of switching dead time on converter behavior is significant in practice. Dead time introduces conduction modes that are not explicitly included in the model derivation, and effectively changes the control inputs d_ϕ, d_p, and d_s [24]. Including conduction modes related to dead time in the model would require a substantial increase in complexity. Alternatively, dead time compensation strategies may be employed in the control system. The latter approach is used here: dead time is compensated in the controller by applying phase shift corrections according to [25].

6.1. Steady-State Accuracy. The first test considers steady-state accuracy. The converter output voltage is measured while varying d_ϕ. A resistive load is used and input voltage is fixed at 10 V throughout. Results for triple and dual phase shift modulation are shown in Fig. 4 and Fig. 5, respectively. For these results, and the dual and triple phase shift

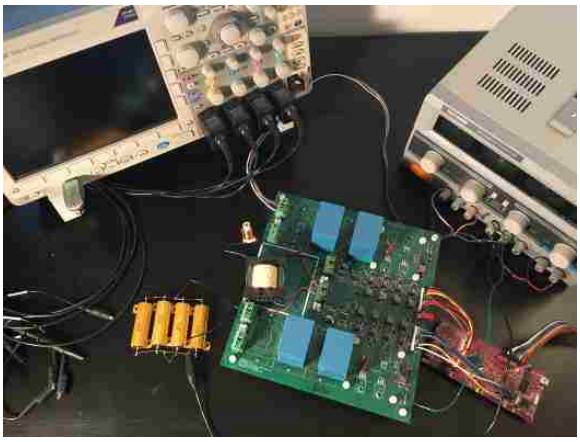

Figure 3. Prototype DAB converter.

Table 2. Control and Hardware Parameters

Parameter	Value	Parameter	Value
C_{in}	40 μF	C_o	40 μF
L_t	5.53 μH	R_t	0.55 Ω
$n_1 : n_2$	1 : 0.85	R_{sh}	6.667 Ω
k_p	0.01	k_i	25

dynamic results in the following subsection, lossless model correction factors have been used. Two combinations of d_p and d_s are considered in each plot. Fig. 4 shows results with $d_p = 0.5$, $d_s = 0.75$ and $d_p = 0.75$, $d_s = 0.5$. Fig. 4 shows results with $d_p = d_s = 0.5$ and $d_p = d_s = 0.75$. In all cases, d_ϕ is varied over the operating range for which $0 < d < 0.5$. The results indicate that the large-signal model accurately predicts the steady-state response of the converter.

Results for single phase shift modulation are shown in Fig. 6. In this case, the hardware results are compared to the uncorrected model and to the corrected model using both lossless and lossy correction factors. As expected, the lossy variant is more accurate for larger phase shifts, since the effects of converter loss become more significant.

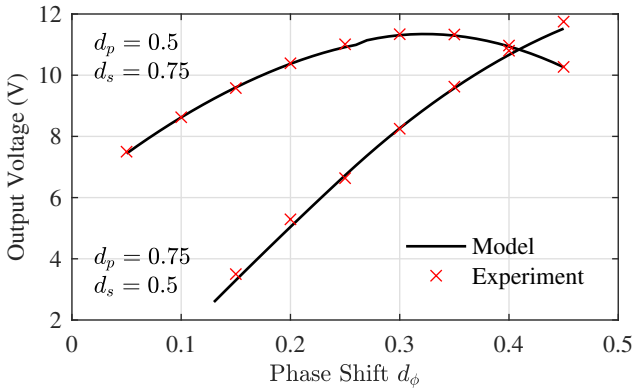

Figure 4. Comparison of relationships between phase shift inputs and output voltage for triple phase shift modulation.

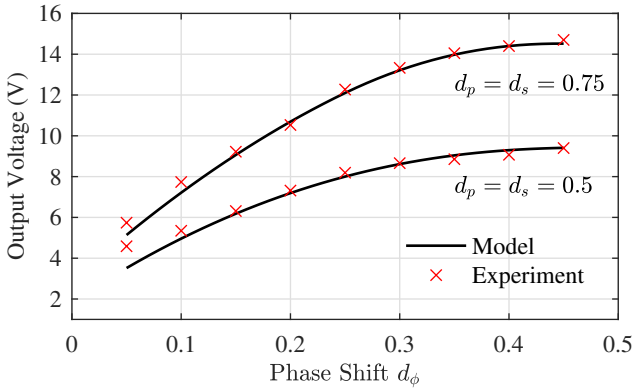

Figure 5. Comparison of relationships between phase shift inputs and output voltage for dual phase shift modulation.

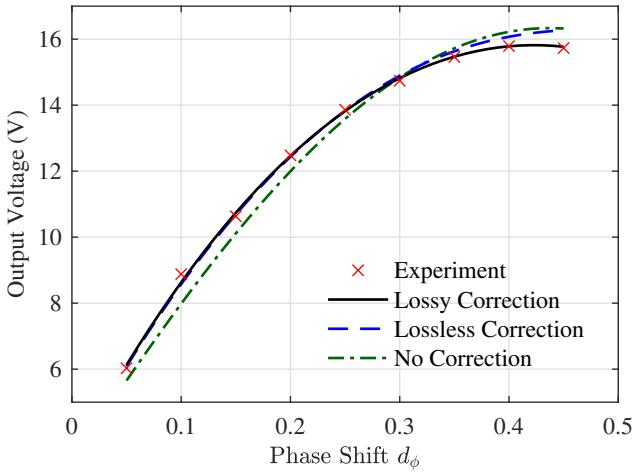

Figure 6. Comparison of relationships between phase shift and output voltage for single phase shift modulation.

6.2. Dynamic Accuracy. The second set of tests consider dynamic response, namely the output voltage transients for step changes in phase shift inputs. The experiment uses same resistive load and 10 V input voltage as in the previous test. For triple phase shift modulation, step changes to d_p and d_s are considered. The results are shown in Fig. 7. At the start of the experiment, both d_p and d_s are 0.5; at $t = 0$ ms, d_s steps from 0.5 to 0.75. At $t = 2$ ms, d_p steps from 0.5 to 0.75. The model predictions and experimental results are consistent for both transients.

In dual phase shift modulation, d_p and d_s are equal, so only one step change is considered. The results for dual phase shift modulation are shown in Fig. 8. At time $t = 0$ ms, both d_p and d_s change from 0.5 to 0.75. Again, the model accurately predicts the response.

For single phase shift, step changes in d_ϕ are considered. As in the steady-state experiments, hardware measurements are compared to the uncorrected model and to both lossless and lossy variants of the corrected model. The results are shown in Fig. 9. In the top plot, d_ϕ steps from 0.15 to 0.3 at $t = 0$ ms; in the bottom plot d_ϕ steps from 0.3 to 0.4. The plots show both the raw hardware measurements and dc sliding averages of the measurements, taken over a single switching period. These averages are, by definition, the experimental v_{o0}.

The top plots of Fig. 9 show that if large phase shifts are avoided, the difference in accuracy between the lossless and lossy model variants is negligible. However, the bottom plots show a situation in which the lossy correction equation is measurably superior. This is particularly clear when comparing model predictions to the dc average output voltage measurements. In both cases, the inclusion of either correction factor consistently improves accuracy with respect to the uncorrected model.

The results in Fig. 9 show that the proposed modeling framework improves on the accuracy of the original model. However, these results use large-signal model predictions. To assess the small-signal accuracy of the models, frequency-domain predictions are com-

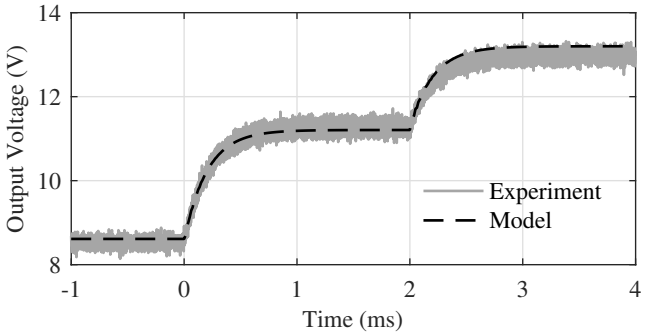

Figure 7. Open-loop voltage transient response for step changes in control inputs for triple phase shift modulation. At $t = 0$ ms d_s changes from 0.5 to 0.75; at $t = 2$ ms, and d_p changes from 0.5 to 0.75.

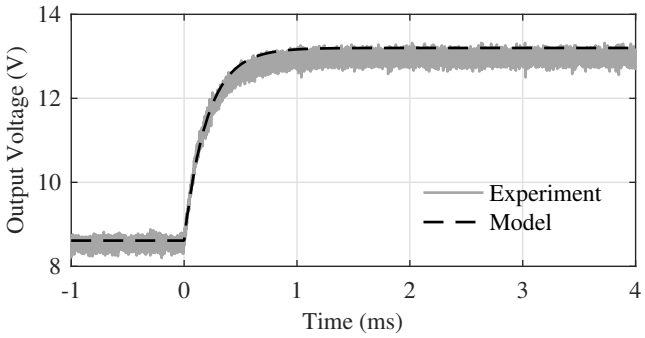

Figure 8. Open-loop voltage transient response for step changes in control inputs for dual phase shift modulation. At $t = 0$ ms d_p (and d_s) changes from 0.5 to 0.75.

pared to ac sweep analyses from switching simulations. The focus of the assessment is control-to-output transfer functions. In triple phase shift modulation there are three relevant control-to-output transfer functions, representing the effect of perturbations in each of the three control inputs on the output voltage. Similarly, there are two relevant control-to-output transfer functions for dual phase shift modulation, and one for single phase shift modulation. Magnitude plots of the frequency responses for each modulation strategy are shown in Fig. 10. Parameters used in the switching simulation are shown in Table 1. Simulations include nonideal behaviors such as dead time, control delays, and converter lossess. The control inputs for each modulation strategy were chosen such that the steady-state output voltage would be approximately 28 V in all three cases. For the triple phase shift case, the

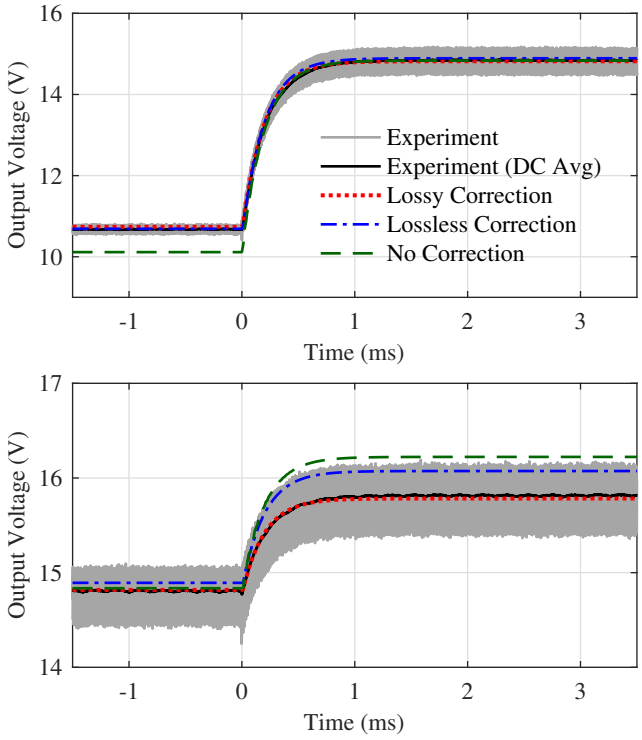

Figure 9. Open-loop voltage transient response for step changes in phase shift. At $t = 0$ ms, d changes from 0.15 to 0.3 (top) and from 0.3 to 0.4 (bottom). Experimental results are shown as raw measurements and the dc average over a single switching period.

inputs were $d_\phi = 0.25$, $d_p = 0.435$, and $d_s = 0.85$. For the dual phase shift case, the inputs were $d_\phi = 0.25$, $d_p = d_s = 0.775$. For the single phase shift case, the inputs were $d_\phi = 0.2$, $d_p = d_s = 1$.

The final validation experiment considers the closed-loop transient response during a step change in voltage reference. The results are measured by logging data from the DSP during the experiment. This allows the sampled voltage and internal control variables to be observed experimentally. Data is logged from the DSP at a rate of 8 kHz. Load and hardware parameters are the same as those used in the previous tests, but the input voltage is fixed at 17 V. Results are shown in Fig. 11. The top plot shows sampled voltage and the bottom shows the phase shift calculated by the controller. Because a closed-loop system is used, the phase shift is not specified as an exogenous input. Instead, it is calculated internally as the output of the voltage controller. The action of the controller ensures that in steady-state,

Table 3. Simulation Parameters

Parameter	Value	Parameter	Value
C_{in}	40 μF	C_o	200 μF
L_t	4 μH	R_t	0.01 Ω
$n_1 : n_2$	1 : 1	R_{sh}	5 Ω
v_{in}	30 V	i_{L0}	2 A

the output voltage is equal to the voltage reference. In terms of the model equations, the steady-state condition $v_{o0} = v_{ref}$ allows even the original model to predict output voltage with zero steady-state error. This is shown in the top plot of Fig. 11. However, in order to satisfy this relationship, all of the error due to the first harmonic approximation is confined to the phase shift. In contrast, the proposed modeling framework is able to predict both phase shift and output voltage accurately. This is a significant advantage in analyzing converter behavior. For instance, ZVS conditions for DAB converters are typically specified in terms of phase shift and voltage conversion ratio. The improved model is therefore capable of identifying ZVS operation, whereas the large-signal error of the original model precludes this type of analysis.

7. CONCLUSION

The modeling framework proposed in this study extends the functionality of existing GAM-based DAB models without significantly increasing complexity. The new framework improves on the original model by including more general modulation strategies and by eliminating steady-state errors caused by the truncation of the Fourier series. This produces fully continuous-time models that are accurate over a wide range of converter operating conditions. The framework is proposed as a general tool: it is applicable to both open and closed-loop operation and supports both large and small-signal model development.

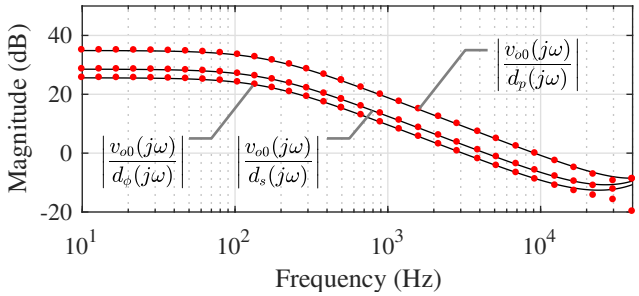

(a) TPS Control-to-Output Transfer Functions

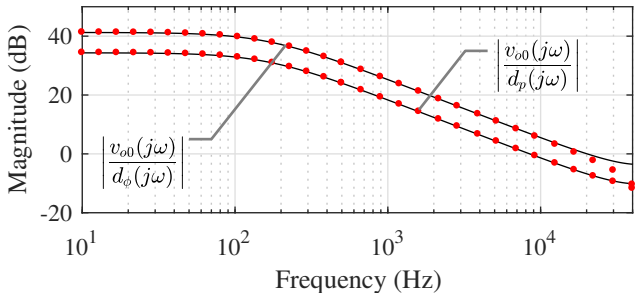

(b) DPS Control-to-Output Transfer Functions

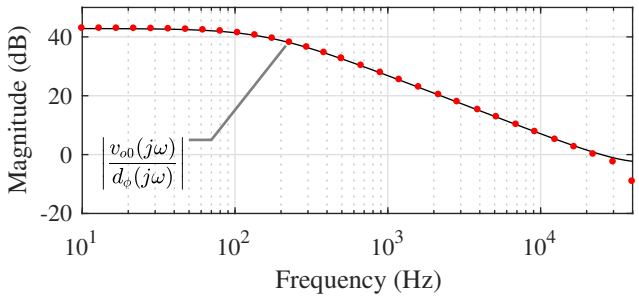

(c) SPS Control-to-Output Transfer Function

Figure 10. Magnitude responses of control-to-output transfer functions. Model predictions are shown as solid lines, dots indicate results of switching simulations.

While the methods proposed here are useful for modeling a single converter, one of the motivations driving this line of research is the development of computationally efficient models for multi-converter systems. The large-signal accuracy of the proposed framework opens the door for system-level applications, and methods for semi-explicit DAE models are already well established in traditional power system analysis. Future work in this study will

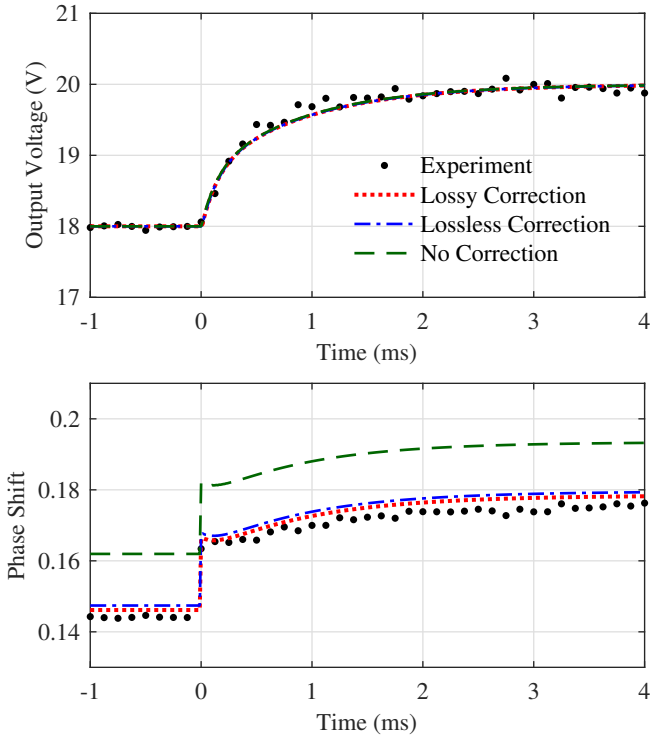

Figure 11. Closed-loop transient response for step change reference voltage. At $t = 0$ ms, v_{ref} changes from 18 V to 20 V. Plots show output voltage (top) and closed-loop phase shift (bottom).

continue to explore the challenges of system-level model construction, with the objective of identifying methods and models that are accessible to both power electronics and power systems research communities.

APPENDIX

Consider the linearization of $f(x, y, u)$ and $g(x, y, u)$. Large-signal states/inputs (x, y, u) can be broken into steady-state operating points (denoted by capital letters) and small-signal deviations.

$$x = X + \tilde{x}, \quad y = Y + \tilde{y}, \quad u = U + \tilde{u} \tag{101}$$

The first order Taylor series expansion of $f(\cdot)$ is

$$\dot{x} = \dot{X} + \dot{\tilde{x}} \approx f(X, Y, U) + \frac{\partial f}{\partial x}\tilde{x} + \frac{\partial f}{\partial y}\tilde{y} + \frac{\partial f}{\partial u}\tilde{u} \tag{102}$$

where $\frac{\partial f}{\partial x}$, $\frac{\partial f}{\partial y}$, and $\frac{\partial f}{\partial u}$ are evaluated at (X, Y, U). By definition, $\dot{X} = f(X, Y, U) = 0$, so

$$\dot{\tilde{x}} = \frac{\partial f}{\partial x}\tilde{x} + \frac{\partial f}{\partial y}\tilde{y} + \frac{\partial f}{\partial u}\tilde{u} \tag{103}$$

Similarly, the Taylor series expansions of $g(\cdot)$ is

$$0 = g(X, Y, U) + \frac{\partial g}{\partial x}\tilde{x} + \frac{\partial g}{\partial y}\tilde{y} + \frac{\partial g}{\partial u}\tilde{u} \tag{104}$$

Again, derivatives are evaluated at (X, Y, U), and $0 = g(X, Y, U)$. An expression for $\tilde{y}$ may be found by rearranging this equation.

$$\tilde{y} = \left(\frac{\partial g}{\partial y}\right)^{-1}\left(-\frac{\partial g}{\partial x}\tilde{x} - \frac{\partial g}{\partial u}\tilde{u}\right) \tag{105}$$

Substituting this expression into (103) eliminates $\tilde{y}$. The resulting equation is

$$\dot{\tilde{x}} = \frac{\partial f}{\partial x}\tilde{x} - \frac{\partial f}{\partial y}\left(\frac{\partial g}{\partial y}\right)^{-1}\left(\frac{\partial g}{\partial x}\tilde{x} + \frac{\partial g}{\partial u}\tilde{u}\right) + \frac{\partial f}{\partial u}\tilde{u} \tag{106}$$

$$= A\tilde{x} + B\tilde{u} \tag{107}$$

where A and B correspond to the expressions in (79) and (80), respectively.

REFERENCES

[1] R. W. A. A. DeDoncker, D. M. Divan, and M. H. Kheraluwala, "A three-phase soft-switched high-power-density dc/dc converter for high-power applications," *IEEE Trans. Ind. Appl.*, vol. 27, no. 1, pp. 63–73, 1991.

[2] M. N. Kheraluwala, R. W. Gascoigne, D. M. Divan, and E. D. Baumann, "Performance characterization of a high-power dual active bridge dc-to-dc converter," *IEEE Trans. Ind. Appl.*, vol. 28, no. 6, pp. 1294–1301, 1992.

[3] G. C. Verghese, M. E. Elbuluk, and J. G. Kassakian, "A general approach to sampled-data modeling for power electronic circuits," *IEEE Trans. Power Electron.*, vol. PE-1, no. 2, pp. 76–89, 1986.

[4] C. Zhao, S. D. Round, and J. W. Kolar, "Full-order averaging modelling of zero-voltage-switching phase-shift bidirectional dc-dc converters," *IET Power Electronics*, vol. 3, no. 3, pp. 400–410, 2010.

[5] F. Krismer and J. W. Kolar, "Accurate small-signal model for the digital control of an automotive bidirectional dual active bridge," *IEEE Trans. Power Electron.*, vol. 24, no. 12, pp. 2756–2768, 2009.

[6] L. Shi, W. Lei, Z. Li, J. Huang, Y. Cui, and Y. Wang, "Bilinear discrete-time modeling and stability analysis of the digitally controlled dual active bridge converter," *IEEE Trans. Power Electron.*, vol. 32, no. 11, pp. 8787–8799, 2017.

[7] A. Rodríguez, A. Vázquez, D. G. Lamar, M. M. Hernando, and J. Sebastián, "Different purpose design strategies and techniques to improve the performance of a dual active bridge with phase-shift control," *IEEE Trans. Power Electron.*, vol. 30, no. 2, pp. 790–804, 2015.

[8] H. Qin and J. W. Kimball, "Solid-state transformer architecture using ac-ac dual-active-bridge converter," *IEEE Trans. Ind. Electron.*, vol. 60, no. 9, pp. 3720–3730, 2013.

[9] B. Hua, M. Chunting, W. Chongwu, and S. Gargies, "The dynamic model and hybrid phase-shift control of a dual-active-bridge converter," in *2008 34th Annual Conference of IEEE Industrial Electronics*, 2008, pp. 2840–2845.

[10] R. D. Middlebrook and S. Cuk, "A general unified approach to modelling switching-converter power stages," in *1976 IEEE Power Electronics Specialists Conference*, 1976, pp. 18–34.

[11] K. Zhang, Z. Shan, and J. Jatskevich, "Large- and small-signal average-value modeling of dual-active-bridge dc-dc converter considering power losses," *IEEE Trans. Power Electron.*, vol. 32, no. 3, pp. 1964–1974, 2017.

[12] F. Zhang, M. M. U. Rehman, R. Zane, and D. Maksimović, "Improved steady-state model of the dual-active-bridge converter," in *2015 IEEE Energy Conversion Congress and Exposition (ECCE)*, 2015, pp. 630–636.

[13] H. Qin and J. W. Kimball, "Generalized average modeling of dual active bridge dc-dc converter," *IEEE Trans. Power Electron.*, vol. 27, no. 4, pp. 2078–2084, 2012.

[14] S. R. Sanders, J. M. Noworolski, X. Z. Liu, and G. C. Verghese, "Generalized averaging method for power conversion circuits," *IEEE Trans. Power Electron.*, vol. 6, no. 2, pp. 251–259, 1991.

[15] S. Cooper, A. Klem, M. H. Nehrir, and H. Ga, "An improved state-space averaged model of a dual active bridge converter for use in acausal system modeling," in *2016 North American Power Symposium (NAPS)*, 2016, pp. 1–5.

[16] S. S. Shah and S. Bhattacharya, "Large & small signal modeling of dual active bridge converter using improved first harmonic approximation," in *2017 IEEE Applied Power Electronics Conference and Exposition (APEC)*, 2017, pp. 1175–1182.

[17] J. A. Mueller and J. W. Kimball, "Model-based determination of closed-loop input impedance for dual active bridge converters," in *2017 IEEE Applied Power Electronics Conference and Exposition (APEC)*, March 2017, pp. 1039–1046.

[18] J. Huang, Y. Wang, Z. Li, and W. Lei, "Unified triple-phase-shift control to minimize current stress and achieve full soft-switching of isolated bidirectional dc-dc converter," *IEEE Trans. Ind. Electron.*, vol. 63, no. 7, pp. 4169–4179, 2016.

[19] B. Zhao, Q. Song, and W. Liu, "Power characterization of isolated bidirectional dual-active-bridge dc-dc converter with dual-phase-shift control," *IEEE Trans. Power Electron.*, vol. 27, no. 9, pp. 4172–4176, 2012.

[20] B. Zhao, Q. Yu, and W. Sun, "Extended-phase-shift control of isolated bidirectional dc-dc converter for power distribution in microgrid," *IEEE Trans. Power Electron.*, vol. 27, no. 11, pp. 4667–4680, 2012.

[21] M. L. Crow, "Numerical integration," in *Computational Methods for Electric Power Systems*, 3rd ed. Boca Raton, FL: CRC Press, 2016.

[22] P. T. Krein, J. Bentsman, R. M. Bass, and B. L. Lesieutre, "On the use of averaging for the analysis of power electronic systems," *IEEE Trans. Power Electron.*, vol. 5, no. 2, pp. 182–190, 1990.

[23] D. Gonzalez-Agudelo, A. Escobar-Mejía, and H. Ramirez-Murrillo, "Dynamic model of a dual active bridge suitable for solid state transformers," in *2016 13th International Conference on Power Electronics (CIEP)*, 2016, pp. 350–355.

[24] B. Zhao, Q. Song, W. Liu, and Y. Sun, "Dead-time effect of the high-frequency isolated bidirectional full-bridge dc-dc converter: Comprehensive theoretical analysis and experimental verification," *IEEE Trans. Power Electron.*, vol. 29, no. 4, pp. 1667–1680, 2014.

[25] D. Segaran, D. G. Holmes, and B. P. McGrath, "Enhanced load step response for a bidirectional dc-dc converter," *IEEE Trans. Power Electron.*, vol. 28, no. 1, pp. 371–379, 2013.

II. MODELING DUAL ACTIVE BRIDGE CONVERTERS IN DC DISTRIBUTION SYSTEMS

Jacob A. Mueller and Jonathan W. Kimball

Department of Electrical & Computer Engineering

Missouri University of Science and Technology

Rolla, Missouri 65409–0050

Email: jam8z4@mst.edu

ABSTRACT

Modeling improvements are proposed for systems containing dual active bridge (DAB) converters. First, a systematic approach to constructing models of multi-converter systems is described. The method generates continuous-time large-signal average models that are suitable for system-level analysis and efficient time-domain simulation. Although the base DAB models are derived using generalized average modeling (GAM), the system-level construction does not require the specification of a base period. Secondly, a method of reconstructing currents in the high-frequency DAB transformer is proposed. This method significantly improves accuracy in modeling transformer current, which is a critical weakness of DAB models derived using GAM. Furthermore, the method is applied offline as needed, so it does not affect the computational complexity of time-domain simulation. Both the system-level model construction procedure and harmonic reconstruction method are validated in switching simulations and hardware experiments.

Keywords: average modeling, dual active bridge converter, generalized average model, phase shift modulation

1. INTRODUCTION

Dual active bridge (DAB) converters are well-suited to applications in power distribution systems due to their high power density, low device stresses, galvanic isolation, and bidirectional operation [1, 2]. DAB converters have been considered as a candidate topology for solid-state transformers [3, 4] and have been studied in the context of automotive [5], aerospace [6], and marine power systems [7, 8]. In all of these applications, the ability to accurately describe the behavior of the DAB converter–and its interactions with other converters in the system–is of critical importance. System-level analyses, such as stability assessments and time-domain simulation, depend on models that are both accurate and scalable. This study is concerned with the development of models that meet these criteria.

Modeling DAB converters is difficult due to the presence of a high-frequency ac conversion stage and ac state variables. The most popular strategy for dealing with this challenge is to employ the sampled-data modeling method from [9]. This method produces discrete-time models that provide exact state solutions for each sub-interval within the base switching period. Models of this type are described in [10, 11, 5], among others. However, this modeling approach assumes that the system cycles through a set of switching modes at some base period, and requires explicit descriptions of each mode. These requirements are trivial for a single converter, but more complicated when the system consists of multiple converters, particularly when converters operate at different switching frequencies.

Continuous-time DAB models have been proposed as well, using both state-space averaging and generalized averaging methods. Those derived using classical state-space averaging either eliminate the ac transformer current state during the averaging process (as in [12]), or represent the transformer by averaging the current into and out of the dual H-bridge circuits [13, 14]. The disadvantage of these models is inherited from the basic averaging framework: the models are derived by calculating the dc average over each switching period and are therefore limited in their ability to represent dynamics at higher frequencies [13].

Generalized average modeling (GAM) provides fully continuous-time representations that are capable of describing ac state variables [15]. This is accomplished by expanding state variables into Fourier series components. A DAB model derived using GAM was proposed in [16]. To achieve a balance of accuracy and complexity, this model was derived under a first harmonic approximation, i.e. with the Fourier series truncated at the first harmonic. The resulting model was accurate for small-signal disturbances, but inaccurate at steady-state due to the first harmonic approximation. A corrective modification was proposed in [17], leading to an improved large-signal model that is accurate in both transient and steady-state operation. While the new model addresses large-signal error, it is still subject to limitations of the first harmonic approximation. In particular, the transformer current state is represented using only the first harmonic of its Fourier series, i.e. as a sinusoid at the converter switching frequency.

Of the modeling approaches described here, the GAM framework is the most appropriate for developing system-level models. GAM methods for constructing models of multi-converter systems are available in existing literature [18]. In general, GAM complexity scales poorly with system size [19], and the foremost challenge is preserving model tractability. For instance, in [7], both state-space averaging and GAM were used to derive large-signal models of a shipboard power system. The authors conclude that, despite greater accuracy, the model derived using GAM is less suitable for efficient time-domain simulation due to high computational complexity. However, in the case of a DAB converter it is possible to mitigate scalability issues using structural properties of the model. In particular, the state equations of the original model in [16] are decoupled along lines of physical relevance, making it possible to consider only the states of interest in the final model. The same decoupling effect exists for systems of multiple DAB converters as well [20].

This study presents two contributions. The first is a method of constructing accurate and scalable models of systems containing multiple DAB converters. Models generated using this method are suitable for fast time-domain simulation or linearization for small-

signal stability analysis. The method is presented in the context of a dc distribution system that contains only DAB converters, though the modeling approach itself does not preclude other converter topologies. The second contribution is a procedure for reconstructing exact transformer currents (and the currents in other converter elements) from the simplified first harmonic representation. The reconstruction process is applied offline, so it improves the fidelity of time-domain state solutions without affecting computational complexity. Both contributions support the development of accurate and efficient representations of DAB converters in multi-converter systems.

The structure of the paper is as follows. Section 2 describes the large-signal DAB model, which is used as a modular element of the system-level model. Section 3 discusses the model construction procedure. The method of reconstructing transformer currents is proposed in Section 4. Verification experiments are discussed in Section 5.

2. BASE DAB CONVERTER MODEL

2.1. GAM Framework. The GAM approach begins with the Fourier series representation of a state variable. For generic state variable $z(t)$, the Fourier series representation is

$$z(t) = \sum_{k=-\infty}^{\infty} \langle z \rangle_k(t) e^{j\omega k t} \tag{1}$$

where f_s is the converter switching frequency and $\omega = 2\pi f_s$. The angle-bracket term $\langle z \rangle_k(t)$ is the k^{th} harmonic coefficient, and is defined by a sliding average over the switching period, T.

$$\langle z \rangle_k(t) = \frac{1}{T} \int_{t-T}^{t} z(\tau) e^{-j\omega k \tau} d\tau \tag{2}$$

These are the generalized averaging operations that define GAM. Classical state-space averaging may be viewed as a special case of the GAM framework, in which only $k = 0$ terms are considered. The dc average component $\langle z \rangle_0(t)$ is equivalent to the representation of $z(t)$ in a model derived using classical state space averaging.

Two additional relationships are used in the application of GAM [15, 21]. The derivative of the harmonic coefficients is given by

$$\frac{d}{dt}\langle z\rangle_k(t) = \left\langle \frac{d}{dt} z \right\rangle_k (t) - j\omega k \langle z\rangle_k(t). \tag{3}$$

The product of coefficients is

$$\langle z \cdot y\rangle_k(t) = \sum_{i=-\infty}^{\infty} \langle z\rangle_{k-i}(t) \cdot \langle y\rangle_i(t). \tag{4}$$

Under a first harmonic approximation, ($k = 0, \pm 1$) the time-domain state may be recovered from the harmonic components as

$$\begin{aligned} z(t) &= \langle z\rangle_1(t)e^{j\omega t} + \langle z\rangle_{-1}(t)e^{-j\omega t} + \langle z\rangle_0(t) \\ &= 2\big(\langle z\rangle_R(t)\cos\omega t - \langle z\rangle_I(t)\sin\omega t\big) + \langle z\rangle_0(t) \end{aligned} \tag{5}$$

where $\langle z\rangle_R(t) = \Re[\langle z\rangle_1(t)]$ and $\langle z\rangle_I(t) = \Im[\langle z\rangle_1(t)]$ are the real and imaginary components of the first harmonic coefficient. This approximation limits both the complexity and large-signal accuracy of the final model, since higher-order terms are neglected. However, in the case of a DAB converter, the large-signal error may be corrected through the use of an algebraic correction factor [17].

2.2. Single Converter Model. This study uses the improved DAB model from [17] as a fundamental building block for the construction of a system level model. The model in [17] is based on [16], but includes a correction factor to eliminate large-signal errors introduced by the first harmonic approximation. The correction equation does not change the model state equations, so the original formulation in [16] is relevant to the present discussion. Since the objective is to analyze the converter behavior in a full system, the closed-loop formulation is used. A diagram of the converter and control system is shown in Fig. 1.

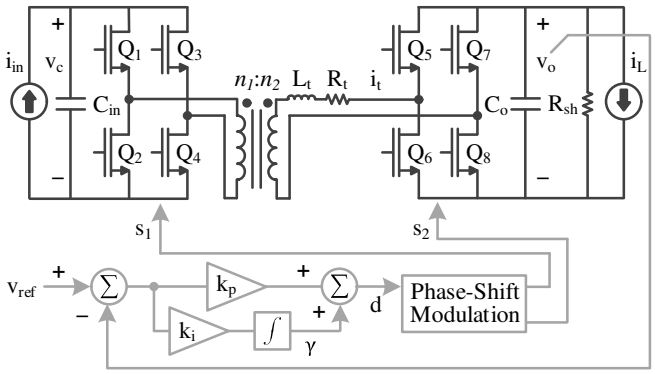

Figure 1. Voltage-controlled DAB converter and control system

Before applying the GAM framework, the state equations are:

$$\dot{v}_c = \frac{1}{C_{in}} i_{in} - \frac{1}{C_{in}} s_1 i_t \tag{6}$$

$$\dot{v}_o = \frac{-1}{R_{sh} C_o} v_o + \frac{1}{C_o} i_t s_2 - \frac{1}{C_o} i_L \tag{7}$$

$$\dot{i}_t = \frac{1}{L_t} v_{in} s_1 - \frac{1}{L_t} v_o s_2 - \frac{R_t}{L_t} i_t \tag{8}$$

Dot notation is used in these equations to denote time derivatives, and hardware and control parameters are identified in Fig. 1. When a voltage source is used instead of a current source, v_c is simply replaced by v_{in}, and (6) is eliminated. Switching functions s_1 and s_2 are

$$s_1 = \begin{cases} 1, & 0 \le \tau < \frac{T}{2} \\ -1, & \frac{T}{2} \le \tau < T \end{cases} \tag{9}$$

$$s_2 = \begin{cases} 1, & \frac{dT}{2} \le \tau < \frac{dT}{2} + \frac{T}{2} \\ -1, & 0 \le \tau < \frac{dT}{2} \quad \text{or} \quad \frac{dT}{2} + \frac{T}{2} \le \tau < T \end{cases} \tag{10}$$

where τ is the time within a single switching period and d is the converter phase shift.

Next the GAM framework is applied. In the following equations, angle brackets for GAM states are dropped in the interest of readability, and states are identified using subscripts. For example, the dc average of generic state z is denoted z_0; real and imaginary

components of the first harmonic component are denoted z_R and z_I, respectively. This notation is used for the remainder of the paper. To further simplify notation, transformers are assumed to have a $1:1$ turns ratio throughout.

The state and input vectors of the model are

$$x = [v_{c0} \quad v_{o0} \quad i_{tR} \quad i_{tI} \quad \gamma_0]^T \tag{11}$$

$$u = [i_{in0} \quad i_{L0} \quad v_{ref}]^T \tag{12}$$

The GAM state equations are:

$$\dot{v}_{c0} = \frac{1}{C_{in}} i_{in0} + \frac{4}{C_{in}\pi} i_{tI} \tag{13}$$

$$\dot{v}_{o0} = \frac{-1}{R_{sh}C_o} v_{o0} - \frac{4\sin\pi\hat{d}}{C_o\pi} i_{tR} - \frac{4\cos\pi\hat{d}}{C_o\pi} i_{tI} - \frac{1}{C_o} i_{L0} \tag{14}$$

$$\dot{i}_{tR} = \frac{2\sin\pi\hat{d}}{L_t\pi} v_{o0} - \frac{R_t}{L_t} i_{tR} + \omega i_{tI} \tag{15}$$

$$\dot{i}_{tI} = \frac{2\cos\pi\hat{d}}{L_t\pi} v_{o0} - \omega i_{tR} - \frac{R_t}{L_t} i_{tI} - \frac{2}{L_t\pi} v_{c0} \tag{16}$$

$$\dot{\gamma}_0 = k_i \left(v_{ref} - v_{o0}\right) \tag{17}$$

Again, in the case of a voltage source, v_{c0} is replaced by v_{in0} in (16), i_{in0} is replaced by v_{in0} in (12), and state equation (13) becomes unnecessary.

Note that the phase shift arguments in (13)–(17) appear as $\hat{d}$, whereas phase shift appears as d in (9), (10), and Fig. 1. This difference is intentional: for a given input voltage/current and load, the phase shift value that satisfies the equilibrium solution of the model equations ($\hat{d}$) is not the same as the corresponding phase shift observed in switching simulations or hardware experiments (d). If the two are assumed to be equal, the state equations above will be affected by persistent steady-state error, and the large-signal model will be inaccurate [13, 22].

A correction factor was proposed in [17] as an algebraic function of the two phase shift variables. The actual phase shift, d, is the output of the voltage controller.

$$d = k_p(v_{ref} - v_{o0}) + \gamma_0 \tag{18}$$

The model equilibrium phase shift, $\hat{d}$, is represented internally as an algebraic state. The relationship between $\hat{d}$ and the rest of the model is described by

$$\begin{aligned} 0 = g(x, \hat{d}, u) = &- v_{c0}R_t \cos \pi\hat{d} - v_{c0}X_t \sin \pi\hat{d} + v_{o0}R_t + K\left(v_{c0} - v_{o0}\right)\theta + Kv_{o0}\tanh\theta \\ &+ Kv_{c0}\frac{d}{|d|}\left(1 - 2\theta d - \operatorname{sech}\theta \exp\left(\frac{d}{|d|}\theta - 2\theta d\right)\right) \end{aligned} \tag{19}$$

where $X_t = \omega L_t$ is transformer reactance and K and θ are the following hardware constants.

$$K = \frac{\pi}{4}\frac{X_t(R_t^2 + X_t^2)}{R_t^2} \tag{20}$$

$$\theta = \frac{\pi R_t}{2X_t} \tag{21}$$

The full large-signal model is a system of differential algebraic equations with the form

$$\dot{x} = f(x, \hat{d}, u) \tag{22}$$

$$0 = g(x, \hat{d}, u), \tag{23}$$

where $f(\cdot)$ contains (13)–(17) and $g(\cdot)$ is defined in (19).

2.3. Decoupling Effect and Selective Averaging. Under the first harmonic approximation, each variable z is broken into three components corresponding to the $k = 0, \pm 1$ averages or, equivalently, z_0, z_R, and z_I. However, only a subset of these appear in the state and input vectors (11). Namely, the dc states (capacitor voltages and integrator) are represented only be dc average ($k = 0$) terms, while the ac transformer currents are repre-

sented by the $k = \pm 1$ terms. This is because the remaining terms are decoupled from states the in (11) [16]. Furthermore, the influence of ac inputs (namely i_{inR}, i_{inI}, i_{oR}, and i_{oI}) is entirely confined to the decoupled states.

In previous studies, the number of Fourier series terms used to represent each state variable was selected according to the dominant dynamics of that state [18]. This is referred to as "selective averaging," and it assumes some *a priori* knowledge of system dynamics. If this process were applied to the DAB model, only the transformer current would be modeled by $k = \pm 1$ terms, since it is the only ac state. Conveniently, the structural properties of the DAB model provide this exact result without the use of assumptions to selectively eliminate undesirable terms.

The real importance of the decoupling effect is that the terminal characteristics of each converter may be represented by dc average terms only without sacrificing model validity. This has significant implications for the system-level model. Interactions between each converter and the rest of the system may be described using dc average states and equations. The $k = \pm 1$ components of these interactions, which are frequency dependent, may be safely ignored. More precisely, when included in the derivation of the system-level model, the $k = \pm 1$ components of terminal voltages and line currents are contained in a subsystem that is decoupled from the dc average line currents and the states in (11). This was shown in [20], an earlier version of this study. Modeling the frequency dependent interactions of this subsystem would require the specification of a system-wide base period, and would undercut the scalability and modularity objectives of the model construction process. Since it is possible to neglect these interactions from the model with no ill effect, the methods shown here focus on dc average interactions and states in (11). The following section describes a procedure that operates directly on the models in (22). The method results in the same final model as the derivation shown in [20], but is simpler and more concise.

3. SYSTEM-LEVEL MODEL

The model construction procedure described in this section uses the large-signal converter model as a modular building block. The system under consideration consists of N converters and M buses. An example system with $N = 5$ and $M = 7$ is shown in Fig. 2 for the purpose of converter and bus numbering schemes. All converters are bidirectional and may connect to the system through the controlled output terminal, uncontrolled input terminal, or both. Superscripts are used to identify states, inputs, and parameters pertaining to each converter, e.g. x^n refers to the state vector of converter n.

3.1. Model Combination. The system has M buses, where $M \geq N$. Each bus may correspond to a converter input or output terminal or to a structural node with no converter present (e.g. bus 5 in Fig. 2). The lines in the system may be resistive or resistive/inductive. The latter is described, since it is more general. The line current between buses i and j is described by

$$i_{\ell 0}^{ij} = \frac{1}{L_{ij}}(v_{b0}^{i} - v_{b0}^{j}) - \frac{R_{ij}}{L_{ij}} i_{\ell 0}^{ij} \tag{24}$$

where v_{b0}^{i} and v_{b0}^{j} are the dc average voltages at buses i and j, R_{ij} and L_{ij} are the resistance and inductance of the line, and $i < j$ by convention.

To construct the system-level model, the points of interaction between the converters and the rest of the system must be expressed in terms of state variables. Specifically, the system-level model must incorporate self-contained descriptions of the output currents for all converters connected by output terminal, input currents of all converters connected by input terminal, and all bus voltages. This is done on a bus-by-bus basis. When bus m corresponds to the output terminal of converter n, the converter output current is:

$$i_{L0}^{n} = -\sum_{i=1}^{m-1} i_{\ell 0}^{mi} + \sum_{j=m+1}^{M} i_{\ell 0}^{mj} \tag{25}$$

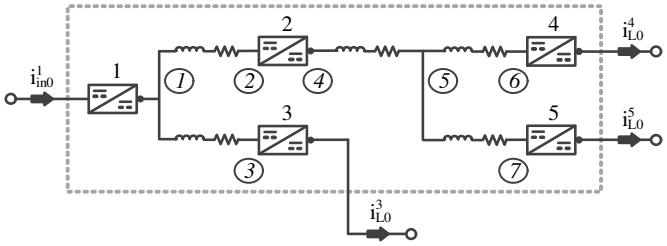

Figure 2. Five-converter example system. Each converter is shown a two-port element, with the (controlled) output port denoted by a dot. Encircled integers are system bus numbers. The dotted line indicates the scope of the system-level model.

This follows from the application of KCL at bus m. Trivially, the bus voltage is equal to the converter output voltage, i.e. $v^m_{b0} = v^n_{o0}$. Similarly, when bus m corresponds to the input terminal of converter n, the converter input current is:

$$i^n_{in0} = \sum_{i=1}^{m-1} i^{mi}_{\ell 0} - \sum_{j=m+1}^{M} i^{mj}_{\ell 0}, \tag{26}$$

In this case, the bus voltage is equal to the input capacitor voltage ($v^m_{b0} = v^n_{c0}$).

In the final case, bus m is not connected to a converter. Bus 5 in Fig. 2 is an example of this case. By KCL, the current at this node is:

$$0 = \sum_{i=1}^{m-1} i^{mi}_{\ell 0} - \sum_{j=m+1}^{M} i^{mj}_{\ell 0} \tag{27}$$

Even though no converter is present, it is still necessary to represent the bus voltages in the model, since they are used in the line current equations. These bus voltages are included as algebraic state variables. For each bus m with no converter, the model contains both the voltage at the bus and the corresponding node current expression.

3.2. System-Level Organization. The full system-level model has the form

$$\dot{x}_{sys} = f_{sys}(x_{sys}, y_{sys}, u_{sys}) \tag{28}$$

$$0 = g_{sys}(x_{sys}, y_{sys}, u_{sys}) \tag{29}$$

The state vector x_{sys} is

$$x_{sys} = [x^1 \quad x^2 \quad \cdots \quad x^N \quad x_{line}]^T \tag{30}$$

where each x^n is a converter state vector and x_{line} is a vector containing all line current states. The algebraic state vector y_{sys} contains all internal phase shift variables and all bus voltages that are not already states in x_{sys}. The vector is

$$y_{sys} = [\hat{d}^1 \quad \hat{d}^2 \quad \cdots \quad \hat{d}^N \quad y_{bus}]^T \tag{31}$$

where y_{bus} contains the voltage v_{b0}^m of each bus m that does not correspond to the output terminal of a source converter or input terminal of a load converter.

The system-level input vector u_{sys} contains all N control inputs and all current inputs that are external to the system, i.e. all i_{in0}^n and i_{L0}^n not described by equations (25) and (26). The number of external connections depends on the topology of the system. For example, the input vector for the system shown in Fig. 2 is

$$u_{sys} = [i_{in0}^1 \;\; v_{ref}^1 \;\; v_{ref}^2 \;\; i_{L0}^3 \;\; v_{ref}^3 \;\; i_{L0}^4 \;\; v_{ref}^4 \;\; i_{L0}^5 \;\; v_{ref}^5]^T \tag{32}$$

The four current terms in this vector correspond to the four external connections shown in Fig. 2.

The system equations $f_{sys}(\cdot)$ are (13)–(17) for each converter and (24) for each line current. Likewise, the equations in $g_{sys}(\cdot)$ are (19) for each converter and (27) for each voltage in y_{bus}.

To use the system-level model, partial derivative matrices are needed. For convenience, define function $\dot{x}_{line} = f_{line}(\cdot)$ to include all line current state equations and $0 = g_{line}(\cdot)$ to include all algebraic KCL equations for buses not connected to converters.

The partial derivative matrices may then be described in terms of block submatrices.

$$\frac{\partial f_{sys}}{\partial x_{sys}} = \begin{bmatrix} \frac{\partial f^1}{\partial x^1} & \cdots & 0 & \frac{\partial f^1}{\partial x_{line}} \\ \vdots & \ddots & \vdots & \vdots \\ 0 & \cdots & \frac{\partial f^N}{\partial x^N} & \frac{\partial f^N}{\partial x_{line}} \\ \frac{\partial f_{line}}{\partial x^1} & \cdots & \frac{\partial f_{line}}{\partial x^N} & \frac{\partial f_{line}}{\partial x_{line}} \end{bmatrix} \tag{33}$$

$$\frac{\partial f_{sys}}{\partial y_{sys}} = \begin{bmatrix} \frac{\partial f^1}{\partial \hat{d}^1} & \cdots & 0 & 0 \\ \vdots & \ddots & \vdots & \vdots \\ 0 & \cdots & \frac{\partial f^N}{\partial \hat{d}^N} & 0 \\ 0 & \cdots & 0 & \frac{\partial f_{line}}{\partial y_{bus}} \end{bmatrix} \tag{34}$$

$$\frac{\partial g_{sys}}{\partial x_{sys}} = \begin{bmatrix} \frac{\partial g^1}{\partial x^1} & \cdots & 0 & 0 \\ \vdots & \ddots & \vdots & \vdots \\ 0 & \cdots & \frac{\partial g^N}{\partial x^N} & 0 \\ 0 & \cdots & 0 & \frac{\partial g_{line}}{\partial x_{line}} \end{bmatrix} \tag{35}$$

$$\frac{\partial g_{sys}}{\partial y_{sys}} = \begin{bmatrix} \frac{\partial g^1}{\partial \hat{d}^1} & \cdots & 0 & 0 \\ \vdots & \ddots & \vdots & \vdots \\ 0 & \cdots & \frac{\partial g^N}{\partial \hat{d}^N} & 0 \\ 0 & \cdots & 0 & 0 \end{bmatrix} \tag{36}$$

Each $\frac{\partial f^n}{\partial x^n}$ submatrix is the state matrix of converter n:

$$\frac{\partial f^n}{\partial x^n} = \begin{bmatrix} 0 & 0 & 0 & \frac{4}{\pi C_{in}^n} & 0 \\ 0 & \frac{-1}{R_{sh}^n C_o^n} & \frac{-4\sin\pi\hat{d}^n}{\pi C_o^n} & \frac{-4\cos\pi\hat{d}^n}{\pi C_o^n} & 0 \\ 0 & \frac{2\sin\pi\hat{d}^n}{\pi L_t^n} & \frac{-R_t^n}{L_t^n} & \omega^n & 0 \\ \frac{-2}{\pi L_t^n} & \frac{2\cos\pi\hat{d}^n}{\pi L_t^n} & -\omega^n & \frac{-R_t^n}{L_t^n} & 0 \\ 0 & -k_i^n & 0 & 0 & 0 \end{bmatrix} \tag{37}$$

The columns of $\frac{\partial f^n}{\partial x_{line}}$ and rows of $\frac{\partial f_{line}}{\partial x^n}$ are

$$\frac{\partial f^n}{\partial i_{\ell 0}^{ij}} = \begin{bmatrix} \frac{\partial(\dot{v}_{c0}^n)}{\partial i_{\ell 0}^{ij}} & \frac{\partial(\dot{v}_{o0}^n)}{\partial i_{\ell 0}^{ij}} & 0 & 0 & 0 \end{bmatrix}^T \tag{38}$$

$$\frac{\partial(\dot{i}_{\ell 0}^{ij})}{\partial x^n} = \begin{bmatrix} \frac{\partial(\dot{i}_{\ell 0}^{ij})}{\partial v_{c0}^n} & \frac{\partial(\dot{i}_{\ell 0}^{ij})}{\partial v_{o0}^n} & 0 & 0 & 0 \end{bmatrix} \tag{39}$$

The elements of these vectors depend on how converter n connects to the system. For generality, let the input and output terminals of converter n correspond to buses p and q, respectively. Then $v_{b0}^p = v_{c0}^n$ and $v_{b0}^q = v_{o0}^n$, and the partial derivative elements are:

$$\frac{\partial(\dot{v}_{c0}^n)}{\partial i_{\ell 0}^{ij}} = \begin{cases} \frac{-1}{C_{in}^n}, & p = i \\ \frac{1}{C_{in}^n}, & p = j \\ 0, & \text{else} \end{cases} \qquad \frac{\partial(\dot{v}_{o0}^n)}{\partial i_{\ell 0}^{ij}} = \begin{cases} \frac{1}{C_o^n}, & q = i \\ \frac{-1}{C_o^n}, & q = j \\ 0, & \text{else} \end{cases}$$

$$\frac{\partial(\dot{i}_{\ell 0}^{ij})}{\partial v_{c0}^n} = \begin{cases} \frac{1}{L_{ij}}, & i = p \\ \frac{-1}{L_{ij}}, & j = p \\ 0, & \text{else} \end{cases} \qquad \frac{\partial(\dot{i}_{\ell 0}^{ij})}{\partial v_{o0}^n} = \begin{cases} \frac{1}{L_{ij}}, & i = q \\ \frac{-1}{L_{ij}}, & j = q \\ 0, & \text{else} \end{cases}$$

Finally, submatrix $\frac{\partial f_{line}}{\partial x_{line}}$ is diagonal with elements

$$\frac{\partial(\dot{i}_{\ell 0}^{ij})}{\partial i_{\ell 0}^{ij}} = -\frac{R_{ij}}{L_{ij}}. \tag{40}$$

The nonzero submatrices of $\frac{\partial f_{sys}}{\partial y_{sys}}$ are $\frac{\partial f^n}{\partial \hat{d}^n}$ and $\frac{\partial f_{line}}{\partial y_{bus}}$. Each $\frac{\partial f^n}{\partial \hat{d}^n}$ is a column:

$$\frac{\partial f^n}{\partial \hat{d}^n} = \begin{bmatrix} 0 \\ \frac{4}{C_o^n}\left(i_{tI}^n \sin \pi\hat{d}^n - i_{tR}^n \cos \pi\hat{d}^n\right) \\ \frac{2v_{o0}^n \cos \pi\hat{d}^n}{L_t^n} \\ \frac{-2v_{o0}^n \sin \pi\hat{d}^n}{L_t^n} \end{bmatrix} \tag{41}$$

Submatrix $\frac{\partial f_{line}}{\partial y_{bus}}$ consists of elements $\frac{\partial (i^{ij}_{\ell 0})}{\partial v^m_{b0}}$ for each line current $i^{ij}_{\ell 0} \in x_{line}$ and bus voltage $v^m_{b0} \in y_{bus}$. These elements are:

$$\frac{\partial (i^{ij}_{\ell 0})}{\partial v^m_{b0}} = \begin{cases} \frac{1}{L_{ij}}, & i = m \\ \frac{-1}{L_{ij}}, & j = m \\ 0, & \text{else} \end{cases} \tag{42}$$

Matrix $\frac{\partial g_{sys}}{\partial x_{sys}}$ is a block diagonal combination of submatrices $\frac{\partial g^n}{\partial x^n}$ and $\frac{\partial g^m_{line}}{\partial x_{line}}$. The former is

$$\frac{\partial g^n}{\partial x^n} = \begin{bmatrix} \frac{\partial g^n}{\partial v^n_{c0}} & R^n_t - K^n \left(\theta^n - \tanh \theta^n\right) & 0 & 0 & \frac{\partial g^n}{\partial d^n} \end{bmatrix} \tag{43}$$

where $\frac{\partial g^n}{\partial v^n_{c0}}$ and $\frac{\partial g^n}{\partial d^n}$ are

$$\begin{aligned} \frac{\partial g^n}{\partial v^n_{c0}} &= K^n \theta^n - R^n_t \cos \pi \hat{d}^n - X^n_t \sin \pi \hat{d}^n \\ &\quad + K^n \frac{d^n}{|d^n|} \left(1 - 2\theta^n d^n - \operatorname{sech} \theta^n \exp\left(\frac{d^n}{|d^n|}\theta^n - 2\theta^n d^n\right)\right) \end{aligned} \tag{44}$$

$$\frac{\partial g^n}{\partial d^n} = \frac{2 d^n \theta K^n v^n_{c0}}{|d^n|} \left(\operatorname{sech} \theta^n \exp\left(\frac{d^n}{|d^n|}\theta^n - 2\theta^n d^n\right) - 1\right) \tag{45}$$

Submatrix $\frac{\partial g^m_{line}}{\partial x_{line}}$ has elements $\frac{\partial g^m_{line}}{\partial i^{ij}_{\ell 0}}$, where $g^m_{line}(\cdot)$ denotes the KCL equation applied at bus m. These elements are:

$$\frac{\partial g^m_{line}}{\partial i^{ij}_{\ell 0}} = \begin{cases} 1, & m = i \\ -1, & m = j \\ 0, & \text{else} \end{cases} \tag{46}$$

The last matrix $\frac{\partial g_{sys}}{\partial y_{sys}}$ has only diagonal elements $\frac{\partial g^n}{\partial \hat{d}^n}$, which are:

$$\frac{\partial g^n}{\partial \hat{d}^n} = \pi v^n_{c0} \left(R^n_t \sin \pi \hat{d}^n - X^n_t \cos \pi \hat{d}^n\right) \tag{47}$$

4. TRANSFORMER CURRENT RECONSTRUCTION

The preceding sections have described a general-purpose large-signal model. This section is concerned with improving the fidelity of the time-domain transformer current representations. The following analysis is applicable to any converter in the system; superscript n is dropped for readability. Let v_c, v_o, i_t, and d be state trajectories resulting a time-domain simulation of the proposed model. The voltages and phase shift are dc average variables, so the state trajectories are give trivially by the states of the proposed model. The transformer current is calculated from states i_{tR} and i_{tI} according to (5). The result is a sinusoidal approximation of the transformer current. This approximation is suitable for efficient small-signal analyses, but for many other purposes, such as evaluating device current stresses or analyzing ZVS conditions, more accurate current representations are required. As a direct consequence of the correction factor equations used in the proposed model, it is possible to obtain accurate representations by reconstructing the full Fourier series for the transformer currents.

Let $v_p = s_1 v_c$ and $v_s = s_2 v_o$ be the voltages across the primary and secondary of the high frequency transformer. To simplify equations, assume that v_c and v_o may be approximated as constant during a single switching period. This scenario would result from sampling the continuous-time state trajectories at multiples of the switching period with a zero-order hold. The transformer current is the solution to the forced differential equation:

$$L_t \dot{i}_t = v_p - v_s - i_t R_t \tag{48}$$

The voltages can be expanded as Fourier series:

$$v_p(\tau) = \sum_{k=1}^{\infty} a_k^p \cos \omega k\tau + b_k^p \sin \omega k\tau \tag{49}$$

$$v_s(\tau) = \sum_{k=1}^{\infty} a_k^s \cos \omega k\tau + b_k^s \sin \omega k\tau \tag{50}$$

The coefficients are known, and equal to the Fourier series coefficients of s_1 and s_2 scaled by v_c and v_o, respectively. The coefficients are:

$$a_k^p = 0 \qquad b_k^p = \begin{cases} \frac{4v_c}{k\pi} & k \text{ odd} \\ 0 & k \text{ even} \end{cases}$$

$$a_k^s = \begin{cases} \frac{-4v_o \sin dk\pi}{k\pi} & k \text{ odd} \\ 0 & k \text{ even} \end{cases} \qquad b_k^s = \begin{cases} \frac{4v_o \cos dk\pi}{k\pi} & k \text{ odd} \\ 0 & k \text{ even} \end{cases}$$

For any given k, the corresponding current solution may be determined using Laplace transforms:

$$i_t(s)(L_t s + R_t) = \frac{(a_k^p - a_k^s)s}{s^2 + (\omega k)^2} + \frac{(b_k^p - b_k^s)\omega k}{s^2 + (\omega k)^2} \tag{51}$$

Alternatively, this may be written as

$$i_t(s) = \left(\frac{1}{L_t s + R_t}\right)\left(\frac{a_k^v s + b_k^v \omega k}{s^2 + (\omega k)^2}\right), \tag{52}$$

where $a_k^v = a_k^p - a_k^s$ and $b_k^v = b_k^p - b_k^s$. The partial fraction decomposition of this equation is:

$$\begin{aligned} i_t(s) = &\frac{1}{L_t}\left(\frac{b_k^v \omega k - a_k^v(\frac{R_t}{L_t})}{(\omega k)^2 + (\frac{R_t}{L_t})^2}\right)\left(\frac{1}{s + (\frac{R_t}{L_t})} - \frac{s}{s^2 + (\omega k)^2}\right) \\ &+ \frac{1}{\omega k L_t}\left[a_k^v + \frac{R_t}{L_t}\left(\frac{b_k^v \omega k - a_k^v(\frac{R_t}{L_t})}{(\omega k)^2 + (\frac{R_t}{L_t})^2}\right)\right]\left(\frac{\omega k}{s^2 + (\omega k)^2}\right) \end{aligned} \tag{53}$$

Taking the inverse Laplace transform yields the time-domain current solution.

$$\begin{aligned} i_t(\tau) = &\frac{1}{L_t}\left(\frac{b_k^v \omega k - a_k^v(\frac{R_t}{L_t})}{(\omega k)^2 + (\frac{R_t}{L_t})^2}\right)\left(e^{\frac{-R_t}{L_t}\tau} - \cos \omega k\tau\right) \\ &+ \frac{1}{\omega k L_t}\left[a_k^v + \frac{R_t}{L_t}\left(\frac{b_k^v \omega k - a_k^v(\frac{R_t}{L_t})}{(\omega k)^2 + (\frac{R_t}{L_t})^2}\right)\right]\sin \omega k\tau \end{aligned} \tag{54}$$

The quantity of interest is the periodic solution, so the decaying exponential term may be discarded. The full current solution is the summation

$$i_t(\tau) = \frac{1}{L_t} \sum_{k=1}^{\infty} a_k^i \cos \omega k\tau + b_k^i \sin \omega k\tau, \tag{55}$$

where a_k^i and b_k^i are the Fourier series coefficients of the transformer current, given by

$$a_k^i = -\left(\frac{b_k^v \omega k - a_k^v (\frac{R_t}{L_t})}{(\omega k)^2 + (\frac{R_t}{L_t})^2} \right) \tag{56}$$

$$b_k^i = \frac{1}{\omega k} \left(a_k^v + \frac{R_t}{L_t} \left(\frac{b_k^v \omega k - a_k^v (\frac{R_t}{L_t})}{(\omega k)^2 + (\frac{R_t}{L_t})^2} \right) \right). \tag{57}$$

The harmonic reconstruction method may be used in steady-state analysis or as a postprocessing method for time-domain simulations. In the latter case, the reconstruction is applied to state trajectories generated through numerical integration of the large-signal model. Since the method is applied offline, the currents for each converter in a given system and each time range of interest may be calculated separately. Moreover, the zero-order-hold approximation allows each switching period to be treated independently. This means that every combination of converter, harmonic number, and switching period in the time range of interest may be considered as an independent, parallel computation.

5. VERIFICATION

Simulations and hardware experiments were used to validate the proposed methods. The objective of the simulation experiments is to show that, in both transient and steady-state conditions, the proposed model and harmonic reconstruction method provide accuracy equivalent to switching simulations with significantly reduced computation time. The objective of the hardware validation is to show the accuracy of the proposed methods with respect to real-world converters.

Table 1. Control and Hardware Parameters for 7-Bus System

Parameter	Value	Parameter	Value
$C_{in}^1, C_{in}^2, C_{in}^3$	200 μF	C_{in}^4, C_{in}^5	40 μF
C_o^1, C_o^2, C_o^3	200 μF	C_o^4, C_o^5	40 μF
f_s^1	40 kHz	k_p^1 / k_i^1	0.01 / 15
f_s^2	60 kHz	k_p^2 / k_i^2	0.01 / 10
f_s^3	75 kHz	k_p^3 / k_i^3	0.01 / 25
f_s^4	100 kHz	k_p^4 / k_i^4	0.001 / 25
f_s^5	90 kHz	k_p^5 / k_i^5	0.005 / 25

5.1. 7-Bus Simulation. One of the key applications of the proposed model is efficient and accurate time-domain simulation. To assess model performance in this capacity, results of system-level simulations performed in PLECS are compared with results obtained through numerical integration of the model equations. Switching simulations are highly accurate but become computationally inefficient as the number of converters in the system increases due to the increased burden of zero-crossing detection.

The system shown in Fig. 2 is considered as a case study. The system is organized as follows. Converter 1 regulates a nominal voltage of 48 V at bus 1. Converter 2 serves bus 4, a subordinate distribution bus, and regulates a nominal voltage of 42 V. Converters 3, 4, and 5 serve bidirectional current source loads. The system may be understood as two subsystems, divided across converter 2. Buses 1, 2, and 3 comprise the 48 V subsystem; buses 4, 5, 6, and 7 comprise the 42 V subsystem. All lines have resistance $R_{ij} = 0.001\ \Omega$ and inductance $L_{ij} = 0.1$ mH. All high-frequency transformers have 1:1 turns ratios, winding resistance $R_t^n = 0.4\ \Omega$, and leakage inductance $L_t^n = 4\ \mu$H. Additional hardware and control parameters are given in Table 1.

Comparisons of switching simulation and model results for a load disturbance transient are shown in Fig. 3 and Fig. 4. The disturbance consists of a step change in the load current of converter 4 at time $t = 0\ s$, from $i_{L0}^4 = 2$ A to $i_{L0}^4 = -2$ A. The load currents

for converters 3 and 5 remain fixed at $i_{L0}^{3} = 4$ A and $i_{L0}^{5} = 2$ A throughout. A selection of bus voltage responses are shown in Fig. 3; line current responses are shown in Fig. 4. The figures show that the model and switching simulation are consistent in both transient and steady-state response. The states not shown in these figures match with similar accuracy. The foremost advantage of using the model for time-domain simulation is execution time. All simulations were performed for a time range of 0.05 s and error tolerance of 10^{-5}. Using a standard explicit solver, the 5-converter switching simulation takes 61.67 s, while integration of the large-signal model completes in 4.11 s. Since the large-signal model is a DAE system, numerical integration using an explicit solver consists of two separate steps: solving dynamic states at the next time step, and then solving the algebraic constraints. Alternatively, the differential and algebraic equations may be solved simultaneously [23]. When this approach is used, numerical integration of the large-signal model completes in 0.466 s.

Despite the accuracy of the dc average states, the transformer currents predicted by the base model are only sinusoidal approximations of the actual transformer current. However, using the harmonic reconstruction method, the actual transformer currents may be calculated with high accuracy as well. A comparison of the transformer current for converter 2 from simulation, from the base model, and from the proposed harmonic reconstruction method is shown in Fig. 5. The reconstruction includes up to the 35th harmonic of the switching frequency. Since only odd harmonics are nonzero, this corresponds to 18 harmonic components.

5.2. Hardware Experiment. The hardware testbed is shown in Fig. 6. The testbed consists of two DAB converters connected in series: the output of converter 1 is connected to the input of converter 2 through a line impedance. The line impedance has both resistive (0.25 Ω) and inductive (100 μH) components. The output of converter 2 is connected to a current source load, which steps from 3 A to 3.5 A during the experiment. Both converters regulate output voltages of 18 V, and operate with switching frequencies of 80 kHz and

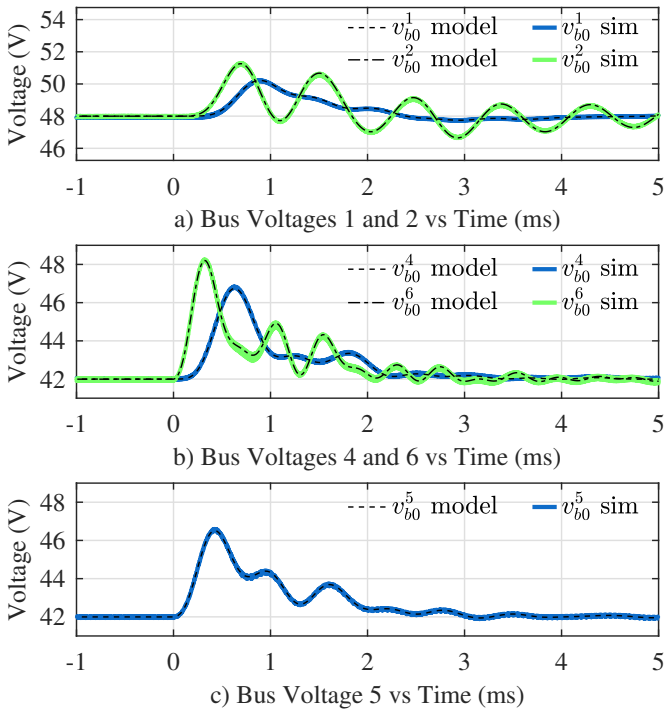

Figure 3. Load disturbance responses of selected system bus voltages. Voltages v_{b0}^1 and v_{b0}^2 are shown in (a), voltages v_{b0}^4 and v_{b0}^6 are shown in (b), and v_{b0}^5 is shown in (c). Voltage v_{b0}^5 is shown separately since it is the only algebraic bus voltage state.

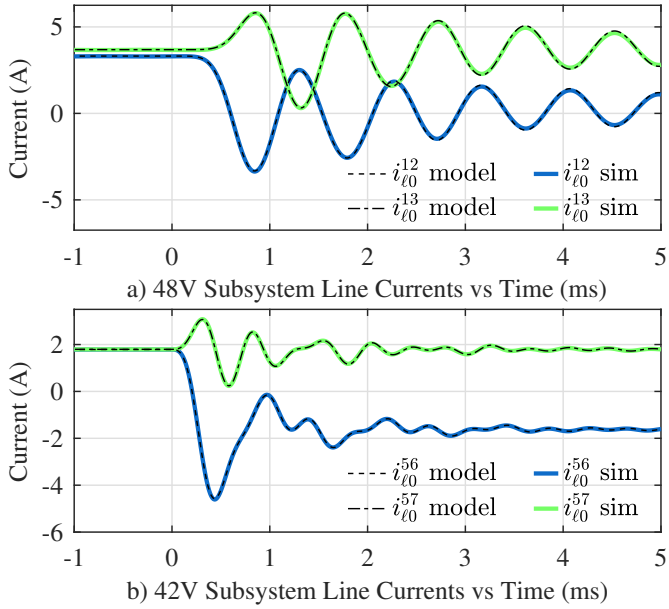

Figure 4. Load disturbance responses of selected system line currents. Line currents $i_{\ell 0}^{12}$ and $i_{\ell 0}^{13}$ are shown in (a), line currents $i_{\ell 0}^{56}$ and $i_{\ell 0}^{57}$ are shown in (b).

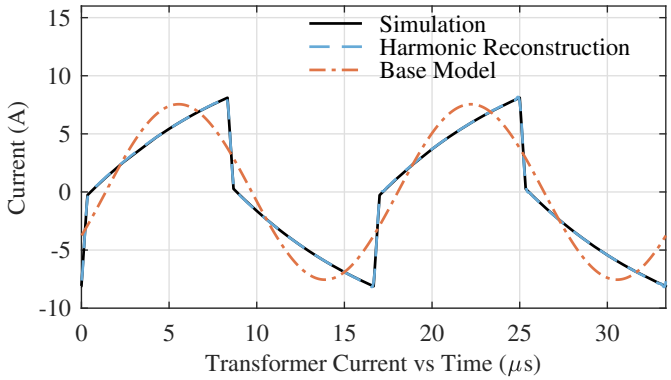

Figure 5. Comparison of converter 2 transformer currents from simulation, results calculated using the proposed harmonic reconstruction method, and first harmonic approximations from the base model.

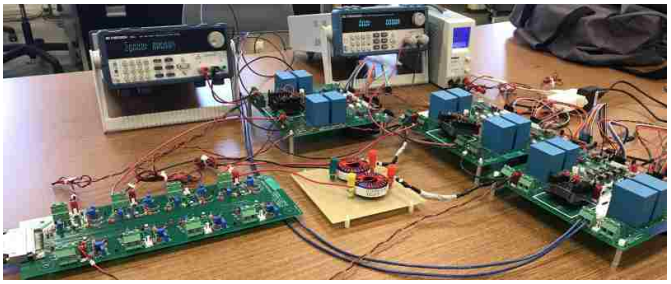

Figure 6. Hardware testbed.

74.074 kHz, respectively. Control systems run independently on two TMS320F28377S digital signal processors (DSPs). Voltages and currents are logged externally during the test; internal state variables are logged through directly through the DSPs.

Comparisons of large-signal model predictions and experimental results are shown in Fig. 7 and Fig. 8. Bus voltage and line current states are shown in Fig. 7, internal integrator states are shown in Fig. 8. The results indicate that the proposed method accurately describes both the transient and steady-state response of the system, despite the difference in switching frequencies between converters. The significance of accurate integrator states is that they allow phase shift values to be determined accurately using (18). This is a distinct advantage over the earlier model in [20], which was affected by large-signal error.

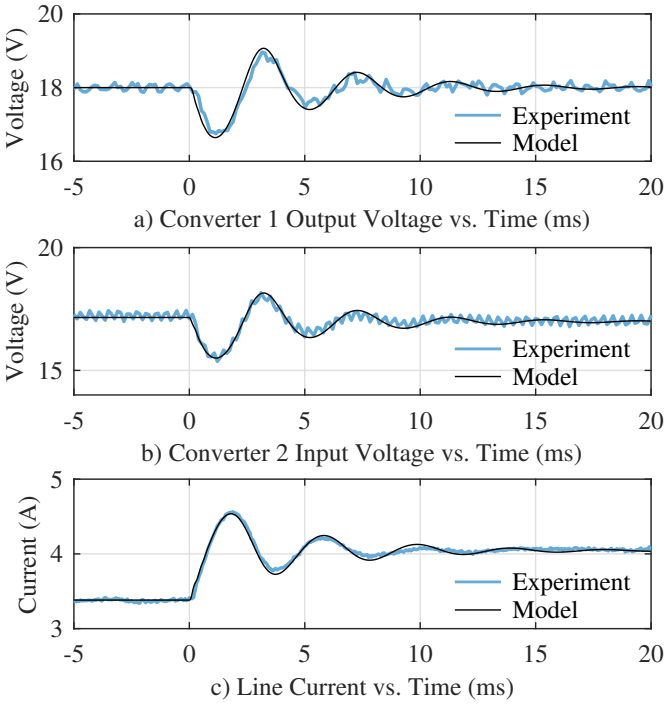

Figure 7. Comparison of hardware measurements and model predictions for bus voltage and line current states.

To verify the functionality of the proposed harmonic reconstruction method, the transformer current of converter 2 is reconstructed and compared to measurements from the experiment. The comparison is shown in Fig. 9. These results demonstrate that the harmonic reconstruction approach accurately describes the real-world behavior of the transformer current.

6. CONCLUSION

This study presents two contributions that support the development of accurate representations of DAB converters in multi-converter systems. First, a modular approach to constructing system-level models is described. The model construction process does not require the specification of a base period, despite the use of GAM to derive the base converter models. This makes it possible to generate models of large systems quickly

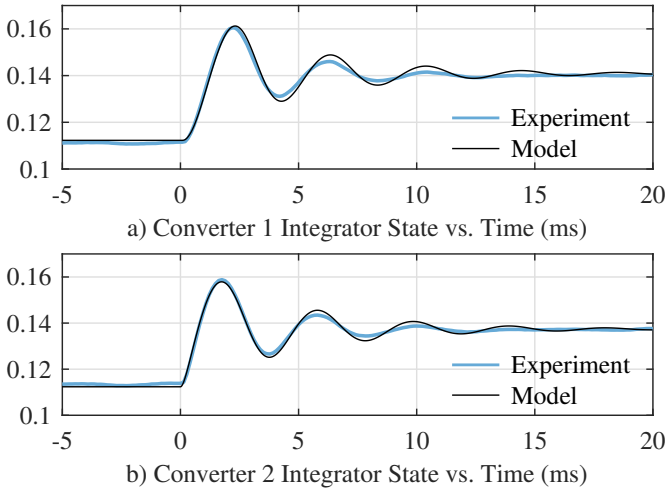

Figure 8. Comparison of hardware measurements and model predictions for controller integrator states.

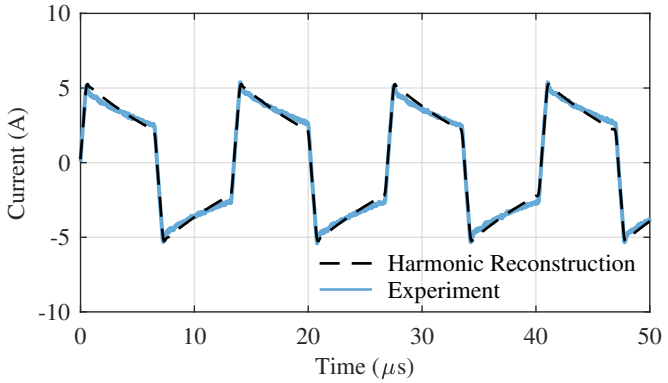

Figure 9. Comparison of converter 2 transformer currents from hardware measurements and harmonic reconstruction.

and easily. The system-level models are fully continuous in time, and provide efficient alternatives to switching simulations for time-domain analysis. Moreover, the models may be linearized for small-signal stability analyses that include the dynamic effects of the high-frequency transformer parameters.

The second contribution of this study is a harmonic reconstruction method that increases the fidelity of high-frequency transformer current representations without increasing model complexity. This reconstruction addresses one of the most important disadvantages of using GAM. The method calculates higher order harmonic components of the transfor-

mer current without including these components as states of the GAM. Furthermore, since the method is applied offline, it does not contribute additional computational complexity when using the system-level model for time-domain simulations.

REFERENCES

[1] R. W. A. A. DeDoncker, D. M. Divan, and M. H. Kheraluwala, "A three-phase soft-switched high-power-density dc/dc converter for high-power applications," *IEEE Trans. Ind. Appl.*, vol. 27, no. 1, pp. 63–73, 1991.

[2] M. N. Kheraluwala, R. W. Gascoigne, D. M. Divan, and E. D. Baumann, "Performance characterization of a high-power dual active bridge dc-to-dc converter," *IEEE Trans. Ind. Appl.*, vol. 28, no. 6, pp. 1294–1301, 1992.

[3] A. Q. Huang, "Medium-voltage solid-state transformer: Technology for a smarter and resilient grid," *IEEE Ind. Electron. Mag.*, vol. 10, no. 3, pp. 29–42, 2016.

[4] X. She, A. Q. Huang, and R. Burgos, "Review of solid-state transformer technologies and their application in power distribution systems," *IEEE J. Emerg. Sel. Topics Power Electron.*, vol. 1, no. 3, pp. 186–198, 2013.

[5] F. Krismer and J. W. Kolar, "Accurate small-signal model for the digital control of an automotive bidirectional dual active bridge," *IEEE Trans. Power Electron.*, vol. 24, no. 12, pp. 2756–2768, 2009.

[6] R. T. Naayagi, A. J. Forsyth, and R. Shuttleworth, "High-power bidirectional dc-dc converter for aerospace applications," *IEEE Trans. Power Electron.*, vol. 27, no. 11, pp. 4366–4379, 2012.

[7] B. Zahedi and L. E. Norum, "Modeling and simulation of all-electric ships with low-voltage dc hybrid power systems," *IEEE Trans. Power Electron.*, vol. 28, no. 10, pp. 4525–4537, 2013.

[8] I. Y. Chung, W. Liu, M. Andrus, K. Schoder, L. Siyu, D. A. Cartes, and M. Steurer, "Integration of a bi-directional dc-dc converter model into a large-scale system simulation of a shipboard mvdc power system," in *2009 IEEE Electric Ship Technologies Symposium*, 2009, pp. 318–325.

[9] G. C. Verghese, M. E. Elbuluk, and J. G. Kassakian, "A general approach to sampled-data modeling for power electronic circuits," *IEEE Trans. Power Electron.*, vol. PE-1, no. 2, pp. 76–89, 1986.

[10] C. Zhao, S. D. Round, and J. W. Kolar, "Full-order averaging modelling of zero-voltage-switching phase-shift bidirectional dc-dc converters," *IET Power Electronics*, vol. 3, no. 3, pp. 400–410, 2010.

[11] L. Shi, W. Lei, Z. Li, J. Huang, Y. Cui, and Y. Wang, "Bilinear discrete-time modeling and stability analysis of the digitally controlled dual active bridge converter," *IEEE Trans. Power Electron.*, vol. 32, no. 11, pp. 8787–8799, 2017.

[12] H. Bai and C. Mi, "Eliminate reactive power and increase system efficiency of isolated bidirectional dual-active-bridge dc-dc converters using novel dual-phase-shift control," *IEEE Trans. Power Electron.*, vol. 23, no. 6, pp. 2905–2914, 2008.

[13] K. Zhang, Z. Shan, and J. Jatskevich, "Large- and small-signal average-value modeling of dual-active-bridge dc-dc converter considering power losses," *IEEE Trans. Power Electron.*, vol. 32, no. 3, pp. 1964–1974, 2017.

[14] F. Zhang, M. M. U. Rehman, R. Zane, and D. Maksimović, "Improved steady-state model of the dual-active-bridge converter," in *2015 IEEE Energy Conversion Congress and Exposition (ECCE)*, 2015, pp. 630–636.

[15] S. R. Sanders, J. M. Noworolski, X. Z. Liu, and G. C. Verghese, "Generalized averaging method for power conversion circuits," *IEEE Trans. Power Electron.*, vol. 6, no. 2, pp. 251–259, 1991.

[16] H. Qin and J. W. Kimball, "Generalized average modeling of dual active bridge dc-dc converter," *IEEE Trans. Power Electron.*, vol. 27, no. 4, pp. 2078–2084, 2012.

[17] J. A. Mueller and J. Kimball, "An improved generalized average model of dc-dc dual active bridge converters," *IEEE Trans. Power Electron.*, vol. PP, no. 99, pp. 1–1, 2018.

[18] A. Emadi, "Modeling and analysis of multiconverter dc power electronic systems using the generalized state-space averaging method," *IEEE Trans. Ind. Electron.*, vol. 51, no. 3, pp. 661–668, 2004.

[19] A. Frances, R. Asensi, O. Garcia, R. Prieto, and J. Uceda, "Modeling electronic power converters in smart dc microgrids - an overview," *IEEE Trans. Smart Grid*, vol. PP, no. 99, pp. 1–1, 2017.

[20] J. A. Mueller and J. W. Kimball, "Generalized average modeling of dc subsystem in solid state transformers," in *2017 IEEE Energy Conversion Congress and Exposition (ECCE)*, October 2017.

[21] S. Bacha, I. Munteanu, and A. I. Bratcu, *Power electronic converters modeling and control: with case studies*, ser. Advanced Textbooks in Control and Signal Processing. London: Springer, 2014.

[22] S. S. Shah and S. Bhattacharya, "Large & small signal modeling of dual active bridge converter using improved first harmonic approximation," in *2017 IEEE Applied Power Electronics Conference and Exposition (APEC)*, 2017, pp. 1175–1182.

[23] M. L. Crow, "Numerical integration," in *Computational Methods for Electric Power Systems*, 3rd ed. Boca Raton, FL: CRC Press, 2016.

III. ACCURATE ENERGY USE ESTIMATION FOR NONINTRUSIVE LOAD MONITORING IN SYSTEMS OF KNOWN DEVICES

Jacob A. Mueller and Jonathan W. Kimball

Department of Electrical & Computer Engineering

Missouri University of Science and Technology

Rolla, Missouri 65409–0050

Email: jam8z4@mst.edu

ABSTRACT

This study presents a method of nonintrusive load monitoring (NILM) for electrical systems consisting of a fixed and known set of devices. This constraint is inherently met by embedded and mobile power systems, and is also commonly satisfied in industrial settings. The proposed NILM method provides time-accurate profiles of device behavior using only probabilistic device models and system-level measurements. The full method consists of model training, construction of a system-level model, and prediction of device-level energy use. Energy use estimations are determined by maximizing the probability of the predicted behavior given the system-level measurements, and are calculated online at each sampling instant. The method is validated using test data from public databases, and its performance is assessed using standard NILM accuracy metrics. The intended application of the proposed method is to support system status assessments and to provide early indications of potential equipment damage through identification of atypical device behavior.

Keywords: nonintrusive load monitoring, load disaggregation, device modeling, hidden Markov models

1. INTRODUCTION

The objective of NILM is to determine individual contributions to combined energy use in an electric system. This breakdown provides a detailed understanding of the active devices in a system from measurements of its composite energy use profile. In a residential setting, this profile can be a set of meter or main-breaker-level measurements. The disaggregated contributions to the total load provide a wealth of knowledge that would otherwise be impractical to attain. This information has a wide variety of applications. For the consumer, it informs decisions on appliance purchases or upgrades [1]. For governments and utilities, disaggregated load profiles may be used to design and assess the efficacy of energy conservation policies, such as conservation voltage reduction or dynamic pricing structures [2, 3].

Many electrical characteristics have been used to identify and model devices [4, 5, 6]. Among these, some of the most successful approaches have used high frequency or transient features. These include harmonics in current waveforms [7] or edge detection methods [8], which identify devices by changes in power when turning on or off. One of the earliest NILM approaches distinguished devices by grouping power changes by location on the P-Q plane [2]. These high frequency characteristics require high sampling rates to accurately record. As a result, models based on these characteristics require large volumes of data. For practical reasons, large storage space requirements and high frequency sampling are undesirable.

Recent research efforts have focused on NILM methods using hidden Markov models (HMMs) to describe electrical systems [9, 10, 11, 12, 13]. Interest in HMMs is motivated by the simplicity with which they accomplish basic modeling functions. Namely, they support an efficient means of parameter estimation (Baum-Welch method) and a straightforward inference algorithm (the Viterbi algorithm) [14]. The general idea behind HMM-based NILM methods is that device behavior can be represented by a latent state variable and an observable output, which is commonly taken as active power or energy. Trained device

models are used to infer the most likely sequence of device states for a given set of measurements. In this capacity, HMMs have been shown to accurately predict device behavior using low frequency ($\leq$1 Hz) measurements. This flexibility with respect to sampling frequency is significant because it allows HMM-based NILM methods to be implemented using existing instrumentation, such as power quality monitors or conventional smartmeter products [12].

Methods of NILM based on HMMs have primarily been studied in the context of residential applications [11, 13, 15]. The main objectives for these applications are to generate cumulative energy usage and time-of-use profiles for each of the devices in the electrical system. This information is not time critical, so offline methods are commonly employed. A fundamental challenge for NILM in residential settings is that the set of devices is continually changing as new devices are acquired and old devices are replaced. This difficulty in handling unmodeled loads has motivated research in unsupervised model training methods, which determine the number and nature of devices in the system and adjust model parameters automatically.

The electrical systems under consideration in this study are assumed to be composed of a fixed and known set of devices. While this assumption limits the applicability of the proposed method in residential contexts, it is commonly met by a variety of pre-designed electrical systems, including factories, data centers, satellites, and electric vehicles of all kinds. Both the challenges and objectives of NILM in these settings are distinct from those of traditional residential applications. The systems of interest serve specific purposes, rather supporting the varied activities of occupants or customers. Because these systems are the result of a premeditated design process, extensive device-level information is known *a priori*. In addition to traditional NILM benefits, such as increased energy efficiency and noninvasive data collection, NILM methods in industrial and vehicular power systems provide a means to assess system health and performance. By detecting and identifying anomalous device behaviors, an industrial NILM system may provide early warnings of impending equipment

failure, preventing damage and reducing downtime. However, conventional HMM-based NILM approaches are unable to support these time-sensitive applications, because their core prediction algorithms operate on full sequences of data. These algorithms may only begin execution after the full length of the sequence has been observed, fundamentally limiting their response times.

The contribution of this study is a NILM procedure for closed electrical systems that provides time-accurate descriptions of device behavior. By eliminating the possibility of unmodeled loads in the system, device behavior in time may be characterized with high precision [16]. The procedure shares some elements with existing NILM methods, such as the supervised training process and use of the Viterbi algorithm (and its variants). However, novel approaches to system-level modeling and energy use prediction are employed. The construction of the system-level model allows independently generated device models to be combined as necessary without requiring aggregate or simultaneous data collection. The energy prediction method maximizes the probability of the predicted device outputs at each sampling instant, and contributes only minimally to overall algorithm complexity. While the proposed method shares the same scalability issues as other HMM-based NILM approaches, recent sparsity exploitation methods may be utilized to mitigate the effects of these issues without degradation of accuracy. The following sections include a discussion of the proposed method and a verification of the method's functionality using a test system of data from public NILM databases.

2. BACKGROUND

An HMM is a tool for describing time series data. Measured data are assumed to be generated by a discrete stochastic process, which itself cannot be directly observed. The observed outputs are assumed to follow a probability distribution conditional on the

current state. Both the probability of the hidden process transitioning to a new state and the probability of a given output being observed satisfy a Markov property: they are conditional only on the current state and are independent of states and outputs at all other times [17].

2.1. Device Modeling. Consider a process being observed at sampling intervals of length T_S. The discrete sample indices are $t \in \{1, \cdots, T\}$. The resulting sequence of observations is

$$O = \{O_1, \cdots, O_T\}. \tag{1}$$

Each O_t may be real-valued or chosen from a discrete set of symbols. The sequence of process states that is assumed to generate these observations is

$$Q = \{Q_1, \cdots, Q_T\}, \quad Q_t \in S = \{S_1, \cdots, S_N\}, \tag{2}$$

where S is the set of N possible states the process may occupy. The HMM itself consists of three components. The transition matrix, A, contains the probabilities of transitioning to another state given the current state. $A \in \mathbb{R}^{N \times N}$ with elements A_{ij} where

$$A_{ij} = P[Q_{t+1} = S_j | Q_t = S_i]. \tag{3}$$

The observation probabilities for each state are defined by ϕ, where

$$\phi_i(O_t) = P[O_t | Q_t = S_i]. \tag{4}$$

In (4), $\phi_i(O_t)$ is a density function and O_t may take on any real number. When observations are discrete-valued, $O_t \in \{v_1, \cdots, v_M\}$ where v_1 through v_M are discrete output symbols. In this case, observation probabilities are discrete in nature, and are contained in a matrix $\Phi \in \mathbb{R}^{N \times M}$ with elements Φ_{ij}, where

$$\Phi_{ij} = P[O_t = v_j | Q_t = S_i]. \tag{5}$$

Finally, initial state occupation probabilities are contained in vector $\pi \in \mathbb{R}^N$, where

$$\pi_i = P[Q_1 = S_i]. \tag{6}$$

The structure of a hidden Markov model for a 3-state device is shown in Fig. 1, along with its associated parameters.

In modeling a device with an HMM, the first step is to define the states and observations. In this study, HMM states represent different operational modes of the device. Each mode is associated with a subset of elements within the device whose power consumption is approximately Gaussian distributed. States are integer valued, so $S_i = i$ and Q is a sequence of integers in range $[1, N]$. Observations are defined as active power consumption. Devices are assumed to be loads, so observations are nonnegative and additive for multiple devices. Since the sampling period is fixed, the energy used by the device since the last sampling instant is the observation scaled by the sampling time. This approximates the power consumption in time using a zero order hold for the sampled measurements. Because of this relationship, the terms power and energy are used somewhat interchangeably when referring to a single sample.

The assumption of Gaussian distributed observations is common in HMM-based NILM [10, 9, 15, 18, 11, 19]. The power measurement of a given device state is subject to a large number of uncertainties including component tolerances, thermal noise, variations

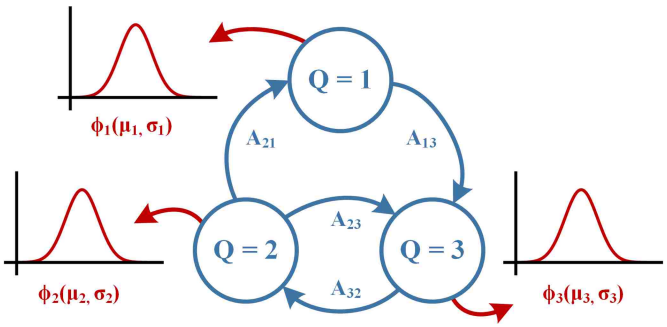

Figure 1. Example of a hidden Markov model structure for a 3-state device.

in grid voltage, and other physical factors. Provided that the sources of uncertainty are independent with finite variance, the central limit theorem states that the observations of the given device state converge in distribution to the Gaussian distribution. In practice, a simpler justification is provided by visual inspection. In Fig. 2, normalized histograms are shown for dryer, stove, and dishwasher devices. Each bar of the histogram represents a bin of 10W, while the y-axis indicates the relative frequency of observations in the corresponding bin. The data in these plots were collected over a period of 10 days with sampling period of 5 seconds.

While the assumption of Gaussian observation distributions is well-founded for most devices, there are some exceptions. Devices with continuously variable power consumption use any amount of power in a limited range with equal probability, and are best represented by a uniform observation distribution. An example of this kind of device is a light with a dimmer switch. Fortuitously, these types of devices are relatively rare. When devices require a continuous range of power utilization, a more common strategy is to transition actively between high and low power states, producing an intermediate power use on average.

Additional modeling assumptions are inherited from the HMM framework. Namely, devices are assumed to be independent and their transition probabilities are assumed to be conditional only on the current device state. A direct consequence of this latter assumption is that the dwell times, or times spent between transitions, are exponentially distributed. These assumptions clearly represent idealized device behavior. However, the cost of refining the models to include more realistic descriptions is high. In [9], models that include device dependencies and more realistic dwell times were proposed. Although these features increase model accuracy, their training and inference algorithms are computationally intractable. For the purposes of this study, the benefit of eliminating errors introduced by simplified modeling assumptions is not worth the accompanying loss of tractability.

2.2. Model Training. Because the composition of the system is assumed to be known *a priori*, a supervised training approach is sufficient. In supervised training methods, device models are trained from previously recorded observation data. The devices contained in the system are expected to behave in a consistent way. Consequently, any unexpected observations may be interpreted as changes in device status due to damage or malfunction. In this way, the proposed method provides a characterization of the health of the network based on how closely the observations match expectations. This characterization can be used to detect anomalous behaviors resulting from damaged equipment or system faults.

The training process begins with collections of raw device device power measurements. Since training occurs offline, and these observation sequences are gathered for the specific purpose of device training, it can be assumed that they are recorded with high enough resolution to be considered continuous. State sequences for this preliminary data

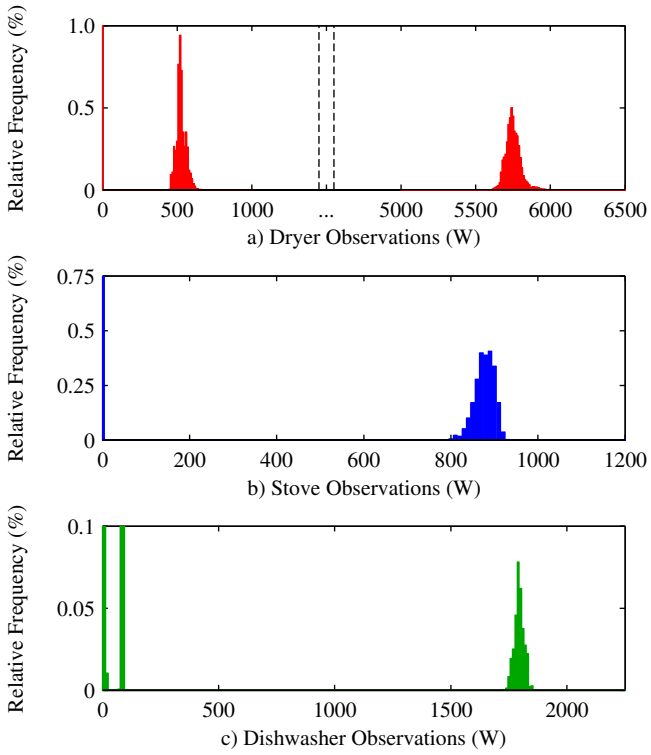

Figure 2. Normalized histogram of observations from dryer (a), stove (b), and dishwasher (c) devices over a period of 10 days. Each bar of the histogram corresponds to a bin of 10W.

are chosen according to the selected state labeling scheme. The preliminary data is then in the form of a state sequence Q and a raw sequence of observations, O. Elements of the transition matrix and the initial state vector are determined from Q as maximum likelihood estimates (MLE):

$$A_{ij} = \frac{\sum_{t=1}^{T-1}[I(Q_t = i) \cdot I(Q_{t+1} = j)]}{\sum_{t=1}^{T-1} I(Q_t = i)} \tag{7}$$

$$\pi_i = \frac{1}{T-1} \sum_{t=1}^{T-1} I(Q_t = i) \tag{8}$$

where $I(\cdot)$ is the indicator function.

Observation distributions for each state are trained from the observation sequence. The procedure depends on the state labeling scheme. For the selected state definition approach, observation probabilities are Gaussian distributed. Each state of the device has corresponding mean and variance parameters, μ and σ^2. These are taken as the sample means and sample variances of the raw power measurements:

$$\mu_i = \frac{\sum_{t=1}^{T}[O_t \cdot I(Q_t = i)]}{\sum_{t=1}^{T} I(Q_t = i)} \tag{9}$$

$$\sigma_i^2 = \frac{\sum_{t=1}^{T}[(O_t - \mu_i)^2 \cdot I(Q_t = i)]}{\sum_{t=1}^{T} I(Q_t = i)} \tag{10}$$

Again $I(\cdot)$ is the indicator function, and is used to attribute parameters to the correct states while setting others to 0. The observation probabilities are now in the form of N Gaussian distributions, or $\phi_i \sim \mathcal{N}(\mu_i, \sigma_i^2)$.

2.3. Scalability and State Inference. Despite the accuracy and flexibility of HMM-based NILM approaches, their underlying algorithms are subject to severe scalability issues. The simplest device model, representing a binary on/off device, has two states. If an HMM is used to represent N of these devices, the total number of states in the system is 2^N. This

exponential scaling in N is a problem on its own, but the more critical limiting influence is the Viterbi algorithm, which has time complexity $O(N^2T)$, where T is the length of the sequence of observations.

The proposed strategies for handling this fundamental limitation have split the field of HMM-based NILM into two groups. The first approach is to use generalizations of HMMs, such as factorial hidden Markov models (FHMMs), which describe multiple devices individually in a distributed state representation [20]. FHMMs have been successfully applied to NILM [19, 9, 18, 21]. A variety of modified FHMM structures are proposed and compared in [9]. The drawback to all of these methods is that exact inference is computationally intractable, and approximate methods must be used. In [15], an approximate inference method motivated by the NILM problem was proposed. The second group of approaches uses the basic HMM structure and relies on the sparsity of matrices that comprise the system-level model to reduce the complexity of the problem. This approach relies on alternative formulations of the Viterbi algorithm, such as those proposed in [22, 23]. One such method, the sparse Viterbi algorithm, was applied in [13] to a NILM system consisting of over 10^9 states with high accuracy and dramatic reductions in execution time. This greedy variant of the Viterbi algorithm maximizes the probability of each individual state sequence transition, allowing online operation.

The NILM procedure proposed in this study uses the traditional HMM structure and is compatible with any state inference method intended for basic HMMs. Since the target applications of this method favor online disaggregation, the sparse Viterbi algorithm is given particular consideration. In preparing the experimental results for this study, both the standard Viterbi algorithm and the sparse Viterbi algorithm were used. For the sake of completeness, a general review of the two algorithms is repeated in this section. More detailed information is available in the accompanying references.

The Viterbi algorithm is well known and is a common element of HMM-based NILM procedures. In the standard Viterbi algorithm, the inferred state sequence $\hat{Q}$ is the sequence of states that maximizes the total probability of the complete sequence of observations. This is done in two steps. First, the algorithm iterates forward in time through the observation sequence. For each state S_j, the algorithm calculates the best possible sequence of previous states ending in state S_j. The probability $\delta_t(j)$ of the best state sequence ending in S_j is calculated recursively. The value of $\delta_t(j)$ depends on a value $\delta_{t-1}(i)$ of state S_i during the previous instant and the probability of transition from state S_i to state S_j. The state S_i that maximizes $\delta_t(j)$ is saved as $\psi_t(j)$.

$$\delta_0(j) = \pi_j \phi_j(O_0) \tag{11}$$

$$\delta_t(j) = \max_{i \in S} \left(\delta_{t-1}(i) A_{ij}\right) \phi_j(O_t) \tag{12}$$

$$\psi_t(j) = \operatorname*{argmax}_{i \in S} \left(\delta_{t-1}(i) A_{ij}\right) \tag{13}$$

Since the observation probabilities of the system-level model are discrete, the $\phi_j(O_t)$ terms in these equations will simply index the appropriate elements of the observation matrix.

The forward step of the algorithm continues until $t = T$. The second step iterates backward in time, constructing the predicted sequence of states from the values of ψ_t. Beginning with $\hat{Q}_T = \max(\delta_T)$, the predicted states are

$$\hat{Q}_t = \psi_{t+1}(\hat{Q}_{t+1}). \tag{14}$$

The backward step continues until $t = 0$.

The sparse Viterbi algorithm was proposed in [23], and was applied to a large-scale NILM problem in [13]. Two factors contribute to the reduction in execution time provided by the sparse Viterbi algorithm. First, the model transition and observation parameters are stored and referenced using sparse matrix storage techniques. Secondly, the algorithm

is designed to find the most probable state transition at each instant, rather than the most probable full sequence of states. To begin each iteration, the algorithm calculates a state occupation probability for the previous time instant. For each state, $\rho_{t-1}(j)$ is the probability of state S_j at the previous time instant given the previous observation. Using these values, the algorithm then finds the probabilities of the current state, $\rho_t(j)$, given the possible past states, transition probabilities, and current observation data. The state that maximizes $\rho_t(j)$ is the predicted state.

$$\rho_{t-1}(j) = \pi_j \phi_j(O_{t-1}) \tag{15}$$

$$\rho_t(j) = \max_{i \in S} \rho_{t-1}(i) A_{ij} \phi_j(O_t) \tag{16}$$

$$\hat{Q}_t = \operatorname*{argmax}_{j \in S} \big(\rho_t(j)\big) \tag{17}$$

The sparse Viterbi algorithm provides a state prediction for each observation sample, and requires no backtracking step. By using sparse matrix format for the transition matrix, observation matrix, and state occupation vectors, the algorithm is able to automatically ignore any calculations involving zero-probability terms.

The standard Viterbi algorithm executes over a fixed-length sequence of past observations, so a full sequence must be collected before the algorithm can begin execution. This limits the algorithm's ability to provide timely feedback. As a greedy variant, the sparse Viterbi algorithm calculates the most likely state transition for each individual sample. This enables the algorithm–and the proposed energy prediction method–to provide outputs on a sample-by-sample basis, significantly reducing response time.

In addition to online operation, the sparse Viterbi algorithm provides modest scalability benefits. The algorithm effectively ignores transition and observation elements with zero probability, decreasing the computational complexity of the state inference process. The scalability increases offered by this algorithm are maximized when the composite system transition and observation matrices are sparse. The sparsity of the observation matrix

is controlled by parameter B_S and a minimum probability threshold, ϵ. The sparsity of the transition matrix varies with the type of devices included in the model. A general approach to increasing the sparsity of the transition matrix is not available in the literature, but system-specific solutions may be achieved by relaxing the assumption of device independence. For example, in [13] aggregate observation data was used to train device dependence into the system-level model. Further research is needed to identify general methods of reducing the complexity of the state disaggregation process.

3. METHODOLOGY

In this section, an innovative model combination and state disaggregation method is described, and a novel, highly-accurate energy reconstruction algorithm is applied to find instantaneous power consumption of each device.

3.1. Model Combination. For a given electrical network, the models of system devices can be combined into a single composite model that represents the behavior of the system as a whole. The composite model is the base of the NILM implementation. Combining the individual HMMs involves combining the transition matrices and the observation distributions.

3.1.1. Transition Matrix. The combination of transition matrices is accomplished using the Kronecker product. Devices are combined sequentially, so the order in which they are incorporated into the model is important. To distinguish the composite transition matrix from those of the individual models, composite matrices are referred to by A, while the transition matrices of the devices will be identified with a superscript. The same scheme will apply for the observation distributions, state sequences, and observation sequences, and will be used for the remainder of the paper. For a set of K devices, the transition matrix of the composite system after incorporating the K^{th} device is:

$$A = \left((A^{(1)} \otimes A^{(2)}) \cdots \otimes A^{(K)}\right) \tag{18}$$

where $\otimes$ denotes the Kronecker product. Models are combined upwards from the first device, and the order in which they are incorporated, k, is used to identify their parameters in the disaggregation process. Alternatively, the composite matrix may be defined recursively as $A = A \otimes A^{(k)}$, $k = 1, 2, \ldots, K$, where A is initialized as $A = 1$. The initial probability vector of the combined system is calculated using (18) as well, the only difference being that the result will remain a vector rather than a matrix.

To illustrate the combination process, consider a simplified example system of two devices. Transition diagrams are shown for the devices in Fig. 3, with self-transitions excluded for clarity. Device 1 consists of two states and device 2 consists of three states. The directions on the edges of the graph indicate the possible transition directions. For example, device 2 may transition freely between states 1 and 3, but may not transition to state 2 from state 3. This is reflected in the transition matrix by a 0 element in column 3, row 2. Possible transition matrices for these devices are

$$A^{(1)} = \begin{bmatrix} 0.9 & 0.1 \\ 0.2 & 0.8 \end{bmatrix}, \quad A^{(2)} = \begin{bmatrix} 0.8 & 0.1 & 0.1 \\ 0 & 0.4 & 0.6 \\ 0.5 & 0 & 0.5 \end{bmatrix}.$$

These probabilities are simplified for the sake of illustration. When the two devices are represented as a system, all possible transitions must be represented. This is shown in Fig. 4. The system-level state, Q, is encircled in the nodes of the graph while the

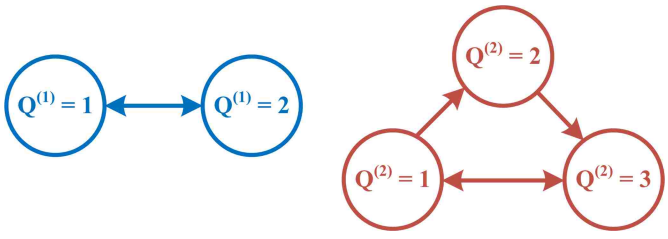

Figure 3. Directed graph representation of two example devices and their potential transitions.

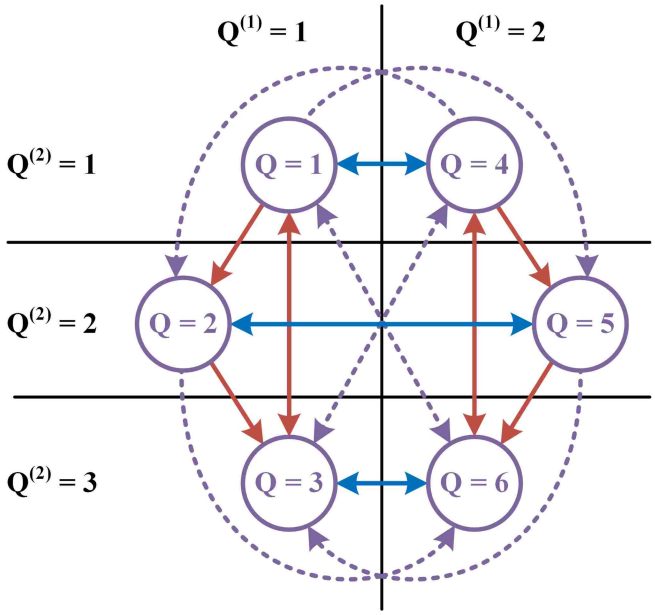

Figure 4. Directed graph representation of a two-device example system. Dotted lines indicate transitions in which both devices change state simultaneously.

corresponding device-level states are shown in the margins. The edges again indicate potential transitions. Since device 2 is unable to transition from state 3 to state 2 at the device level, the combined system is likewise unable to transition from states 3 or 6 to states 2 or 5. This restriction is again represented in the transition matrix.

$$A^{(1)} \otimes A^{(2)} = \begin{bmatrix} 0.72 & 0.09 & 0.09 & 0.08 & 0.01 & 0.01 \\ 0 & 0.36 & 0.54 & 0 & 0.04 & 0.06 \\ 0.45 & 0 & 0.45 & 0.05 & 0 & 0.05 \\ 0.16 & 0.02 & 0.02 & 0.64 & 0.08 & 0.08 \\ 0 & 0.08 & 0.12 & 0 & 0.32 & 0.48 \\ 0.1 & 0 & 0.1 & 0.4 & 0 & 0.4 \end{bmatrix}$$

3.1.2. Observation Matrix. To simplify the combination of observation probabilities, the individual devices' observation distributions are converted into discrete probability mass functions, such that they may be described in matrix form. To convert the continuous

distributions into a discrete representation, an appropriate bin size, B_S, is selected for the desired application. The bins form an ordered partition of the range of possible power use, indexed from 1 to M. The largest bin index, M, is determined by the capacity of the line and is therefore bounded by physical constraints. In this way, B_S determines the size of the individual device observation matrices and, by extension, the size of the composite observation matrix. In reference to the sensor apparatus used to collect the aggregate observations during the NILM system deployment, B_S represents an important design parameter connecting the minimum sensor resolution to model size and complexity.

The discrete elements of the observation matrix $\Phi^{(k)}$ for device k are then calculated by integrating the observation density functions over the set of bins.

$$\Phi_{ij}^{(k)} = \int_{(j-1)B_S}^{(j)B_S} \phi_i^{(k)}(O_t) dO_t, \quad j = 1, 2, \cdots, M \tag{19}$$

Integrating over the bins ensures that no bin contains a zero observation probability, which could result from incomplete training data if the observation matrix were taken directly from the sequence of binned observations. However, for sparsity exploitation methods, it is desirable to have as few nonzero elements as possible. Elements with very low probability may be neglected by setting a minimum probability threshold, ϵ, such that observation matrix elements are fixed to 0 if their calculated values are less than ϵ. For this study, $\epsilon = 10^{-9}$ was used. Once these low-probability elements are eliminated, the rows of $\Phi^{(k)}$ are normalized such that they form valid probability mass functions, i.e. each row sums to 1.

The observation matrix for the combined system is produced by taking the Kronecker product of the individual matrices and summing columns that correspond to equal total observations. This sum results from the fact that power contributions from each device

are additive. When B_S is small, the observation matrices may be very large in size, and calculation of the Kronecker product will be slow. For this case, it is easier to find the combined observation matrix by column.

$$\boldsymbol{\Phi} = \left[\boldsymbol{\Phi}_{*,1} \;\middle|\; \boldsymbol{\Phi}_{*,2} \;\middle|\; \cdots \;\middle|\; \boldsymbol{\Phi}_{*,m} \right] \tag{20}$$

$$\boldsymbol{\Phi}_{*,c} = \sum_{a=1}^{c-1} \sum_{b=1}^{c-1} \left(I(a+b-1=c) \left(\boldsymbol{\Phi}_{*,a} \otimes \boldsymbol{\Phi}^{(k)}_{*,b} \right) \right) \tag{21}$$

This process is repeated for each k, in the same order in which the devices' transition matrices were combined. Once an individual device's observation matrix has been included in the combined system model, it may be discarded. Only the parameters of the continuous observation distributions need to be retained, so it is not necessary to store full matrices for each device.

Returning to the example system, let the bin size be $B_S = 5\text{W}$ and suppose the devices may only use 0W, 5W, or 10W at any given instant. In this way, an observation $O^{(1)} = 1$ corresponds to device 1 using 0W, $O^{(2)} = 2$ to device 2 using 5W, and so on. The observations occur according to the following probabilities:

$$\boldsymbol{\Phi}^{(1)} = \begin{bmatrix} 1 & 0 & 0 \\ 0 & 0.2 & 0.8 \end{bmatrix}, \quad \boldsymbol{\Phi}^{(2)} = \begin{bmatrix} 1 & 0 & 0 \\ 0 & 0.9 & 0.1 \\ 0 & 0.3 & 0.7 \end{bmatrix}.$$

Again, these values are used to simplify the demonstration of the combination process. Normally, the discrete elements would result from the integration of continuous observation distributions as shown in (19). The system-level observation matrix for these devices is

$$\Phi = \begin{bmatrix} 1 & 0 & 0 & 0 & 0 \\ 0 & 0.9 & 0.1 & 0 & 0 \\ 0 & 0.3 & 0.7 & 0 & 0 \\ 0 & 0.2 & 0.8 & 0 & 0 \\ 0 & 0 & 0.18 & 0.74 & 0.08 \\ 0 & 0 & 0.06 & 0.38 & 0.56 \end{bmatrix}.$$

Element Φ_{54} is the conditional probability that the system consumes 15W ($O = 4$) given that the system state is $Q = 5$. From Fig. 4, system state 5 corresponds to $Q^{(1)} = 2$ and $Q^{(2)} = 2$. Given these states, system power consumption of 15W may occur either when $O^{(1)} = 2$ and $O^{(2)} = 3$, or when $O^{(1)} = 3$ and $O^{(2)} = 2$. The value of Φ_{54} is then:

$$\begin{aligned} \Phi_{54} &= P\left[O = 4 | Q = 5\right] \\ &= P\left[O^{(1)} = 2 \middle| Q^{(1)} = 2\right] P\left[O^{(2)} = 3 \middle| Q^{(2)} = 2\right] \\ &\quad + P\left[O^{(1)} = 3 \middle| Q^{(1)} = 2\right] P\left[O^{(2)} = 2 \middle| Q^{(2)} = 2\right] \\ &= \Phi_{23}^{(1)} \Phi_{22}^{(2)} + \Phi_{22}^{(1)} \Phi_{23}^{(2)} \\ &= (0.8)(0.9) + (0.2)(0.1) = 0.74 \end{aligned}$$

The calculation of this element illustrates how the system-level observation probabilities are related to the probabilities of observations at the device level. Equation (21) applies this same operation to column vectors from the device matrices and produces the columns of system-level observation matrix.

The training and model combination process need only occur once, offline. The following sections discuss the online operations of the NILM system, including state disaggregation and energy use prediction.

3.2. State Disaggregation. The system model represents K devices and consists of transition matrix A and observation matrix Φ. A sequence of observations O is measured for the full system. From the assumption of a closed system of known devices, it follows that

$$O = \sum_{k=1}^{K} O^{(k)}, \tag{22}$$

where $O^{(k)}$ is the unknown energy contribution of device k. The objective of the NILM system is to find the best possible estimate of these contributions. The first step towards this goal is to determine the composite sequence of states $\hat{Q}$ that is most likely to result in the composite observation sequence O. The inferred state sequence $\hat{Q}$ is calculated from the composite matrices A and Φ, and represents the most likely behavior of all devices considered as a single system. Since the system model is itself an HMM, this may be accomplished using the Viterbi algorithm [24, 14] or a variant of the Viterbi algorithm, as discussed in Section 2.3.

Once the composite sequence $\hat{Q}$ has been calculated, the next task is to determine the most likely state sequence for each individual device. Because of the use of the Kronecker product in constructing the composite model, the device states are interleaved in the system model. The correspondence of individual device states to composite model state is dependent on the order in which their individual models were included in the composite model. From the set of K devices, let N_k be the number of states in the k^{th} device, numbered in order of incorporation in (18). The generalized disaggregation algorithm is then

$$\hat{Q}_t^{(k)} = \mathrm{mod}\left(\mathrm{ceil}\left(\frac{\hat{Q}_t}{\prod_{j=k+1}^{K} N_j}\right) - 1, N_k\right) + 1, \tag{23}$$

where $\hat{Q}_t^{(k)}$ is the Viterbi path for the k^{th} device at instant t, and mod and ceil are the modulo and ceiling functions, respectively.

For device K, the last included in the composite model, the form of (23) reduces to

$$\hat{Q}_t^{(K)} = \text{mod}\left(\hat{Q}_t - 1, N_K\right) + 1. \tag{24}$$

The graph in Fig. 4 provides a visual representation of equations (23) and (24) for the two-device example system. It is clear from the graph that system state $Q = 5$ corresponds to device states $Q^{(1)} = 2$ and $Q^{(2)} = 2$. Equivalently, $\hat{Q} = 5$ corresponds to $\hat{Q}^{(1)} = 2$ and $\hat{Q}^{(2)} = 2$ at any given instant. The disaggregation equations produce the same results. Equation (23) must be used to calculate $\hat{Q}^{(1)}$, while the reduced form in (24) may be used to calculate $\hat{Q}^{(2)}$. For this system, $K = 2$, $N_1 = 2$, and $N_2 = 3$.

$$\hat{Q}^{(1)} = \text{mod}\left(\text{ceil}\left(\frac{5}{3}\right) - 1, 2\right) + 1 = 2$$

$$\hat{Q}^{(2)} = \text{mod}\left(5 - 1, 2\right) + 1 = 2$$

3.3. Prediction of Energy Use. Once the estimated state sequences for the individual devices have been found, it remains to predict the energy use of each device. The simplest approach to this prediction is to use the best possible constant estimator. This is given by the expected value of the observation, conditional on the current state.

$$\hat{O}_t^{(k)} = E\left[O_t^{(k)} \middle| Q_t^{(k)} = j\right] = \mu_j^{(k)} \tag{25}$$

The total energy use predicted for device n is then

$$\hat{W}^{(k)} = T_S \sum_{t=1}^{T} \hat{O}_t^{(k)}. \tag{26}$$

This conventional method is useful in estimating cumulative energy use over a period of time, but provides only a rough approximation of actual device behavior. The number of possible observation predictions is limited to the number of model states, and the predictions of observations in time are constant when the state is not changing.

When the set of devices contained in the system is known and unchanging, a more detailed estimate of the energy contributions from each device may be achieved by breaking down the composite energy use according to the devices' conditional observation distributions. The calculation of these predictions may be framed as a constrained optimization problem, maximizing the total probability of the observations while constraining their sum to equal the measured aggregate observation.

Let $\hat{O}$ be a K-vector of observation predictions for the K system devices. Because the devices are assumed to operate independently, the probability of $\hat{O}$ given the disaggregated state sequence is determined by

$$P[\hat{O}] = \prod_{k=1}^{K} P\left[\hat{O}^{(k)} \middle| \hat{Q}^{(k)} = j\right] = \prod_{k=1}^{K} \phi_j^{(k)}\left(\hat{O}^{(k)}\right). \tag{27}$$

To simplify notation, time indices t have been dropped in (27), and will be omitted for the remainder of this section. Working in logspace, the product term in (27) becomes a summation of terms, but the locations of critical points remain the same. The objective function f is defined as

$$f(\hat{O}) = \ln\left(P[\hat{O}]\right) = \sum_{k=1}^{K} \ln\left(\phi_j^{(k)}\left(\hat{O}^{(k)}\right)\right). \tag{28}$$

The equality constraint, g, is given by the assumption of known system composition and additive observations.

$$g(\hat{O}) = \sum_{k=1}^{K} \hat{O}^{(k)} - O = 0 \tag{29}$$

Using Lagrange multipliers, $\nabla f = \lambda \nabla g$. The k^{th} summation term of (28) depends only on the k^{th} element of $\hat{O}$. For $\hat{Q}^{(i)} = j$, the partial derivative is then

$$\frac{\partial f(\hat{O})}{\partial \hat{O}^{(k)}} = \frac{\partial}{\partial \hat{O}^{(k)}} \ln\left(\phi_j^{(k)}(\hat{O}^{(k)})\right) = \frac{\left(\mu_j^{(k)} - \hat{O}^{(k)}\right)}{\left(\sigma_j^{(k)}\right)^2}. \tag{30}$$

The convenient linear form of this equation results from the assumption of Gaussian observation distributions. The k^{th} term of $\lambda \nabla g$ is

$$\lambda \frac{\partial g(\hat{O})}{\partial \hat{O}^{(k)}} = \lambda. \tag{31}$$

Equating the derivatives in (30) and (31),

$$\frac{\left(\mu_j^{(k)} - \hat{O}^{(k)}\right)}{\left(\sigma_j^{(k)}\right)^2} = \lambda. \tag{32}$$

By rearranging this equation, each $\hat{O}^{(k)}$ may be expressed in terms of λ and mean and variance parameters, which are known.

$$\hat{O}^{(k)} = \mu_j^{(k)} - \lambda \left(\sigma_j^{(k)}\right)^2 \tag{33}$$

Substituting these terms into (29) yields an expression for λ in terms of the aggregate observation and the sums of the means and variances of the appropriate device states.

$$\lambda = \frac{\left(\sum_{k=1}^{K} \mu_{\hat{Q}^{(k)}}^{(k)}\right) - O}{\sum_{k=1}^{K} \left(\sigma_{\hat{Q}^{(k)}}^{(k)}\right)^2} \tag{34}$$

Finally, the individual observation predictions are then calculated by substituting λ back into (33) for each device.

The final equations (33) and (34) are used to predict the device-level observations at each time sample. This adds little in terms of computational complexity, as the summations in (34) contain K terms, and only change when disaggregated state changes.

3.4. Discussion. In the context of HMM-based NILM procedures, the proposed method features novel approaches to system-level modeling and energy use prediction. The basic HMM framework is used at both the device and system level, allowing simple and well-known methods to be used for training and state inference. The combination process is modular in that devices may be modeled individually and used later to build system-level models. A conceptually similar model combination process was employed for two devices in [10], but was presented without the necessary mathematical framework, and without the ability to break system-level states into individual device states. Methods in other studies, such as [13], require system-specific training data. Beyond knowledge of the devices contained in a system, the proposed method requires no system-specific information. That is, the system-level model can be constructed without composite or simultaneous submetered data collection.

In the process of combining device models, continuous observation distribution parameters are converted into discrete probabilities. This allows sparsity exploitation methods, i.e. the sparse Viterbi algorithm, to be employed in the state inference stage. However, the continuous parameters are preserved, and are used after the state has been disaggregated to provide more accurate energy use predictions.

The most important element of the proposed method is the energy prediction process. Other HMM-based NILM studies typically stop at state disaggregation, and provide energy predictions as constant, one-to-one mappings between state and observation. This limitation is dictated by application context; almost all other methods are intended for residential systems in which unmodeled loads are likely present. The uncertainty introduced by unknown devices prevents more refined predictions. For the applications of the proposed

method, it is assumed that all loads are known, and the equality constraint in (29) may safely be applied. The key benefit of this arrangement is that transient and high-variance features in device behavior are accurately recognized.

Separating energy prediction from state inference also allows an additional degree of freedom in system time scale. For existing HMM-based NILM methods, the time scale of the state disaggregation and energy use prediction are the same, and are set by the observation sequence sampling time. Unless the predicted state changes, the observation prediction cannot change. In the proposed method, it is possible to execute the more computationally expensive state prediction on a slower time scale and allow the energy use prediction to iterate more quickly. This functionality provides additional time resolution to the observation predictions at a low computational cost.

Table 1. Device-Level Accuracy Results from Disaggregation Tests

Standard Viterbi Algorithm				
Device	**States**	**State Accuracy**	**Estimation Acc. Proposed Method**	**Estimation Acc. Expect. Method**
Stove	2	0.9553	0.9644	0.9608
Dryer	3	0.9834	0.9953	0.9925
Dishwasher	3	0.5081	0.9674	0.9651
Microwave	2	0.7221	0.8743	0.8732
Refrigerator	3	0.8754	0.9185	0.9080
LCD TV	2	0.9011	0.9088	0.8943
Sparse Viterbi Algorithm				
Stove	2	0.9511	0.9596	0.9561
Dryer	3	0.9782	0.9951	0.9919
Dishwasher	3	0.5007	0.9107	0.9080
Microwave	2	0.7953	0.7348	0.7323
Refrigerator	3	0.8208	0.9157	0.8623
LCD TV	2	0.9309	0.9350	0.9226

4. EXPERIMENTAL VERIFICATION

The objectives of the verification experiments were to demonstrate the functionality of the NILM system and assess its performance. Specific performance metrics of interest are how closely the system outputs ($\hat{Q}_t^{(k)}$ and $\hat{O}_t^{(k)}$) match the corresponding ground truth sequences ($Q_t^{(k)}$ and $O_t^{(k)}$), which are unknown to the model during the system tests. For the same test data, results are collected using the standard Viterbi algorithm and using the sparse Viterbi algorithm. This allows the impact of the replacing the standard Viterbi algorithm to be quantified in terms of system performance. Energy use estimations calculated using the expected value and the method proposed in Section 3 are compared as well. Additionally, energy predictions are calculated both when using the disaggregated states and when using the ground truth states. This latter case represents an idealized situation in which no errors are made in state disaggregation, i.e. $\hat{Q} = Q$. While this is an unrealistic scenario in practice, it effectively decouples the performance of the energy prediction methods from errors introduced in state disaggregation, allowing fair comparison of the estimation methods.

The experiments were conducted using individual appliance data from public databases intended for NILM research. The resources used include the ECO [25], Smart$*$ [26], and GREEND [27] datasets. The datasets contain high quality data at the aggregate and submetered level over a period of a few months. Although these datasets contain data from residential systems, it was possible to generate test cases that meet the assumption of known and fixed system composition by extracting device data from the datasets and summing their measurements to construct an aggregate observation sequence. Since the experiment is intended to assess the performance of the algorithms in systems with known composition, rather than their ability to recognize specific types of devices, the actual devices used in the tests is immaterial. The test systems contain residential devices simply because the available public NILM databases that contain the amount of data required come exclusively from residential settings.

For the full experiment, a 10-fold cross validation was used. For each monitored device, 10 days of measurements were extracted from the datasets, ensuring that the device in question was active on each day. From this collection, one day of data was selected for each device and included in a composite test sequence. This was repeated 10 times, such that 10 test sequences were created and each day of device data was included once. For each test sequence, the 9 remaining days served as training data for the device models used. The model was not trained on the data used in the test. This full procedure was repeated 10 times, with randomly generated time shifts for each device, so that 10 different aggregate test sequences were generated for each set of test devices. The sampling time was set at 5 seconds for training and testing. For simplicity, the same time scale used for the state disaggregation and energy use prediction functions. The time scale was limited by the time resolution of the available device data. Setting the sampling time lower than 5 seconds would have required reconstruction of missing samples for some devices, which would introduce bias in the experimental results.

4.1. Performance Assessments. Standard NILM performance metrics were used to assess the accuracy of the methods. These methods are summarized in [28], and were gathered from a variety of NILM studies. The state sequence accuracy of two-state devices was assessed using F-Score. For devices with more than two states, the modified F-Score proposed in [28] was used. This modified version is referred to as finite state F-score or FS-Score, and is intended for finite state machine devices. For all devices, the energy accuracy was assessed using estimation accuracy, proposed in [21]. To quantify the difference between the energy prediction methods, root mean square error (RMSE) was calculated for the predicted values as well. This metric was used in [11] for assessment at the device level. Here, RMSE values are calculated by state:

$$RMSE_j^{(k)} = \left(\frac{1}{T_j} \sum_{t:Q_t^{(k)}=j} \left(\hat{O}^{(k)} - O^{(k)} \right)^2 \right)^{1/2} \tag{35}$$

Here, $RMSE_j^{(k)}$ is the RMSE for state j of device k, and T_j is the total number of sample times for which $Q^{(k)} = j$.

4.2. Results. The results of the disaggregation experiments are summarized in Table 1. The state accuracies of the standard Viterbi algorithm and the sparse Viterbi algorithm are very similar on average. Despite being a greedy variant of its predecessor, the sparse Viterbi algorithm performs comparably for all devices. The significance of this similarity is that the disaggregated states calculated by the sparse Viterbi algorithm at each sampling instant are nearly as accurate as those calculated by the standard Viterbi algorithm, which are only available after the entire sequence of observation data has been recorded. The sparse Viterbi algorithm provides online operation with almost no degradation in accuracy.

The energy accuracy results at the device level are similar as well. The estimation accuracy metric provides an indication of how well the total energy used by the device is estimated by the predictions, characterizing long-term predictive accuracy. The expectation method is designed for long-term accuracy. The expected value is the best constant estimator of a sequence of random variables. The observation sequence of an N-state device can be split into N subsequences, one for each state, of independent and identically distributed random variables. The distributions of these subsequences are the conditional observation distributions. By the strong law of large numbers, the sample averages of the subsequences

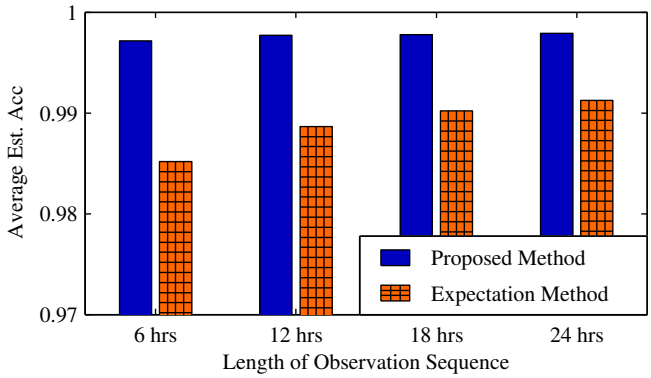

Figure 5. Average estimation accuracy by length of observation sequence.

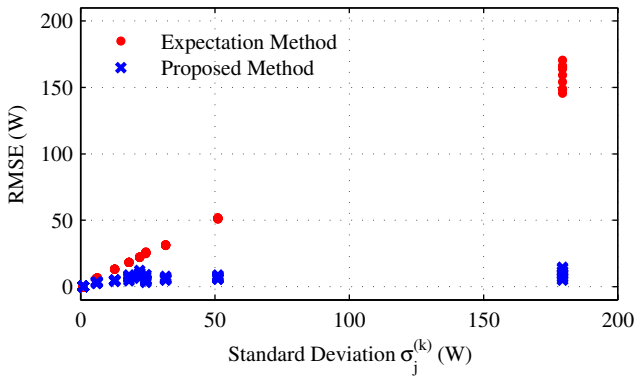

Figure 6. State RMSE of predicted observations plotted against the standard deviation of their observation distribution. All predictions used in this figure were calculated with ground-truth states.

converge to the expected values of their observation distributions as the length of the observation sequence increases. As a result, the accuracy of the expectation method increases with the length of the observation sequence under consideration. In other words, the contributions of behaviors that deviate from the expected value become smaller with respect to the cumulative energy of the observation sequence. The difference between the two methods is that the proposed method is capable of predicting these behaviors, which include transient features and deviations within states with high observation variance. The results in Table 1 show that the long-term accuracy of the proposed method is strictly greater than that of the expectation method. The magnitude of the difference between the methods is small, consistent with the decreasing energy contributions from transient and high-variance observations. As the time scale considered is shortened, the contributions from transient and variant behaviors become more significant, and the accuracy of the expectation method decreases. The accuracy of the proposed method, however, remains nearly constant. This is illustrated in Fig. 5, which shows the average predictive accuracy as the observation sequence length varies. The results in Fig. 5 were taken from the predictions based on ground truth states, to ensure fair comparison between methods.

The real performance advantages of the proposed method are its short-term accuracy characteristics. The estimation accuracies in Table 1 show that the proposed method maintains the long-term accuracy of the expectation method, but provide no insight into the predictive accuracies of the two methods at a given sampling instant. To characterize short time scale accuracy, the RMSE is calculated for each state. In Fig. 6, the RMSE values for each device state are plotted against the standard deviation of the state's observation distribution. These results correspond to tests using ground truth states, removing the effects of state errors. For the expectation method, error scales linearly with standard deviation. This matches intuition: the expected value is a poorer estimation of a random variable with higher variance. In contrast, the proposed method maintains low error for states with high variance. This relationship holds true when disaggregated states are used as well. Fig. 7 shows the difference in RMSE between the two methods both when using disaggregated states and when using ground truth states. In all cases, the RMSE of the proposed method is lower than that of the expectation method.

A comparison of the ground truth observations and actual predictions of the two methods for the refrigerator and TV are shown in Fig. 8 and Fig. 9, respectively. The refrigerator's behavior is characterized by transient spikes in active power corresponding to the inrush current of the starting compressor. The transient is consistent enough to require its own dedicated state. The TV is an electronic device, and experiences small variations in power as the image on the screen changes. These variations are not large enough to necessitate their own states, but are an immediately recognizable feature in the device's energy use profile. The proposed method is much more capable of predicting these transient effects, while the expectation method provides only a rough approximation. The performance difference shown in these plots is indicative of the overall improvement offered by the proposed method. For a 24 hour observation sequence (the same used to collect the results in Table 1), the predictions shown in Fig. 8 and Fig. 9 represent an increase in estimation accuracy of 1.75% for the refrigerator and 1.36% for the TV.

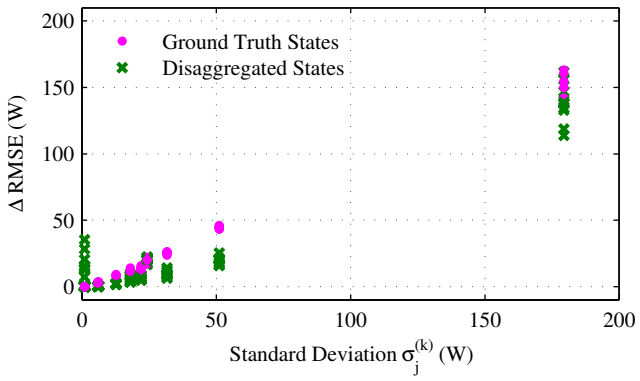

Figure 7. Difference in state RMSE values for predictions of the proposed method and expectation method. Predictions calculated from both disaggregated states and ground truth states are shown.

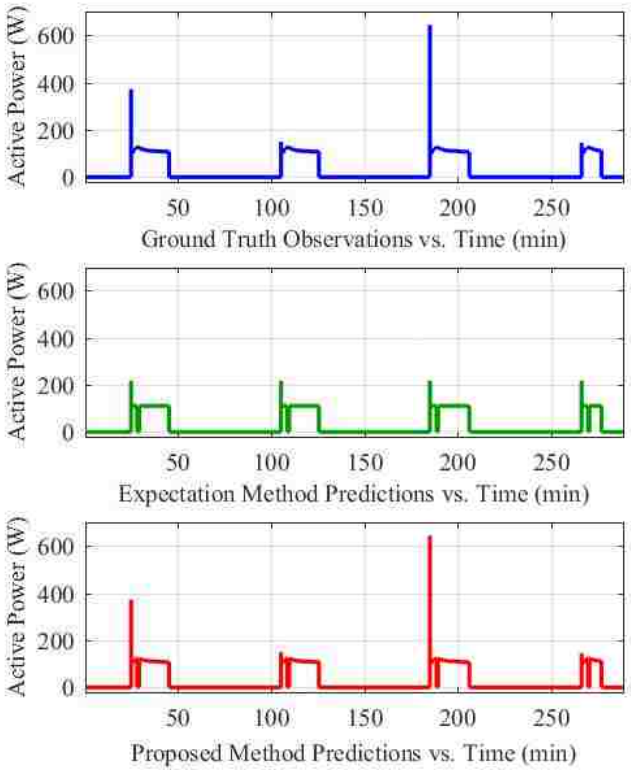

Figure 8. Comparison of ground truth and predicted observations for the refrigerator. All x-axis units shown in minutes.

These two appliances represent critical areas in the space of electrical devices. The transient behavior of the refrigerator is typical of devices with inductive or capacitive load characteristics, while the TV's power variations due to operational changes are typical of

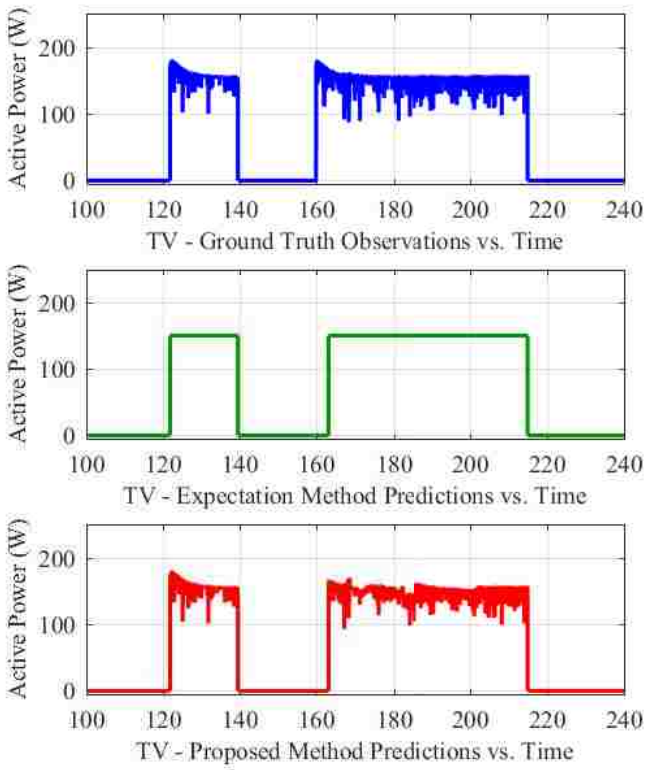

Figure 9. Comparison of ground truth and predicted observations for the LCD TV. All x-axis units shown in minutes.

electronic loads. While the total energy use during these transients and variations is small compared to the devices' cumulative energies, their recognition is of critical importance to applications involving the identification of atypical device behaviors.

5. CONCLUSION

The method proposed in this study provides accurate estimates of device activity for systems with known sets of devices. By removing the possibility of unknown devices, the optimal device-level predictions for the system-level measurements may be calculated at each instant. This method maintains the long-term accuracy of the conventional expectation method and significantly reduces the predictive error at any given instant. The increase in performance is greatest for states whose observation distributions have large variances,

since the proposed method is capable of predicting transients and deviations from the mean, while the expectation method ignores these features. Future work in this study will explore new methods of state sequence determination. The state inference calculations are the dominant limiting factors for both the accuracy and scalability of the method as a whole. A more scalable means of calculating states would extend the applicability of the NILM algorithm to much larger systems.

REFERENCES

[1] Z. Wang and G. Zheng, "Residential appliances identification and monitoring by a nonintrusive method," *IEEE Trans. Smart Grid*, vol. 3, no. 1, pp. 80–92, March 2012.

[2] G. Hart, "Nonintrusive appliance load monitoring," *Proc. IEEE*, vol. 80, no. 12, pp. 1870–1891, Dec 1992.

[3] D. He, W. Lin, N. Liu, R. Harley, and T. Habetler, "Incorporating non-intrusive load monitoring into building level demand response," *IEEE Trans. Smart Grid*, vol. 4, no. 4, pp. 1870–1877, Dec 2013.

[4] M. Zeifman and K. Roth, "Nonintrusive appliance load monitoring: Review and outlook," *IEEE Trans. Consum. Electron.*, vol. 57, no. 1, pp. 76–84, February 2011.

[5] Y. F. Wong, Y. Ahmet Sekercioglu, T. Drummond, and V. S. Wong, "Recent approaches to non-intrusive load monitoring techniques in residential settings," in *IEEE Symp. Computational Intelligence Applications In Smart Grid (CIASG)*, April 2013, pp. 73–79.

[6] Y. Du, L. Du, B. Lu, R. Harley, and T. Habetler, "A review of identification and monitoring methods for electric loads in commercial and residential buildings," in *Energy Conversion Congress and Exposition (ECCE), 2010 IEEE*, Sept 2010, pp. 4527–4533.

[7] C. Laughman *et al.*, "Power signature analysis," *IEEE Power Energy Mag.*, vol. 1, no. 2, pp. 56–63, Mar 2003.

[8] M. Berges, E. Goldman, H. S. Matthews, L. Soibelman, and K. Anderson, "User-centered nonintrusive electricity load monitoring for residential buildings," *J. Comput. Civ. Eng.*, vol. 25, no. 6, pp. 471–480, May 2011.

[9] H. Kim, M. Marwah, M. Arlitt, G. Lyon, and J. Han, "Unsupervised disaggregation of low frequency power measurements," in *SDM*, vol. 11, 2011, pp. 747–758.

[10] T. Zia, D. Bruckner, and A. Zaidi, "A hidden Markov model based procedure for identifying household electric loads," in *37th Conf. Industrial Electronics*, Nov 2011, pp. 3218–3223.

[11] O. Parson, S. Ghosh, M. Weal, and A. Rogers, "Non-intrusive load monitoring using prior models of general appliance types," in *26th Conference on Artificial Intelligence*, vol. 22, 2012, pp. 356–362.

[12] J. Liao, G. Elafoudi, L. Stankovic, and V. Stankovic, "Non-intrusive appliance load monitoring using low-resolution smart meter data," in *IEEE Int.l Conf. Smart Grid Communications (SmartGridComm)*, Nov 2014, pp. 535–540.

[13] S. Makonin, F. Popowich, I. Bajic, B. Gill, and L. Bartram, "Exploiting hmm sparsity to perform online real-time nonintrusive load monitoring," *IEEE Trans. Smart Grid*, vol. PP, no. 99, pp. 1–11, 2015.

[14] L. Rabiner, "A tutorial on hidden Markov models and selected applications in speech recognition," *Proc. IEEE*, vol. 77, no. 2, pp. 257–286, Feb 1989.

[15] J. Z. Kolter and T. Jaakkola, "Approximate inference in additive factorial HMMs with application to energy disaggregation," in *Proc. 15th Int. Conf. Artificial Intelligence and Statistics*, vol. 22, 2012, pp. 1472–1482.

[16] J. A. Mueller and J. W. Kimball, "An accurate method of energy use prediction for systems with known composition," in *Proc. 3rd. Int. Workshop on Nonintrusive Load Monitoring*, May 2016.

[17] Z. Ghahramani, "An introduction to hidden Markov models and bayesian networks," *Int. J. Pattern Recognition and Artificial Intell.*, vol. 15, no. 1, pp. 9–42, Jun. 2001.

[18] A. Zoha, A. Gluhak, M. Nati, and M. Imran, "Low-power appliance monitoring using factorial hidden Markov models," in *IEEE 8th Int.l Conf. Intelligent Sensors, Sensor Networks and Information Processing*, April 2013, pp. 527–532.

[19] L. Wang, X. Luo, and W. Zhang, "Unsupervised energy disaggregation with factorial hidden Markov models based on generalized backfitting algorithm," in *Proc. IEEE Region 10 Conf.*, Oct 2013, pp. 1–4.

[20] Z. Ghahramani and M. I. Jordan, "Factorial hidden Markov models," *Mach. Learn.*, vol. 29, no. 2-3, pp. 245–273, Nov. 1997.

[21] J. Z. Kolter and M. J. Johnson, "REDD: A Public Data Set for Energy Disaggregation Research," in *Proc. 2011 Workshop on Data Mining Applications in Sustainability (SustKDD 2011)*, Aug 2011.

[22] M. Zeifman and K. Roth, "Viterbi algorithm with sparse transitions (vast) for nonintrusive load monitoring," in *Computational Intelligence Applications In Smart Grid (CIASG), 2011 IEEE Symposium on*, April 2011, pp. 1–8.

[23] S. Makonin, F. Popowich, and I. Bajic, "Efficient matrix processing for nonintrusive load monitoring (NILM)," in *Proc. 2nd. Int. Workshop on Nonintrusive Load Monitoring*, June 2014.

[24] J. Forney, G.D., "The Viterbi algorithm," *Proc. IEEE*, vol. 61, no. 3, pp. 268–278, March 1973.

[25] C. Beckel, W. Kleiminger, R. Cicchetti, T. Staake, and S. Santini, "The ECO data set and the performance of non-intrusive load monitoring algorithms," in *Proc. 1st ACM Int.l Conf. Embedded Systems for Energy-Efficient Buildings (BuildSys 2014)*, Nov 2014, pp. 80–89.

[26] S. Barker *et al.*, "Smart*: An open data set and tools for enabling research in sustainable homes," in *Proc. 2012 Workshop on Data Mining Applications in Sustainability (SustKDD 2012)*, Aug 2012.

[27] A. Monacchi, D. Egarter, W. Elmenreich, S. D'Alessandro, and A. Tonello, "GREEND: An energy consumption dataset of households in Italy and Austria," in *IEEE Int. Conf. Smart Grid Communications (SmartGridComm)*, Nov 2014, pp. 511–516.

[28] S. Makonin and F. Popowich, "Nonintrusive load monitoring (NILM) performance evaluation," *Energy Efficiency*, vol. 8, no. 4, pp. 809–814, 2014.

IV. MODELING AND ANALYSIS OF DC MICROGRIDS AS STOCHASTIC HYBRID SYSTEMS

Jacob A. Mueller and Jonathan W. Kimball

Department of Electrical & Computer Engineering

Missouri University of Science and Technology

Rolla, Missouri 65409–0050

Email: jam8z4@mst.edu

ABSTRACT

This study proposes a method of predicting the influence of random load behavior on the dynamics of dc microgrids and distribution systems. This is accomplished by combining stochastic load models and deterministic microgrid models. Together, these elements constitute a stochastic hybrid system. The resulting model enables straightforward calculation of dynamic state moments, which are used to assess the probability of desirable operating conditions. Specific consideration is given to systems based on the dual active bridge (DAB) topology. Bounds are derived for the probability of zero voltage switching (ZVS) in DAB converters. A simple example is presented to demonstrate how these bounds may be used to improve ZVS performance as an optimization problem. Predictions of state moment dynamics and ZVS probability assessments are verified through comparisons to Monte Carlo simulations.

Keywords: Stochastic hybrid system, dual active bridge converter, generalized average model, zero voltage switching

1. INTRODUCTION

Randomness and uncertainty are unavoidable in practical power systems. Randomness is introduced by generation sources, loads, and even by tolerances of the passive elements that make up the system. It is difficult, if not impossible, to include all sources of uncertainty in system-level design and analysis. Often the most practical solution is to make conservative simplifying assumptions and analyze for the worst possible cases of operation. This is a common strategy when modeling loads in systems of power electronic converters. In describing load behavior, simple specifications are useful for evaluating boundary cases of operation (e.g. maximum/minimum power ratings), which are typically the most relevant to stability and efficiency constraints.

However, this approach offers no insight into how operating conditions evolve within conservative limits. While a system may be stable over a wide range of operation, certain regions within the operating space are likely more desirable than others. For instance, soft-switching significantly improves converter efficiency and reliability, but is typically only possible for a subset of operating conditions. It is preferable to either operate the converter in its soft-switching range as often as possible, or to design the soft-switching range around the typical system operating conditions. In either case, there is a need for quantitative descriptions of typical operating conditions as a function of the behavior of loads within the system. This study proposes a method of obtaining these descriptions by modeling converter and load behavior as a stochastic hybrid system (SHS).

The SHS framework is a powerful modeling tool that includes continuous dynamics, instantaneous events, and a variety of random effects [1]. The framework is challenging due to its sheer generality but offers powerful machinery for system analysis. In particular, it is possible to describe the evolution of moments of dynamic states as a system of ordinary differential equations (ODEs). In [2], a conventional power system was modeled as an SHS.

A similar approach was employed in [3] to analyze the stability of ac microgrid systems. The procedure for applying the SHS framework here is heavily influenced by the methods in [2], though the treatment of load behavior is different.

A central component of this study is the representation of practical loads. Practical loads are a combination of multiple independent devices. The devices in a given load behave randomly, and their cumulative current requirement is a function of their individual behaviors. A similar load modeling problem exists in the field of nonintrusive load monitoring (NILM). The objective of NILM is to obtain a detailed description of the behavior of devices in a system without monitoring each device individually [4, 5]. This is accomplished using probabilistic models of device behavior. A successful subset of NILM methods employs hidden Markov models (HMMs) to describe devices [6, 7, 8, 9]. The advantage of HMMs is that they can be trained to represent individual device behavior and then combined as needed to construct models of composite multi-device loads. This advantage is particularly useful when modeling multiple devices at different locations in a distribution system. The methods for constructing and manipulating device models proposed in [9] are the basis for the load representation in this study.

This study presents two contributions. The first is a new method of characterizing the dynamic behavior of dc microgrids and distribution systems as a function of random load influences. This includes a systematic approach to modeling load behavior, generating the SHS model, and solving for the important descriptors of system dynamics (namely low order moments). The second contribution is a method of assessing the probability of soft-switching for each of the converters in the system. In particular, the Cantelli inequality is used to determine upper and lower bounds on the probability of zero voltage switching (ZVS). While the tightness of the bounds depends on the combined influence of loads throughout the system, the bounds provide a useful mechanism for improving ZVS performance. The first contribution is applicable regardless of converter topology; the second is specific to the ZVS conditions of dual active bridge (DAB) converters.

The paper is structured as follows. Section 2 reviews relevant aspects of the SHS framework. Section 3 describes the representation of system loads and connection to the deterministic dynamic model. The SHS model is described in Section 4. ZVS probability assessments in DAB converters are discussed in Section 5. Verification experiments are described in Section 6, including an example of how the ZVS assessments can be used to improve soft-switching performance as an optimization problem.

2. BACKGROUND

The SHS framework is extremely general, and only a limited subset of its descriptive capability is used in this study. This section reviews fundamentals of the SHS approach that are relevant to the proposed method. A more comprehensive review of SHS formalisms can be found in [10].

Consider a dynamic model with the form

$$\dot{x} = f(x, y, u) \tag{1}$$

$$0 = g(x, y, u), \tag{2}$$

where x, y, and u are vectors denoting dynamic states, algebraic states, and inputs, respectively. For a given operating point, there is a corresponding affine model defined by

$$\dot{x} = Ax + Bu + C \tag{3}$$

$$y = Dx + Eu + F. \tag{4}$$

Let $Q(t)$ be a homogenous continuous-time Markov chain (CTMC) that transitions between a set of discrete modes $\mathcal{S}$ according to a transition rate matrix λ. At some time t, the occupation probabilities for each mode $q \in \mathcal{S}$ are denoted $\pi_q(t)$. Each mode corresponds to

a set of inputs u_q. The SHS model consists of a family of affine models linearized at each u_q. The model is

$$\dot{X}(t) = A_q X(t) + B_q u_q + C_q, \tag{5}$$

where $X(t)$ is a stochastic process that describes the dynamic state. The transition rate matrix λ fully determines mode transitions. That is, mode transitions are not explicitly time or state-dependent. A reset map defines how states and modes change on each transition. The reset map is denoted ϕ_{ij}, where $i, j \in \mathcal{S}$ are the modes before and after the transition, respectively. In this case, the function of the reset map is to avoid any discontinuities in the dynamic state. Therefore, ϕ_{ij} is defined as

$$\phi_{ij}(q, x) = (j, x). \tag{6}$$

The benefit of the SHS framework is the ability to quantify how dynamic states evolve over time. Specifically, it possible to derive a set of ODEs that characterize the evolution of moments of $X(t)$. The derivation begins with the extended generator for the SHS, which is the operator

$$\begin{aligned}(L\psi)(q, x) =& \frac{\partial}{\partial x}\psi(q, x) \cdot (A_q x + B_q u_q + C_q) \\ &+ \sum_{i,j \in \mathcal{S}} \lambda_{ij} \left((\psi(\phi_{ij}(q, x)) - \psi(q, x)) \right),\end{aligned} \tag{7}$$

where $\psi(q, x)$ is a suitably smooth test function and each λ_{ij} is an element of matrix λ. For the generator form shown in (7), which assumes that inputs are constant between mode transitions, $\psi(q, x)$ must be bounded and continuously differentiable with respect to x. More stringent requirements apply when the inputs are assumed to be stochastic. If inputs contain white noise components, $\phi(q, x)$ must be twice continuously differentiable with respect to x [1].

The generator becomes useful in Dynkin's formula, which describes the evolution of the expected value of the test function.

$$\frac{d}{dt}\mathbb{E}\left[\psi(Q(t), X(t))\right] = \mathbb{E}\left[(L\psi)(Q(t), X(t))\right] \tag{8}$$

To extract conditional moments of $X(t)$, the test function is defined as

$$\psi_i^{(m)}(q, x) = \delta_i(q)x^{(m)}, \tag{9}$$

where $\delta_i(q)$ is the Kronecker delta function and m is a vector of moment orders [2]. For a system with N dynamic states, m is an N-element row vector and $x^{(m)}$ defined as

$$x^{(m)} = \prod_{i=1}^{N} x_i^{m_i}. \tag{10}$$

For a given mode i, the expected value of $\psi(q, x)$ is equal to the conditional moments of $X(t)$.

$$\mathbb{E}\left[\psi_i^{(m)}(q, x)\right] = \mathbb{E}\left[X^{(m)}(t)\middle|Q(t) = i\right]\pi_i(t) \tag{11}$$

The unconditional moments of $X(t)$ may then be computed by the law of total expectation.

$$\mathbb{E}\left[X^{(m)}(t)\right] = \sum_{i\in\mathcal{S}} \mathbb{E}\left[\psi_i^{(m)}(q, x)\right] \tag{12}$$

Therefore, the evolution of the dynamic state moments is described by the set of ODEs corresponding to time derivatives of $\mathbb{E}\left[\psi_i^{(m)}(q, x)\right]$. To simplify notation, let the conditional moments be denoted by

$$\mu_i^{(m)}(t) = \mathbb{E}\left[\psi_i^{(m)}(q, x)\right] \tag{13}$$

Then according to (8), the ODEs of interest are

$$\dot{\mu}_i^{(m)}(t) = \mathbb{E}\left[(L\psi_i^{(m)})(Q(t), X(t))\right] \tag{14}$$

Conditional moments of algebraic states may be computed from the conditional moments of $X(t)$. Let conditional moments of the process $Y(t)$ be denoted $\zeta^{(m)}(t)$. Then the conditional moments are

$$\zeta_i^{(m)}(t) = \mathbb{E}\left[(D_i X(t) + E_i u_i + F_i)^{(m)} \middle| Q(t) = i\right] \pi_i(t) \tag{15}$$

Much of the practical difficulty in applying the SHS framework lies in computing usable expressions for the right-hand sides of (14) and (15). An expression for the right-hand side of (14) is given below, slightly modified from the form given in [2].

$$\begin{aligned}\dot{\mu}_i^{(m)}(t) = &\sum_{p=1}^{N} m_p \left(\sum_{r=1}^{N} a_{pr}^{(i)} \mu_i^{(m-e_p+e_r)}(t) + \mu_i^{(m-e_p)}(t) v_{i,p} \right) \\ &+ \sum_{j \in \mathcal{S}_i^-} \lambda_{ji} \mu_j^{(m)}(t) - \sum_{k \in \mathcal{S}_i^+} \lambda_{ik} \mu_i^{(m)}(t)\end{aligned} \tag{16}$$

In this equation, $a_{pr}^{(i)}$ is the p^{th} row, r^{th} column element of A_i, $v_{i,p}$ is the p^{th} element of vector $v_i = B_i u_i + C_i$, e_p and e_r are elementary row vectors, and $\mathcal{S}_i^-$ and $\mathcal{S}_i^+$ denote the sets of modes that transition into and out of mode i, respectively.

3. DYNAMIC MODEL AND LOAD PROCESS

The dynamic model used in this study describes a dc microgrid or distribution system consisting of loads, sources, and DAB converters. The deterministic model is constructed according to the procedure in [11]. In principle, the SHS microgrid model described in Sec. 4 is compatible with any system-level dynamic model that can be linearized and expressed in the form of (3) and (4), regardless of the topology of the converters in the system. The prediction of ZVS probabilities in Sec. 5, however, is specific to the DAB topology.

In the simplest case, the dynamic model describes a single voltage-controlled DAB with a current-source load. This is shown in Fig. 1. The inputs to the system-level model are source voltages/currents, load currents, and voltage reference commands for closed-loop

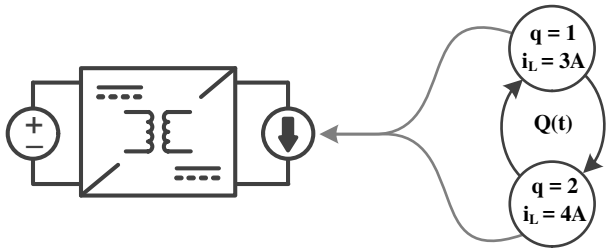

Figure 1. Single DAB converter and two-mode load process.

voltage controllers. Each mode of the process $Q(t)$ corresponds to a set of inputs. Since the present focus is on modeling load behavior, source parameters and voltage references are assumed to be constant, and differences between inputs are restricted to load current values.

The load process $Q(t)$ represents the influence of random loads on the system. The load modeling objective is to identify parameters that accurately describe $Q(t)$, namely the transition rate matrix λ. Each converter regulates a local bus voltage, which may supply power to multiple individual devices. When multiple devices are present, the total load seen by the system is a combination of the individual device requirements. The approach taken here involves modeling each device individually, and combining device-level models to construct a model of the total load behavior.

Each individual device model is a discrete-time Markov chain. The Markov chain consists of a set of modes, mode transition probabilities, and possible output values. Device i is represented by M_i modes. At each discrete instant, the probability of transitioning from mode j to mode k is represented by element p_{jk} of transition matrix $P_i \in \mathbb{R}^{M_i \times M_i}$. In the present study, the output for each mode is a single, constant value of load current, as shown in Fig. 1. Load currents of device i are contained in vector $i_{Li} \in \mathbb{R}^{1 \times M_i}$. Markov chains are easily trained using maximum likelihood estimation. The only information required to train the device model is a sequence of observations (either power or current measurements), recorded with a known sampling period, T_S. A simple model training procedure is given in [9].

Individual device models are combined to generate models of composite loads. Let M, P, and i_L (with no subscripts) denote the parameters of the combined model. When the first device is included in the composite model, $M = M_1$, $P = P_1$, and $i_L = i_{L1}$. For including all other devices $i > 1$, the model combination equations are defined recursively:

$$P = P \otimes P_i \tag{17}$$

$$i_L = i_L \otimes \mathbf{1}(M_i) + \mathbf{1}(M) \otimes i_{Li} \tag{18}$$

$$M = MM_i, \tag{19}$$

where $\otimes$ denotes the Kronecker product and $\mathbf{1}(M)$ is a row vector of M elements equal to 1. This combination process follows the procedure in [9], with small modifications for constant load current outputs.

For the conceptual diagram in Fig. 1, which involves only one load, each mode corresponds to a single scalar value. In the more general case, where loads exist at multiple points in the system, each mode corresponds to a vector of load currents. The combination in (18) applies regardless of the locations of loads in the system.

Once all individual devices have been included in the composite model, the M modes of the Markov chain are exactly the modes of $Q(t)$. However, $Q(t)$ is continuous in time, whereas the P defines a discrete-time Markov chain. In general, it is not possible to convert a discrete-time Markov chain into a CTMC. However, since the device models are trained using a known sampling time, it is possible to approximate the parameters of the CTMC. The elements of the transition rate matrix λ can be determined from P as:

$$\lambda_{ii} = -\frac{1 - p_{ii}}{T_S} \tag{20}$$

$$\lambda_{ij} = -\frac{\lambda_{ii} p_{ij}}{1 - p_{ii}}. \tag{21}$$

4. SHS MICROGRID MODEL

4.1. SHS Model. Let $\mu_i^{|n|}(t)$ denote the set of all n^{th} moments of $X(t)$ conditional on mode i. That is, $\mu_i^{|n|}(t)$ is a column vector of all moments defined in (13) for which the one-norm of m is equal to n. In terms of the dynamic states, $\mu_i^{|n|}(t)$ can be understood as

$$\mu_i^{|n|}(t) = \mathbb{E}\left[\left(\prod_{k=0}^{n} X(t)\right)\middle| Q(t) = i\right]\pi_i(t), \tag{22}$$

where the product symbol denotes the Kronecker product, such that the term in parentheses is the Kronecker product of the state vector and itself n times. By convention, this term is simply 1 for $n = 0$. In this way, the 0^{th} order moments are the mode occupation probabilities:

$$\mu_i^{|0|}(t) = \mathbb{E}\left[1\middle| Q(t) = i\right]\pi_i(t) = \pi_i(t). \tag{23}$$

First and second order moments are

$$\mu_i^{|1|}(t) = \mathbb{E}\left[X(t)\middle| Q(t) = i\right]\pi_i(t) \tag{24}$$

$$\mu_i^{|2|}(t) = \mathbb{E}\left[X(t) \otimes X(t)\middle| Q(t) = i\right]\pi_i(t), \tag{25}$$

where $\otimes$ is the Kronecker product. To represent moments for all modes, let vector $\mu^{|n|}(t)$ be defined as

$$\mu^{|n|}(t) = \begin{bmatrix} \mu_1^{|n|}(t) \\ \vdots \\ \mu_M^{|n|}(t) \end{bmatrix}. \tag{26}$$

In this way, $\mu^{|0|}(t) \in \mathbb{R}^{M\times 1}$ contains mode occupation probabilities, $\mu^{|1|}(t) \in \mathbb{R}^{NM\times 1}$ contains all first order moments, $\mu^{|2|}(t) \in \mathbb{R}^{N^2M\times 1}$, contains all second order moments, and so on.

Note that this formulation draws a distinction between correlations e.g. $\mathbb{E}[X_1(t)X_2(t)]$ and $\mathbb{E}[X_2(t)X_1(t)]$, while these two quantities are actually the same. For a system with N dynamic states, the number of unique n^{th} order moments is

$$N_u(n) = \binom{N+n-1}{n}. \tag{27}$$

The reason for this construction is to facilitate a simplified method of obtaining the set of moment ODEs. Once the full linear system has been obtained, redundant moments are eliminated through basic matrix operations. To distinguish between moment vectors, the sets of unique moments are denoted $\hat{\mu}_i^{|n|}(t)$. In the present study, this difference in notation is only necessary for the second order moments, since $\hat{\mu}_i^{|n|}(t) = \mu_i^{|n|}(t)$ for $n < 2$.

For the SHS formulation used in this study, moment dynamic equations depend only on moments of equal or lower order, avoiding the need for moment-closure methods [2]. In fact, (16) reveals that the dynamics of moments of order n are only directly dependent on moments of order n and $n-1$. For a given moment characterized by m, (16) shows that $\dot{\mu}_i^{(m)}(t)$ depends on $\mu_i^{(m-e_p+e_r)}(t)$, $\mu_i^{(m-e_p)}(t)$, $\mu_i^{(m)}(t)$, and $\mu_j^{(m)}(t)$ for other modes $j \in \mathcal{S}$. Recall that the order of moment $\mu_i^{(m)}(t)$ is equal to the one-norm of m. Trivially, $\mu_i^{(m)}(t)$ and $\mu_j^{(m)}(t)$ have the same order. If the order of $\mu_i^{(m)}(t)$ is n, then since e_p and e_r are unit vectors, the orders of $\mu_i^{(m-e_p+e_r)}(t)$ and $\mu_i^{(m-e_p)}(t)$ must be n and $n-1$, respectively.

Consequently, it is possible to express the system of ODEs for n^{th} order moments as

$$\dot{\mu}^{|n|}(t) = G^{(n)}\mu^{|n|}(t) + H^{(n)}\mu^{|n-1|}(t) \tag{28}$$

Matrices $G^{(n)}$ and $H^{(n)}$ follow from (16), but provide a more manageable structure to the definition of the SHS model.

Simplified expressions for $G^{(n)}$ and $H^{(n)}$ are given here for low-order moments. The 0^{th} order moments are the mode occupation probabilities of the CTMC. Therefore $H^{(0)} = 0$ and $G^{(0)} = \lambda^T$, where the transpose is due to the fact $\mu^{|0|}(t)$ is a column vector. For first and second order moments, both $G^{(n)}$ and $H^{(n)}$ may be constructed primarily as block diagonal combinations of submatrices for each mode:

$$G^{(n)} = \begin{bmatrix} G_1^{(n)} & 0 & \cdots & 0 \\ 0 & G_2^{(n)} & \cdots & 0 \\ \vdots & \vdots & \ddots & \vdots \\ 0 & 0 & \cdots & G_M^{(n)} \end{bmatrix} + \left(\lambda^T \otimes I(N^n)\right) \tag{29}$$

$$H^{(n)} = \begin{bmatrix} H_1^{(n)} & 0 & \cdots & 0 \\ 0 & H_2^{(n)} & \cdots & 0 \\ \vdots & \vdots & \ddots & \vdots \\ 0 & 0 & \cdots & H_M^{(n)}, \end{bmatrix} \tag{30}$$

where $I(N^n)$ is the N^n-dimensional identity matrix. In the case of first order moments, the submatrices for each mode are

$$G_i^{(1)} = A_i \tag{31}$$

$$H_i^{(1)} = v_i. \tag{32}$$

For second order moments, the submatrices are calculated using a transformation matrix, W_m, which is constant for all modes.

$$G_i^{(2)} = W_m \left(I(N) \otimes A_i\right) \tag{33}$$

$$H_i^{(2)} = W_m \left(I(N) \otimes v_i\right). \tag{34}$$

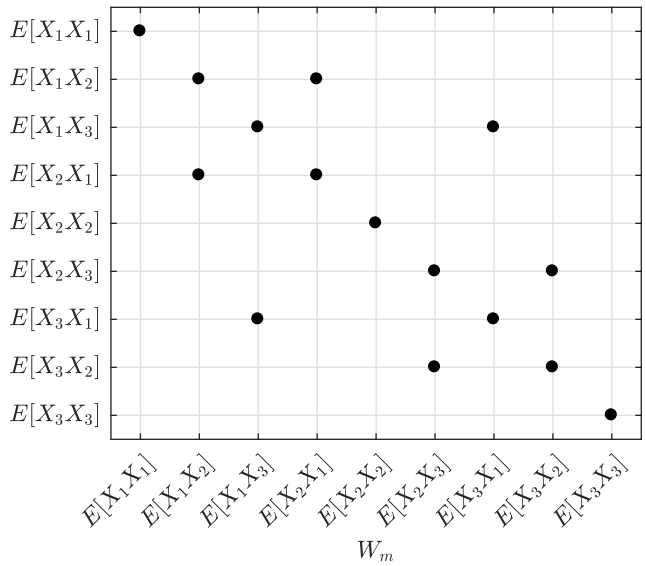

Figure 2. Example of transformation matrix W_m for a 3-state system.

The role of W_m is to describe the structure of the moments. Each row of W_m corresponds to the dynamic equation for a particular conditional second order moment. The elements of W_m are equivalent to the values of the coefficient m_p in (16). Since W_m describes second order moments, all rows and columns sum to 2. Note that a transformation appears in the equations for second order moments, but not in equations for first-order moments (i.e. (31) and (32)). The same connection to values of m_p in (16) applies to these equations, but if a transformation was defined it would simply be the identity matrix.

The sparsity pattern of W_m for a simple system with $N = 3$ states is shown in Fig. 2. To illustrate how W_m corresponds to moment relationships, conditional second order moments are shown on the horizontal and vertical axes. For legibility, time dependence and conditioning are omitted from the notation used in the figure.

Matrix W_m can be interpreted as a representation of how second order moments relate to each other. Since moments $\mathbb{E}[X_1(t)X_2(t)|Q(t) = q]$ and $\mathbb{E}[X_2(t)X_1(t)|Q(t) = q]$ are the same, the equations that govern their dynamics must both depend on exactly the same two moments. Furthermore, moments whose dynamics depend on $\mathbb{E}[X_1(t)X_2(t)|Q(t) = q]$ must also depend on $\mathbb{E}[X_2(t)X_1(t)|Q(t) = q]$. Fig. 2 shows that this is the case.

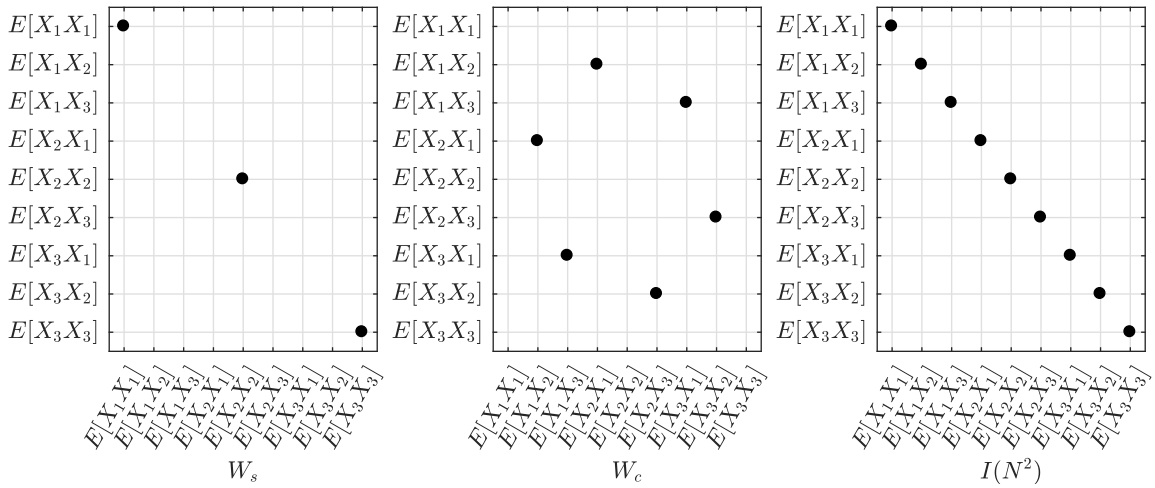

Figure 3. Decomposition of W_m into W_s, W_c, and $I(N^2)$ for a 3-state system.

A convenient way to decompose the structure of W_m is to separate each moment's dependencies into self-dependence and dependence on its equivalent moment. This separation may be accomplished as

$$W_m = W_s + W_c + I(N^2), \tag{35}$$

where the identity matrix describes each moment's self-dependence and W_c describes dependence on the equivalent moment. The last matrix, W_s, describes an additional self dependence for moments of the form $\mathbb{E}[X_i(t)X_i(t)|Q(t) = q]$. The decomposition is shown graphically in Fig. 3. The nonzero elements W_s and W_c are:

$$W_c\big(N(i-1)+j, N(j-1)+i\big) = 1, \quad \forall i, j \in \{1, \cdots, N\}, \quad i \neq j \tag{36}$$

$$W_s\big(N(i-1)+i, N(i-1)+i\big) = 1, \quad \forall i \in \{1, \cdots, N\} \tag{37}$$

4.2. Elimination of Redundant Second Order Moments. The equivalent moments contained in $\mu_i^{|2|}(t)$ decrease the computational efficiency of the SHS model. Moreover, matrix $G_i^{(2)}$ will be rank deficient unless redundant moments are eliminated, meaning stationary moment solutions cannot be calculated through linear equations. However, re-

dundant moments may be eliminated from the system using the transformation matrix W_m and its decomposed forms W_c and W_s. Redundant moments are eliminated at the sub-matrix level, such that the reduced system is constructed through the same block-diagonal procedure. Considering only unique second order moments, the reduced system is

$$\dot{\hat{\mu}}^{|2|}(t) = \hat{G}^{(2)}\hat{\mu}^{|2|}(t) + \hat{H}^{(2)}\mu^{|1|}(t) \tag{38}$$

$$\hat{G}^{(2)} = \begin{bmatrix} \hat{G}_1^{(2)} & 0 & \cdots & 0 \\ 0 & \hat{G}_2^{(2)} & \cdots & 0 \\ \vdots & \vdots & \ddots & \vdots \\ 0 & 0 & \cdots & \hat{G}_M^{(2)} \end{bmatrix} + \left(\lambda^T \otimes I(N_u(2))\right) \tag{39}$$

$$\hat{H}^{(2)} = \begin{bmatrix} \hat{H}_1^{(2)} & 0 & \cdots & 0 \\ 0 & \hat{H}_2^{(2)} & \cdots & 0 \\ \vdots & \vdots & \ddots & \vdots \\ 0 & 0 & \cdots & \hat{H}_M^{(2)} \end{bmatrix}. \tag{40}$$

The process of eliminating redundant moments consists of two linear transformations. First, rows of $G_i^{(2)}$ that describe dynamics of redundant moments must be eliminated. Second, columns of $G_i^{(2)}$ corresponding to dependence on equivalent moments must be summed together. One additional matrix, denoted R, is needed to derive these transformations. Let $\hat{\mu}_i^{|2|}(t) = R\mu_i^{|2|}(t)$, where R eliminates all redundant moments from $\mu_i^{|2|}(t)$. Matrix R is easily specified from the locations of unique moments in $\mu_i^{|2|}(t)$. The indices of the unique moments are an ordered set of $N_u(2)$ integers, defined by:

$$S_u = \bigcup_{i=1}^{N} \{(i-1)N + i,\ \cdots,\ iN\}. \tag{41}$$

Then the $N_u(2)$ rows of R are the rows of the N^2 identity matrix that correspond to unique moments: if j is the i^{th} element of S_u, the i^{th} row of R is the j^{th} row of $I(N^2)$.

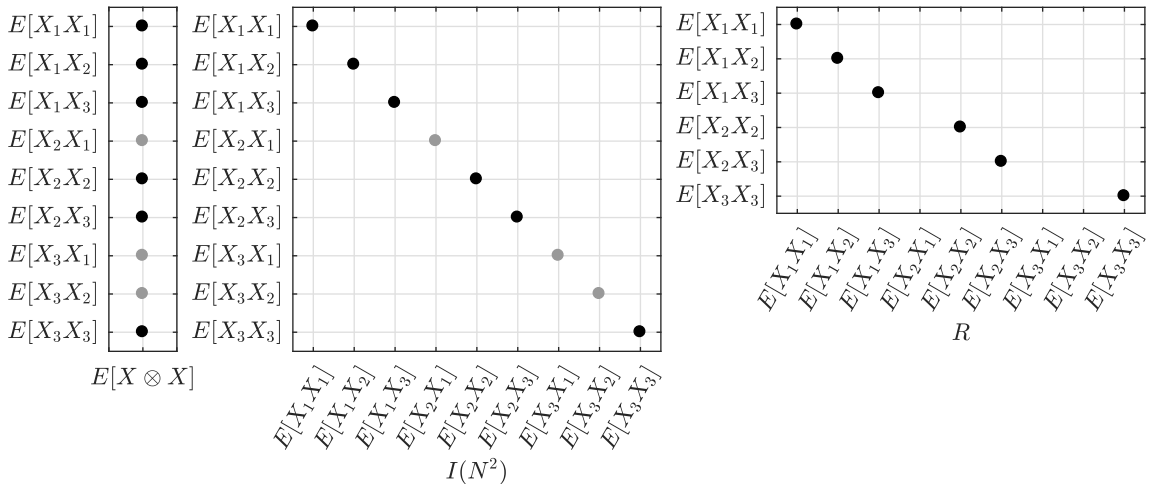

Figure 4. Specification of R from indicies of unique moments.

In the case of the simplified 3-moment system, the indicies of unique moments are:

$$S_u = \{1,\ 2,\ 3\} \cup \{5,\ 6\} \cup \{7\}\,. \tag{42}$$

For this system, the 4^{th} element of S_u is 5. Therefore, the 4^{th} row, 5^{th} column element of R is equal to 1. This is shown graphically in Fig. 4.

Matrix R is exactly the transformation needed to eliminate redundant moment equations from the model. Premultiplying $G_i^{(2)}$ and $H_i^{(2)}$ by R eliminates rows that describe dynamics of redundant moments. This is all that is needed to determine $\hat{H}_i^{(2)}$ from $H_i^{(2)}$. To complete the definition of $\hat{G}_i^{(2)}$, columns of $G_i^{(2)}$ that correspond to dependence on equivalent moments must be summed. Relationships between equivalent moments are contained in W_m. The relevant information is in W_c and $I(N^2)$; the additional self-dependence described by W_s is irrelevant to moment equivalence. Postmultiplying $G_i^{(2)}$ by $\left(W_c + I(N^2)\right)^T$ sums the necessary columns. The full transformation is

$$\hat{G}_i^{(2)} = RG_i^{(2)}\left[R(W_c + I(N^2))\right]^T \tag{43}$$

$$\hat{H}_i^{(2)} = RH_i^{(2)}. \tag{44}$$

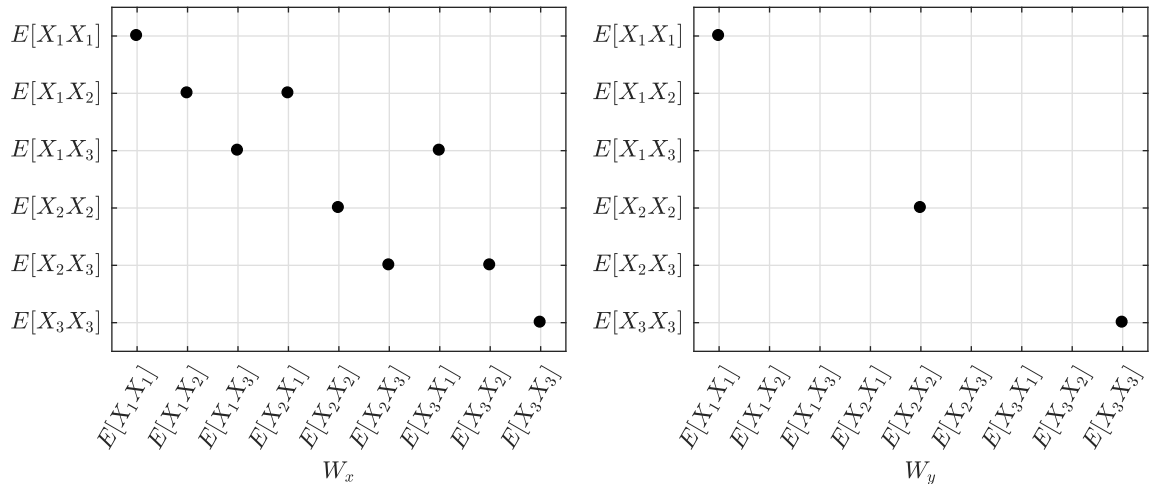

Figure 5. Sparsity pattern of final transformation matrices used to calculate reduced subsystem matrices.

In comparison to the submatrices in (33) and (34), these definitions produce a second order system with significantly reduced size. More importantly, matrix $\hat{G}^{(2)}$ will always have full rank, making it possible to solve for stationary moments.

A more efficient alternative to (43) and (44) is to directly calculate $\hat{G}_i^{(2)}$ and $\hat{H}_i^{(2)}$, rather than reducing them from $G_i^{(2)}$ and $H_i^{(2)}$. Let two new transformations, W_x and W_y, be defined as

$$W_x = R\left(W_c + I(N^2)\right) \tag{45}$$

$$W_y = RW_s. \tag{46}$$

Sparsity patterns for these matrices are shown in Fig. 5. The reduced subsystem matrices may be calculated from W_x and W_y as

$$\hat{G}_i^{(2)} = \left(W_x + W_y\right)\left(I(N) \otimes A_i\right)\left(W_x^T\right) \tag{47}$$

$$\hat{H}_i^{(2)} = \left(W_x + W_y\right)\left(I(N) \otimes v_i\right). \tag{48}$$

$W_x \leftarrow [0]_{N_u(2),N^2}$, $W_y \leftarrow [0]_{N_u(2),N^2}$
$k \leftarrow 1$
for $i \leftarrow 1, \cdots, N$ **do**
    $W_y(k, N(i-1)+i) \leftarrow 1$
    for $j \leftarrow i, \cdots, N$ **do**
        $W_x(k, N(i-1)+j) \leftarrow 1$
        $W_x(k, N(j-1)+i) \leftarrow 1$
        $k \leftarrow k+1$
    end for
end for

Figure 6. Pseudocode for construction of W_x and W_y.

The definitions in (45) and (45) are only given for clarity of derivation. In practice, W_x and W_y are more efficiently constructed through simple algorithmic specifications. Pseudocode for generating these matrices is shown in Fig. 6. W_x and W_y are the only transformations required to calculate the reduced subsystem matrices, so the ability to specify them directly is a significant advantage. When W_x and W_y are constructed according to the pseudocode in Fig. 6, the final SHS model may be formed without calculating R, W_m, W_s, or W_c.

4.3. Final Model and Steady-State Moments. After reducing the second order system, the final model for low order moments is

$$\dot{\mu}^{|0|}(t) = G^{(0)}\mu^{|0|}(t) \tag{49}$$

$$\dot{\mu}^{|1|}(t) = G^{(1)}\mu^{|1|}(t) + H^{(1)}\mu^{|0|}(t) \tag{50}$$

$$\dot{\hat{\mu}}^{|2|}(t) = \hat{G}^{(2)}\hat{\mu}^{|2|}(t) + \hat{H}^{(2)}\mu^{|1|}(t) \tag{51}$$

where $G^{(0)} = \lambda^T$ and $G^{(1)}$, $H^{(1)}$, $\hat{G}^{(2)}$, and $\hat{H}^{(2)}$ are specified by submatrices in (31), (32), (47), and (48), respectively. Noting that $\hat{\mu}^{|n|}(t) = \hat{\mu}^{|n|}(t)$, $\hat{G}^{(n)} = G^{(n)}$, and $\hat{H}^{(n)} = H^{(n)}$ for $n = 0$ and $n = 1$, the general form of an n^{th} order SHS model may be expressed as

$$\dot{\hat{\mu}}^{|n|}(t) = \hat{G}^{(n)}\hat{\mu}^{|n|}(t) + \hat{H}^{(n)}\hat{\mu}^{|n-1|}(t) \tag{52}$$

$$\hat{G}^{(n)} = \begin{bmatrix} \hat{G}_1^{(n)} & 0 & \cdots & 0 \\ 0 & \hat{G}_2^{(n)} & \cdots & 0 \\ \vdots & \vdots & \ddots & \vdots \\ 0 & 0 & \cdots & \hat{G}_M^{(n)} \end{bmatrix} + \left(\lambda^T \otimes I(N_u(n))\right) \tag{53}$$

$$\hat{H}^{(n)} = \begin{bmatrix} \hat{H}_1^{(n)} & 0 & \cdots & 0 \\ 0 & \hat{H}_2^{(n)} & \cdots & 0 \\ \vdots & \vdots & \ddots & \vdots \\ 0 & 0 & \cdots & \hat{H}_M^{(n)} \end{bmatrix}. \tag{54}$$

Submatrices $\hat{G}_i^{(n)}$ and $\hat{H}_i^{(n)}$ are

$$\hat{G}_i^{(n)} = R^{(n)} W_m^{(n)} \left(I(N^{n-1}) \otimes A_i\right) \left[R^{(n)} \left(W_c^{(n)} + I(N^n)\right)\right] \tag{55}$$

$$\hat{H}_i^{(n)} = R^{(n)} W_m^{(n)} \left(I(N^{n-1}) \otimes v_i\right) \left[R^{(n-1)} \left(W_c^{(n-1)} + I(N^{n-1})\right)\right] \tag{56}$$

where $R^{(n)}$, $W_m^{(n)}$, and $W_c^{(n)}$ are transformation matrices for the n^{th} order moments.

This system is suitable for predicting moment dynamics. In some cases, however, it may be desirable to simply compute the moments for steady-state behavior. Let t_F represent some final time at which the stationary distribution has been reached, and the left-hand side of (52) is 0. The 0^{th} moments are the stationary distribution of the CTMC, or $\pi(t_F)$. Therefore, $\mu^{|0|}(t_F)$ may be determined by solving $0 = \lambda^T \mu^{|0|}(t_F)$ with the constraint

$$\sum_{i=1}^{M} \mu_i^{|0|}(t_F) = 1. \tag{57}$$

The rest of the stationary moments are then:

$$\hat{\mu}^{|n|}(t_F) = \left(\hat{G}^{(n)}\right)^{-1} \left(-\hat{H}^{(1)} \hat{\mu}^{|n-1|}(t_F)\right). \tag{58}$$

5. ANALYSIS OF ZVS PERFORMANCE

5.1. ZVS Conditions. In single phase shift modulation, the conditions for ZVS may be expressed in terms of phase shift and voltage gain [12, 13, 14]. Assuming forward power transfer, ZVS occurs in both H-bridges when the following inequalities are satisfied:

$$d \geq \frac{1}{2} - \frac{v_o}{2v_c} \tag{59}$$

$$d \geq \frac{1}{2} - \frac{v_c}{2v_o}. \tag{60}$$

Since both v_o and v_c can be assumed to be strictly positive, these inequalities may be rearranged as

$$2dv_c + v_o - v_c \geq 0 \tag{61}$$

$$2dv_o + v_c - v_o \geq 0. \tag{62}$$

Further, since d is a function of the controller states, these conditions may be expressed entirely in terms of the states and inputs of the DAB model. The resulting expressions are denoted $h_d(x, u)$ and $h_u(x, u)$, with subscripts indicating that they pertain to the conditions for voltage step-down and step-up operation, respectively.

$$h_d(x, u) \triangleq 2v_c \left(k_p(v_{ref} - v_o) + \gamma\right) + v_o - v_c \tag{63}$$

$$h_u(x, u) \triangleq 2v_o \left(k_p(v_{ref} - v_o) + \gamma\right) + v_c - v_o \tag{64}$$

In the context of the deterministic model, ZVS operation in a given converter may be determined by checking whether $h_d(x, u) \geq 0$ and $h_u(x, u) \geq 0$.

5.2. ZVS Moments and Bounds. In the SHS model, ZVS conditions are treated similarly to algebraic states. That is, $h_d(x, u)$ and $h_u(x, u)$ are put into the linearized form of (4), and their moments are computed according to (15). The following discussion

considers a generic scalar-valued function $h(x, u)$, which may represent either of the two ZVS condition equations. If x_q is the deterministic steady-state corresponding to input u_q, the linear approximation of $h(x, u)$ is

$$h(x, u) \approx D_q x + E_q u_q + f_q, \tag{65}$$

where D_q and E_q are derivative vectors and f_q is a constant scalar offset.

$$D_q = \left.\frac{\partial h(x, u)}{\partial x}\right|_{\substack{u=u_q \\ x=x_q}} \tag{66}$$

$$E_q = \left.\frac{\partial h(x, u)}{\partial u}\right|_{\substack{u=u_q \\ x=x_q}} \tag{67}$$

$$f_q = h(x_q, u_q) - D_q x_q - E_q u_q \tag{68}$$

Since $h(x, u)$ is a scalar, (15) can be simplified. Let the conditional moments of $h(x, u)$ in mode i be denoted $\xi_i^{(n)}(t)$. Then each $\xi_i^{(n)}(t)$ can be computed from dynamic state moments as

$$\xi_i^{(n)}(t) = r_i^n \mu_i^{|0|}(t) + \sum_{k=1}^{n} \binom{n}{k} r_i^{n-k} \left(\prod_{j=1}^{k} D_i \right) \mu_i^{|n|}(t), \tag{69}$$

where the Kronecker product is used for the products of vector D_i, and r_i is defined as

$$r_i = E_i u_i + f_i. \tag{70}$$

The first few moments of $\xi_i^{(n)}(t)$ are

$$\xi_i^{(1)}(t) = r_i \mu_i^{|0|}(t) + D_i \mu_i^{|1|}(t) \tag{71}$$

$$\xi_i^{(2)}(t) = r_i^2 \mu_i^{|0|}(t) + 2 r_i D_i \mu_i^{|1|}(t) + (D_i \otimes D_i)\, \mu_i^{|2|}(t) \tag{72}$$

The second order moment can alternatively be expressed as a function of unique second order dynamic state moments using the transformation from the previous section.

$$\xi_i^{(2)}(t) = r_i^2 \mu_i^{|0|}(t) + 2 r_i D_i \mu_i^{|1|}(t) + (D_i \otimes D_i) \left(W_x^T\right) \hat{\mu}_i^{|2|}(t) \tag{73}$$

Finally, the unconditional moments are the sum of each the conditional moments for each mode.

$$\mathbb{E}\left[h(x,u)^n\right] \approx \xi^{(n)}(t) = \sum_{i=1}^{M} \xi_i^{(n)}(t) \tag{74}$$

The moments of $h_d(x,u)$ and $h_u(x,u)$ make it possible to assess the probability of ZVS. The probability of ZVS corresponds to the probability these functions are greater than zero, according to the ZVS condition equations. Using the Cantelli inequality, a bounds on the probability of ZVS can be defined in terms of first and second moments. For generic random variable X and constant a, the Cantelli inequality is [15]:

$$\mathbb{P}\left[X - \mu_X \geq a\right] \begin{cases} \leq & \frac{\sigma_X^2}{\sigma_X^2 + a^2} \quad a \geq 0 \\ \geq & 1 - \frac{\sigma_X^2}{\sigma_X^2 + a^2} \quad a < 0 \end{cases}, \tag{75}$$

where μ_X and σ_X^2 are the first and second central moments of X. Letting $a = -\mu_X$ the inequality is

$$\mathbb{P}\left[X \geq 0\right] \begin{cases} \leq & \frac{\sigma_X^2}{\sigma_X^2 + \mu_X^2} \quad \mu_X < 0 \\ \geq & 1 - \frac{\sigma_X^2}{\sigma_X^2 + \mu_X^2} \quad \mu_X \geq 0 \end{cases}. \tag{76}$$

Applying this inequality to $h(x,u)$, and substituting raw moments for central moments, the upper limits and lower limits on the probability $\mathbb{P}[h(x,u) \geq 0]$ are:

$$\mathbb{P}\left[h(x,u) \geq 0\right] \geq \begin{cases} \frac{(\xi^{(1)}(t))^2}{\xi^{(2)}(t)}, & \xi^{(1)}(t) \geq 0 \\ 0, & \xi^{(1)}(t) < 0 \end{cases} \tag{77}$$

$$\mathbb{P}\left[h(x,u) \geq 0\right] \leq \begin{cases} 1, & \xi^{(1)}(t) \geq 0 \\ 1 - \frac{(\xi^{(1)}(t))^2}{\xi^{(2)}(t)}, & \xi^{(1)}(t) < 0 \end{cases} \tag{78}$$

These expressions are valid for $h_d(x,u)$, $h_u(x,u)$, and for any other functions that encode operating conditions as scalar comparisons to zero.

6. VERIFICATION

The verification experiments for this study consider a 7-bus test system. The system contains 5 DAB converters and is structured as shown in Fig. 7. All DAB converters are closed-loop, voltage-controlled. The converter output terminals are indicated with a dot in Fig. 7. Hardware and control parameters are given in Table 1. Randomness is introduced through the loads of converters 3, 4, and 5. Markov chains that describe the individual devices in these three loads are shown in Fig. 8.

Table 1. Control and Hardware Parameters for 7-Bus System

Parameter	Value	Parameter	Value
$C_{in}^1, C_{in}^2, C_{in}^3, C_o^1, C_o^2, C_o^3$	200 μF	v_{ref}^1	48 V
$C_{in}^4, C_{in}^5, C_o^4, C_o^5$	40 μF	v_{ref}^2, v_{ref}^3	42 V
$L_t^1, L_t^2, L_t^3, L_t^4, L_t^5$	4 μH	v_{ref}^4, v_{ref}^5	36 V
f_s^1	40 kHz	k_p^1 / k_i^1	0.01 / 15
f_s^2	60 kHz	k_p^2 / k_i^2	0.01 / 10
f_s^3	75 kHz	k_p^3 / k_i^3	0.01 / 25
f_s^4	100 kHz	k_p^4 / k_i^4	0.001 / 25
f_s^5	90 kHz	k_p^5 / k_i^5	0.005 / 25

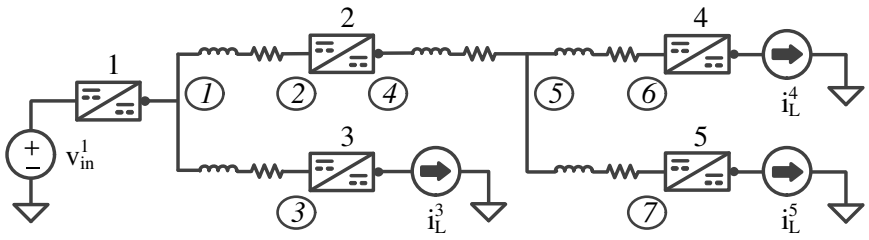

Figure 7. 7-Bus Test System.

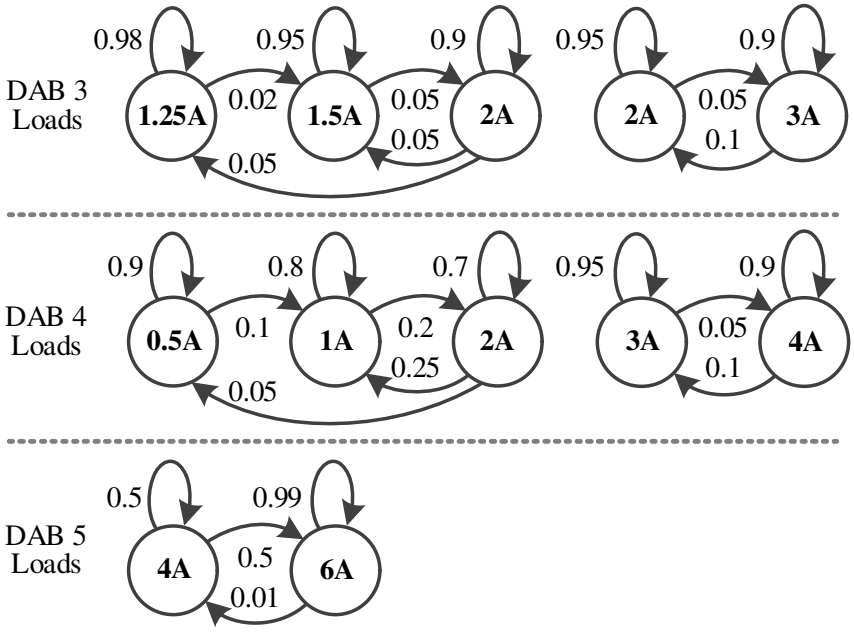

Figure 8. Markov chains for loads in 7-bus system experiments.

Performance is assessed through comparisons of Monte Carlo simulations to predictions from the SHS model. The Monte Carlo analysis consists of 1000 independent simulations of a period of 15 ms. In all cases, the load devices begin mode 1 at $t = 0$ s, corresponding to the leftmost modes of the Markov chains shown in Fig. 8. The system experiences a transient response as the mode occupation probabilities approach the stationary distribution of the CTMC. The simulations use a discrete sample time of 1 μs. Unless otherwise specified, Monte Carlo results are shown as averages over the independent trials on a sample-by-sample basis.

6.1. Moment Dynamics of $X(t)$. The primary function of the SHS model is to accurately predict the dynamics of moments of system state variables. Comparisons of SHS model predictions to moment dynamics obtained from Monte Carlo simulations are shown in Fig. 9 and Fig. 10. First moments are shown in Fig. 9 for selected bus voltage and line current states. Second order moments are shown in Fig. 10. The figures show that the SHS predictions match Monte Carlo simulations both in transient response and steady-state behavior. Similarly matching plots may be shown for all other system state variables.

6.2. Moment Dynamics of ZVS Conditions. In addition to state moment dynamics, the SHS model correctly predicts the evolution of moments of ZVS conditions. This is shown for DAB 3 and 4 in Fig. 11. For these converters, output voltage is always less than input voltage, and the existence of ZVS is therefore governed by $h_d(x,u)$. Fig. 11 shows

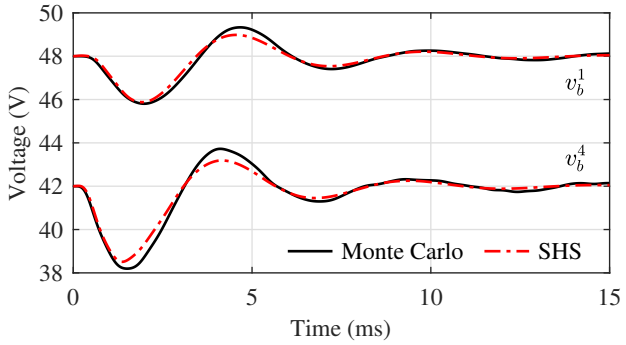

(a) Bus Voltage First Moments

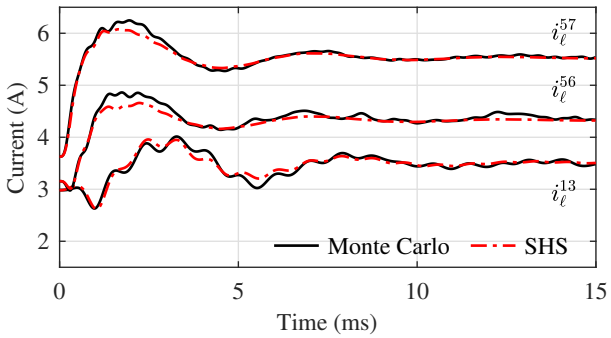

(b) Line Current First Moments

Figure 9. Comparison of first moment dynamics obtained from Monte Carlo simulations to SHS model predictions.

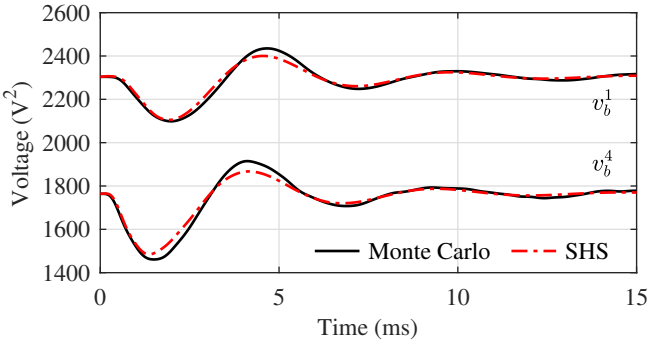

(a) Bus Voltage Second Moments

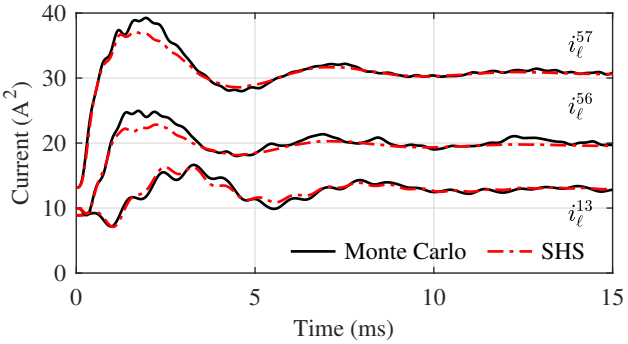

(b) Line Current Second Moments

Figure 10. Comparison of second moment dynamics obtained from Monte Carlo simulations to SHS model predictions.

comparisons of first and second moments of $h_d(x, u)$ observed in Monte Carlo simulations to SHS model predictions. These results indicate that the SHS framework is capable of accurately predicting the moments of nonlinear algebraic functions of system states and inputs.

The purpose of computing moments of ZVS conditions is to obtain approximate bounds on the probability of ZVS. Fig. 12 shows ZVS probability bounds calculated using (77) and (78). The point of comparison in this case is the relative frequency of ZVS in Monte Carlo simulations. For each trial, a sequence of binary variables is defined according to whether ZVS occurs at each time sample. The average of these sequences indicates the relative frequency of ZVS in simulation.

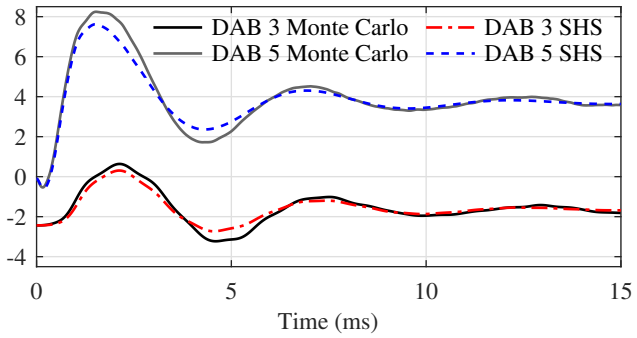

(a) First Moment of $h_d(x, u)$

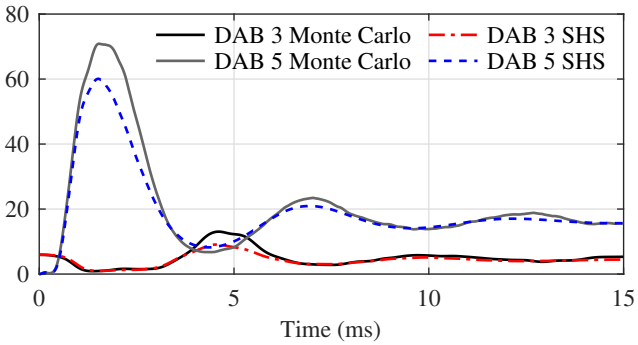

(b) Second Moment of $h_d(x, u)$

Figure 11. Comparison of $\mathbb{E}[h_d(x,u)]$ and $\mathbb{E}\left[(h_d(x,u))^2\right]$ obtained from Monte Carlo simulations to SHS model predictions. Results are shown for converters 3 and 5.

The results in Fig. 12 show that the tightness of the bound varies for each converter. For instance, the upper bound shown in Fig. 12(a) for DAB 3 is loose in comparison to the lower bound for DAB 5, shown in Fig. 12(c). Fig. 11 indicates the reason for this difference. For DAB 3, the first moment of $h_d(x, u)$ is close to zero. As a result, the tail probability assessed in (77) and (78) is a significant fraction of the overall distribution, and the bound given by the Cantelli inequality is conservative. In contrast, the first moment of $h_d(x, u)$ for DAB 5 is further from zero, and the tail probability is more accurately assessed.

6.3. Improving ZVS Performance. In addition to predicting ZVS behavior, the SHS model and ZVS condition functions may be used to improve soft-switching performance. A simple example is given here, in which the proportional gain of a voltage controller is adjusted to maximize the probability of ZVS. Fig. 13 shows the ZVS condition

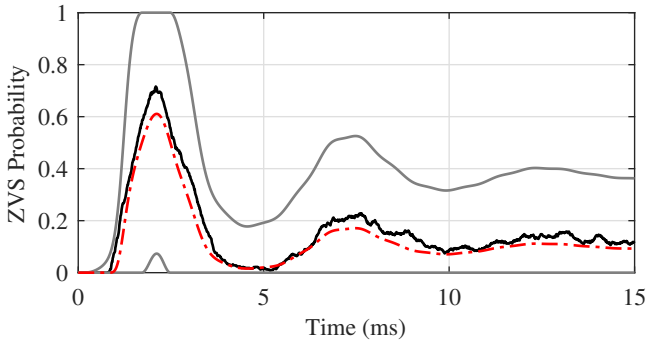

(a) DAB 3 ZVS Probability

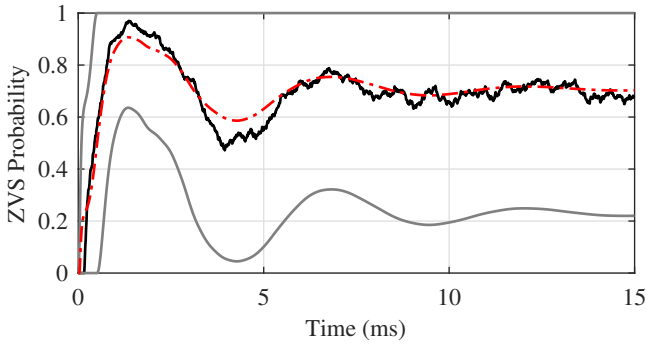

(b) DAB 4 ZVS Probability

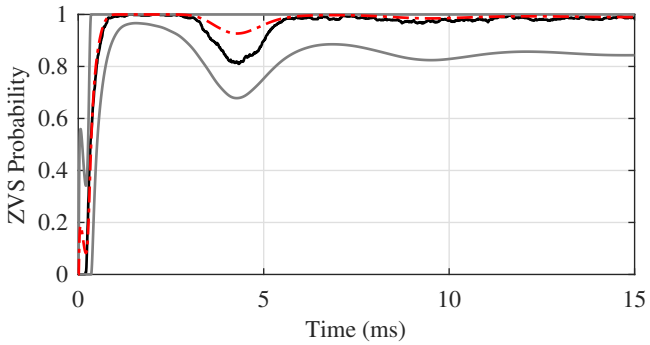

(c) DAB 5 ZVS Probability

Figure 12. Comparison of ZVS probability bounds from SHS to results from Monte Carlo simulations.

equation for a DAB converter in step-down operation. The x and y axes of the plot are phase shift and voltage gain, respectively, and input voltage is assumed constant. This is a simple way of visualizing ZVS limits: ZVS occurs in all operating points above the limit

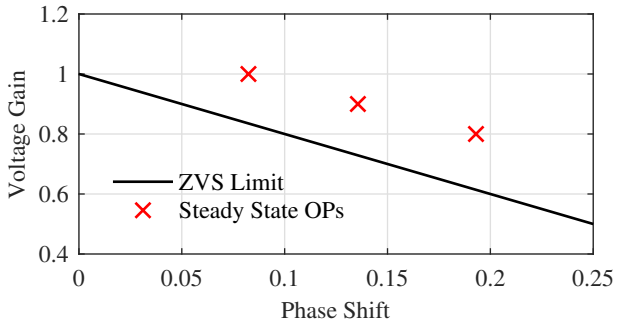

Figure 13. Step-down ZVS limit and operating points for a three-mode load process.

line. Superimposed on the plot are three steady-state operating points which correspond to three modes of a load process. In this case, each mode is characterized by a different voltage reference and load current.

All three operating points are above the converter's ZVS limit. A steady-state analysis would therefore conclude that this converter always experiences ZVS. In practice, however, transient conditions when transitioning between modes cause the converter to exit the ZVS region. The SHS model is capable of identifying this behavior provides a means for mitigating its effect. The objective in this example is to maximize ZVS probability by changing controller gain. The function to be maximized is then

$$F(\xi, k_p) = \frac{(\xi^{(1)}(t))^2}{\xi^{(2)}(t)}. \tag{79}$$

A simple iterative approach to this maximization is steepest descent. Since the proportional gain k_p is to be adjusted, the iteration is

$$k_p = k_p + \epsilon \frac{\partial F(\xi, k_p)}{\partial k_p} \tag{80}$$

where ϵ is the step-size parameter, and is small (10^{-4} in this example). This iteration continues until the derivative term in (80) drops below a predetermined threshold. Fig. 14(a) shows the change in $F(\xi, k_p)$ and k_p over 600 steepest descent iterations. The initial value

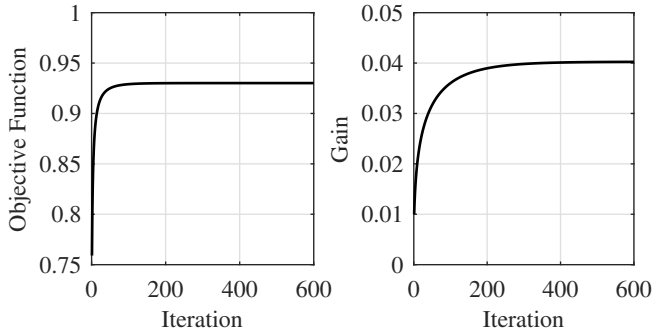

(a) Changes in gain and objective function over 600 iterations

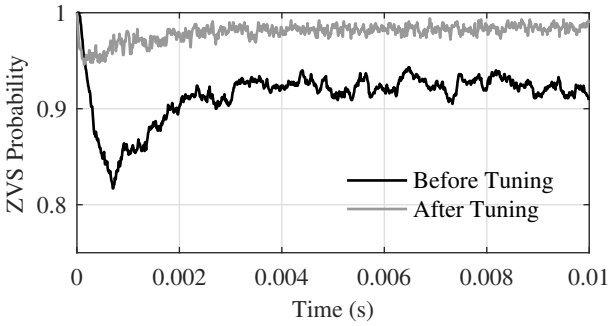

(b) ZVS probability before and after tuning k_p

Figure 14. Maximization of ZVS probability using steepest descent on proportional gain parameter.

of k_p is 0.01; after 600 iterations the gain is $k_p = 0.0402$. Fig. 14(b) shows results of Monte Carlo simulations before and after tuning the controller gain. These results clearly show the improvement in ZVS performance due to the gain adjustments.

7. CONCLUSION

This study presents two contributions. The first is a method of predicting the influence of random load behavior on dc microgrids and distribution systems. At the core of this method is a stochastic process that represents the combined behavior of loads throughout the system. The model that governs load process is constructed from individual device models, which are trained using simple parameter estimation algorithms. Using the

SHS framework, the load process is combined with deterministic system-level models. The resulting SHS model provides the tools necessary to analyze the effects of load behavior on system dynamics.

The second contribution is a method of assessing the probability of ZVS in DAB converters for a given set of load devices. ZVS conditions are encoded as a function of dynamic state moments. Leveraging the functionality of the SHS model, moments of the ZVS condition functions are obtained. These moments are used in Cantelli's inequality to produce a set of bounds on ZVS probability. While the proposed method of ZVS assessment is specific to the DAB topology, it represents an example of how desirable operating conditions may be represented in the SHS model.

REFERENCES

[1] J. P. Hespanha, "Modelling and analysis of stochastic hybrid systems," *IEE Proceedings - Control Theory and Applications*, vol. 153, no. 5, pp. 520–535, 2006.

[2] S. V. Dhople, Y. C. Chen, L. DeVille, and A. D. Domínguez-García, "Analysis of power system dynamics subject to stochastic power injections," *IEEE Trans. Circuits Syst. I*, vol. 60, no. 12, pp. 3341–3353, 2013.

[3] G. Mpembele and J. Kimball, "Analysis of a standalone microgrid stability using generic markov jump linear systems," in *2017 IEEE Power and Energy Conference at Illinois (PECI)*, 2017, pp. 1–8.

[4] G. Hart, "Nonintrusive appliance load monitoring," *Proc. IEEE*, vol. 80, no. 12, pp. 1870–1891, Dec 1992.

[5] F. Sultanem, "Using appliance signatures for monitoring residential loads at meter panel level," *IEEE Trans. Power Del.*, vol. 6, no. 4, pp. 1380–1385, Oct 1991.

[6] A. Zoha, A. Gluhak, M. Nati, and M. Imran, "Low-power appliance monitoring using factorial hidden Markov models," in *IEEE 8th Int.l Conf. Intelligent Sensors, Sensor Networks and Information Processing*, April 2013, pp. 527–532.

[7] T. Zia, D. Bruckner, and A. Zaidi, "A hidden Markov model based procedure for identifying household electric loads," in *37th Conf. Industrial Electronics*, Nov 2011, pp. 3218–3223.

[8] S. Makonin, F. Popowich, I. Bajic, B. Gill, and L. Bartram, "Exploiting hmm sparsity to perform online real-time nonintrusive load monitoring," *IEEE Trans. Smart Grid*, vol. PP, no. 99, pp. 1–11, 2015.

[9] J. A. Mueller and J. W. Kimball, "Accurate energy use estimation for nonintrusive load monitoring in systems of known devices," *IEEE Trans. Smart Grid*, vol. PP, no. 99, pp. 1–1, 2017.

[10] G. Pola, M. L. Bujorianu, J. Lygeros, and M. D. Di Benedetto, "Stochastic hybrid models: An overview," *IFAC Proceedings Volumes*, vol. 36, no. 6, pp. 45–50, 2003.

[11] J. A. Mueller and J. Kimball, "Modeling dual active bridge converters in dc distribution systems," *IEEE Trans. Power Electron.*, 2018.

[12] M. N. Kheraluwala, R. W. Gascoigne, D. M. Divan, and E. D. Baumann, "Performance characterization of a high-power dual active bridge dc-to-dc converter," *IEEE Trans. Ind. Appl.*, vol. 28, no. 6, pp. 1294–1301, 1992.

[13] A. Rodríguez, A. Vázquez, D. G. Lamar, M. M. Hernando, and J. Sebastián, "Different purpose design strategies and techniques to improve the performance of a dual active bridge with phase-shift control," *IEEE Trans. Power Electron.*, vol. 30, no. 2, pp. 790–804, 2015.

[14] R. T. Naayagi, A. J. Forsyth, and R. Shuttleworth, "High-power bidirectional dc-dc converter for aerospace applications," *IEEE Trans. Power Electron.*, vol. 27, no. 11, pp. 4366–4379, 2012.

[15] I. R. Savage, "Probability inequalities of the tchebycheff type," *Journal of Research of the National Bureau of Standards*, vol. 65B, no. 3, pp. 211–226, 1961.

SECTION

2. CONCLUSION

The objective of this dissertation is to provide an accurate modeling framework for dc microgrids and distribution systems. The proposed framework is intended for time-domain simulation, stability assessment, and performance optimization. Systems based on the DAB topology are the primary focus of this research. The challenge of constructing multi-converter system models is managing the tradeoff between accuracy and complexity. This is true regardless of converter topology, but the DAB converter represents an extreme case. Both the algebraic correction factor proposed in Paper I and the harmonic reconstruction of transformer currents in Paper II improve model accuracy without significantly increasing complexity. These improvements are specific to the DAB topology, but may serve to inform similar average model solutions for converters with high-frequency ac conversion stages. The most immediate possible extension is ac-ac DAB converters, for which no accurate large-signal average model has yet been reported.

While aspects of the proposed methodology related to accuracy improvements are specific to the DAB topology, the general model construction strategies are more widely applicable without modification. The system-level model's standardized form and modular construction is specifically intended to facilitate different converter topologies without adjustments to the modeling procedure. The load models in Paper III are similarly extensible. When combined with dynamic models in Paper IV, loads appear as controlled current sources connected to output terminals of dedicated converters. However, this is just one possible configuration. The methodology in Paper IV requires only that the load appear as

an exogenous input in the dynamic model, and is otherwise unaffected by changes in load configuration. The load models could, for example, be used to represent the changes in voltage and current set-points of photovoltaic sources with maximum power point trackers.

Of all the methods and models proposed in this dissertation, the SHS model presents the most abundant avenues for future work. The modeling framework described in Paper IV is intended for analysis and design, but potential applications also exist for online energy management and supervisory control. The SHS model describes conditional moments of dynamic states for each mode of the load process. A subset of the dynamic states are measured during normal operation, i.e. the controlled converter output voltages and internally calculated integrator states. Using conditional moments and empirical observations, it is possible to calculate the likelihood that the load process is in a given mode. If the actual mode of the load process is also known, as in the case of a supervisory controller responsible for scheduling device activity, low values likelihood values may be used to identify problems in device functionality. Paper III suggests a similar fault detection method using the outputs of a NILM algorithm. However, a NILM-based approach is limited to parallel loads at a single location, whereas an SHS-based approach could be used for loads distributed throughout the system.

REFERENCES

[1] A. Q. Huang, M. L. Crow, G. T. Heydt, J. P. Zheng, and S. J. Dale, "The future renewable electric energy delivery and management (freedm) system: The energy internet," *Proc. IEEE*, vol. 99, no. 1, pp. 133–148, 2011.

[2] R. H. Lasseter, "Microgrids," in *2002 IEEE Power Engineering Society Winter Meeting*, vol. 1, 2002, pp. 305–308 vol.1.

[3] S. S. Williamson, A. K. Rathore, and F. Musavi, "Industrial electronics for electric transportation: Current state-of-the-art and future challenges," *IEEE Trans. Ind. Electron.*, vol. 62, no. 5, pp. 3021–3032, 2015.

[4] A. T. Elsayed, A. A. Mohamed, and O. A. Mohammed, "Dc microgrids and distribution systems: An overview," *Electric Power Systems Research*, vol. 119, pp. 407–417, 2015.

[5] T. Dragičević, X. Lu, J. C. Vasquez, and J. M. Guerrero, "Dc microgrids part ii: A review of power architectures, applications, and standardization issues," *IEEE Trans. Power Electron.*, vol. 31, no. 5, pp. 3528–3549, 2016.

[6] M. L. Crow, "Numerical integration," in *Computational Methods for Electric Power Systems*, 3rd ed. Boca Raton, FL: CRC Press, 2016.

[7] P. W. Sauer and M. A. Pai, *Power system dynamics and stability*. Upper Saddle River, N.J.: Prentice Hall, 1998.

[8] R. J. Dirkman, "The simulation of general circuits containing ideal switches," in *1987 IEEE Power Electronics Specialists Conference*, 1987, pp. 185–194.

[9] A. M. Luciano and A. G. M. Strollo, "A fast time-domain algorithm for the simulation of switching power converters," *IEEE Trans. Power Electron.*, vol. 5, no. 3, pp. 363–370, 1990.

[10] D. Bedrosian and J. Vlach, "Time-domain analysis of networks with internally controlled switches," *IEEE Transactions on Circuits and Systems I: Fundamental Theory and Applications*, vol. 39, no. 3, pp. 199–212, 1992.

[11] N. Mohan, W. P. Robbins, T. M. Undeland, R. Nilssen, and O. Mo, "Simulation of power electronic and motion control systems-an overview," *Proc. IEEE*, vol. 82, no. 8, pp. 1287–1302, 1994.

[12] H. N. Chandra and V. J. Thottuvelil, "Modeling and analysis of computer power systems," in *20th Annual IEEE Power Electronics Specialists Conference*, 1989, pp. 144–151 vol.1.

[13] D. Maksimovic, A. M. Stankovic, V. J. Thottuvelil, and G. C. Verghese, "Modeling and simulation of power electronic converters," *Proc. IEEE*, vol. 89, no. 6, pp. 898–912, 2001.

[14] R. W. Erickson, S. Cuk, and R. D. Middlebrook, "Large-signal modelling and analysis of switching regulators," in *1982 IEEE Power Electronics Specialists conference*, 1982, pp. 240–250.

[15] R. D. Middlebrook and S. Cuk, "A general unified approach to modelling switching-converter power stages," in *1976 IEEE Power Electronics Specialists Conference*, 1976, pp. 18–34.

[16] G. W. Wester and R. D. Middlebrook, "Low-frequency characterization of switched dc-dc converters," *IEEE Transactions on Aerospace and Electronic Systems*, vol. AES-9, no. 3, pp. 376–385, 1973.

[17] S. R. Sanders, J. M. Noworolski, X. Z. Liu, and G. C. Verghese, "Generalized averaging method for power conversion circuits," *IEEE Trans. Power Electron.*, vol. 6, no. 2, pp. 251–259, 1991.

[18] B. H. Cho and F. C. Y. Lee, "Modeling and analysis of spacecraft power systems," *IEEE Trans. Power Electron.*, vol. 3, no. 1, pp. 44–54, 1988.

[19] P. T. Krein, J. Bentsman, R. M. Bass, and B. L. Lesieutre, "On the use of averaging for the analysis of power electronic systems," *IEEE Trans. Power Electron.*, vol. 5, no. 2, pp. 182–190, 1990.

[20] K. Zhang, Z. Shan, and J. Jatskevich, "Large- and small-signal average-value modeling of dual-active-bridge dc-dc converter considering power losses," *IEEE Trans. Power Electron.*, vol. 32, no. 3, pp. 1964–1974, 2017.

[21] H. Qin and J. W. Kimball, "Generalized average modeling of dual active bridge dc-dc converter," *IEEE Trans. Power Electron.*, vol. 27, no. 4, pp. 2078–2084, 2012.

[22] R. D. Middlebrook, "Input filter considerations in design and application of switching regulators," in *Rec. IEEE Ind. Appl. Soc. Annu. Meeting*, 1976, pp. 366–382.

[23] A. Riccobono and E. Santi, "Comprehensive review of stability criteria for dc power distribution systems," *IEEE Trans. Ind. Appl.*, vol. 50, no. 5, pp. 3525–3535, 2014.

[24] C. M. Wildrick, F. C. Lee, B. H. Cho, and B. Choi, "A method of defining the load impedance specification for a stable distributed power system," *IEEE Trans. Power Electron.*, vol. 10, no. 3, pp. 280–285, 1995.

[25] X. Feng, J. Liu, and F. C. Lee, "Impedance specifications for stable dc distributed power systems," *IEEE Trans. Power Electron.*, vol. 17, no. 2, pp. 157–162, 2002.

[26] F. Liu, J. Liu, H. Zhang, and D. Xue, "Generalized stability criterion for multi-module distributed dc system," *Journal of Power Electronics*, vol. 1, no. 1, 2014.

[27] X. Zhang, X. Ruan, and C. K. Tse, "Impedance-based local stability criterion for dc distributed power systems," *IEEE Trans. Circuits Syst. I*, vol. 62, no. 3, pp. 916–925, 2015.

[28] J. A. Mueller and J. W. Kimball, "Model-based determination of closed-loop input impedance for dual active bridge converters," in *2017 IEEE Applied Power Electronics Conference and Exposition (APEC)*, March 2017, pp. 1039–1046.

[29] P. Kundur, N. J. Balu, and M. G. Lauby, *Power system stability and control*, ser. EPRI power system engineering series. New York: McGraw-Hill, 1994.

[30] R. W. A. A. DeDoncker, D. M. Divan, and M. H. Kheraluwala, "A three-phase soft-switched high-power-density dc/dc converter for high-power applications," *IEEE Trans. Ind. Appl.*, vol. 27, no. 1, pp. 63–73, 1991.

[31] M. N. Kheraluwala, R. W. Gascoigne, D. M. Divan, and E. D. Baumann, "Performance characterization of a high-power dual active bridge dc-to-dc converter," *IEEE Trans. Ind. Appl.*, vol. 28, no. 6, pp. 1294–1301, 1992.

[32] B. Zhao, Q. Song, W. Liu, and Y. Sun, "Overview of dual-active-bridge isolated bidirectional dc-dc converter for high-frequency-link power-conversion system," *IEEE Trans. Power Electron.*, vol. 29, no. 8, pp. 4091–4106, 2014.

[33] A. K. Jain and R. Ayyanar, "Pwm control of dual active bridge: Comprehensive analysis and experimental verification," *IEEE Trans. Power Electron.*, vol. 26, no. 4, pp. 1215–1227, 2011.

[34] H. Bai and C. Mi, "Eliminate reactive power and increase system efficiency of isolated bidirectional dual-active-bridge dc-dc converters using novel dual-phase-shift control," *IEEE Trans. Power Electron.*, vol. 23, no. 6, pp. 2905–2914, 2008.

[35] B. Zhao, Q. Yu, and W. Sun, "Extended-phase-shift control of isolated bidirectional dc-dc converter for power distribution in microgrid," *IEEE Trans. Power Electron.*, vol. 27, no. 11, pp. 4667–4680, 2012.

[36] J. Huang, Y. Wang, Z. Li, and W. Lei, "Unified triple-phase-shift control to minimize current stress and achieve full soft-switching of isolated bidirectional dc-dc converter," *IEEE Trans. Ind. Electron.*, vol. 63, no. 7, pp. 4169–4179, 2016.

[37] R. T. Naayagi, A. J. Forsyth, and R. Shuttleworth, "High-power bidirectional dc-dc converter for aerospace applications," *IEEE Trans. Power Electron.*, vol. 27, no. 11, pp. 4366–4379, 2012.

[38] F. Krismer and J. W. Kolar, "Accurate small-signal model for the digital control of an automotive bidirectional dual active bridge," *IEEE Trans. Power Electron.*, vol. 24, no. 12, pp. 2756–2768, 2009.

[39] B. Zahedi and L. E. Norum, "Modeling and simulation of all-electric ships with low-voltage dc hybrid power systems," *IEEE Trans. Power Electron.*, vol. 28, no. 10, pp. 4525–4537, 2013.

[40] I. Y. Chung, W. Liu, M. Andrus, K. Schoder, L. Siyu, D. A. Cartes, and M. Steurer, "Integration of a bi-directional dc-dc converter model into a large-scale system simulation of a shipboard mvdc power system," in *2009 IEEE Electric Ship Technologies Symposium*, 2009, pp. 318–325.

[41] S. Inoue and H. Akagi, "A bidirectional isolated dc-dc converter as a core circuit of the next-generation medium-voltage power conversion system," *IEEE Trans. Power Electron.*, vol. 22, no. 2, pp. 535–542, 2007.

[42] A. Q. Huang, "Medium-voltage solid-state transformer: Technology for a smarter and resilient grid," *IEEE Ind. Electron. Mag.*, vol. 10, no. 3, pp. 29–42, 2016.

[43] X. She, A. Q. Huang, and R. Burgos, "Review of solid-state transformer technologies and their application in power distribution systems," *IEEE J. Emerg. Sel. Topics Power Electron.*, vol. 1, no. 3, pp. 186–198, 2013.

[44] H. Qin and J. W. Kimball, "Solid-state transformer architecture using ac-ac dual-active-bridge converter," *IEEE Trans. Ind. Electron.*, vol. 60, no. 9, pp. 3720–3730, 2013.

[45] R. W. Erickson and D. Maksimovic, *Fundamentals of power electronics*, 2nd ed. Norwell, Mass.: Kluwer Academic, 2001.

[46] S. Bacha, I. Munteanu, and A. I. Bratcu, *Power electronic converters modeling and control: with case studies*, ser. Advanced Textbooks in Control and Signal Processing. London: Springer, 2014.

[47] B. Hua, M. Chunting, W. Chongwu, and S. Gargies, "The dynamic model and hybrid phase-shift control of a dual-active-bridge converter," in *2008 34th Annual Conference of IEEE Industrial Electronics*, 2008, pp. 2840–2845.

[48] G. C. Verghese, M. E. Elbuluk, and J. G. Kassakian, "A general approach to sampled-data modeling for power electronic circuits," *IEEE Trans. Power Electron.*, vol. PE-1, no. 2, pp. 76–89, 1986.

[49] C. Zhao, S. D. Round, and J. W. Kolar, "Full-order averaging modelling of zero-voltage-switching phase-shift bidirectional dc-dc converters," *IET Power Electronics*, vol. 3, no. 3, pp. 400–410, 2010.

[50] L. Shi, W. Lei, Z. Li, J. Huang, Y. Cui, and Y. Wang, "Bilinear discrete-time modeling and stability analysis of the digitally controlled dual active bridge converter," *IEEE Trans. Power Electron.*, vol. 32, no. 11, pp. 8787–8799, 2017.

[51] J. Mahdavi, A. Emaadi, M. D. Bellar, and M. Ehsani, "Analysis of power electronic converters using the generalized state-space averaging approach," *IEEE Transactions on Circuits and Systems I: Fundamental Theory and Applications*, vol. 44, no. 8, pp. 767–770, 1997.

[52] V. A. Caliskan, O. C. Verghese, and A. M. Stankovic, "Multifrequency averaging of dc/dc converters," *IEEE Trans. Power Electron.*, vol. 14, no. 1, pp. 124–133, 1999.

[53] S. S. Shah and S. Bhattacharya, "Large & small signal modeling of dual active bridge converter using improved first harmonic approximation," in *2017 IEEE Applied Power Electronics Conference and Exposition (APEC)*, 2017, pp. 1175–1182.

[54] A. Emadi, "Modeling and analysis of multiconverter dc power electronic systems using the generalized state-space averaging method," *IEEE Trans. Ind. Electron.*, vol. 51, no. 3, pp. 661–668, 2004.

[55] A. Frances, R. Asensi, O. Garcia, R. Prieto, and J. Uceda, "Modeling electronic power converters in smart dc microgrids - an overview," *IEEE Trans. Smart Grid*, vol. PP, no. 99, pp. 1–1, 2017.

[56] P. Shamsi and B. Fahimi, "Stability assessment of a dc distribution network in a hybrid micro-grid application," *IEEE Trans. Smart Grid*, vol. 5, no. 5, pp. 2527–2534, 2014.

[57] J. A. Mueller and J. W. Kimball, "Generalized average modeling of dc subsystem in solid state transformers," in *2017 IEEE Energy Conversion Congress and Exposition (ECCE)*, October 2017.

[58] G. Gross and F. D. Galiana, "Short-term load forecasting," *Proc. IEEE*, vol. 75, no. 12, pp. 1558–1573, 1987.

[59] M. T. Hagan and S. M. Behr, "The time series approach to short term load forecasting," *IEEE Trans. Power Syst.*, vol. 2, no. 3, pp. 785–791, 1987.

[60] G. E. P. Box, G. M. Jenkins, G. C. Reinsel, and G. M. Ljung, *Time Series Analysis: Forecasting and Control*, 5th ed. Hoboken, NJ: John Wiley & Sons, Inc., 2016.

[61] A. Marinescu, C. Harris, I. Dusparic, S. Clarke, and V. Cahill, "Residential electrical demand forecasting in very small scale: An evaluation of forecasting methods," in *2013 2nd International Workshop on Software Engineering Challenges for the Smart Grid (SE4SG)*, 2013, pp. 25–32.

[62] G. Hart, "Nonintrusive appliance load monitoring," *Proc. IEEE*, vol. 80, no. 12, pp. 1870–1891, Dec 1992.

[63] Y. F. Wong, Y. Ahmet Sekercioglu, T. Drummond, and V. S. Wong, "Recent approaches to non-intrusive load monitoring techniques in residential settings," in *IEEE Symp. Computational Intelligence Applications In Smart Grid (CIASG)*, April 2013, pp. 73–79.

[64] Y. Du, L. Du, B. Lu, R. Harley, and T. Habetler, "A review of identification and monitoring methods for electric loads in commercial and residential buildings," in *Energy Conversion Congress and Exposition (ECCE), 2010 IEEE*, Sept 2010, pp. 4527–4533.

[65] H. Kim, M. Marwah, M. Arlitt, G. Lyon, and J. Han, "Unsupervised disaggregation of low frequency power measurements," in *SDM*, vol. 11, 2011, pp. 747–758.

[66] T. Zia, D. Bruckner, and A. Zaidi, "A hidden Markov model based procedure for identifying household electric loads," in *37th Conf. Industrial Electronics*, Nov 2011, pp. 3218–3223.

[67] O. Parson, S. Ghosh, M. Weal, and A. Rogers, "Non-intrusive load monitoring using prior models of general appliance types," in *26th Conference on Artificial Intelligence*, vol. 22, 2012, pp. 356–362.

[68] J. Liao, G. Elafoudi, L. Stankovic, and V. Stankovic, "Non-intrusive appliance load monitoring using low-resolution smart meter data," in *IEEE Int.l Conf. Smart Grid Communications (SmartGridComm)*, Nov 2014, pp. 535–540.

[69] S. Makonin, F. Popowich, I. Bajic, B. Gill, and L. Bartram, "Exploiting hmm sparsity to perform online real-time nonintrusive load monitoring," *IEEE Trans. Smart Grid*, vol. PP, no. 99, pp. 1–11, 2015.

[70] A. Papoulis, *Probability, random variables, and stochastic processes*, 3rd ed., ser. McGraw-Hill series in electrical engineering Communications and signal processing. New York: McGraw-Hill, 1991.

[71] J. P. Hespanha, "Modelling and analysis of stochastic hybrid systems," *IEE Proceedings - Control Theory and Applications*, vol. 153, no. 5, pp. 520–535, 2006.

[72] A. R. Teel, A. Subbaraman, and A. Sferlazza, "Stability analysis for stochastic hybrid systems: A survey," *Automatica*, vol. 50, no. 10, pp. 2435–2456, 2014.

[73] S. V. Dhople, Y. C. Chen, L. DeVille, and A. D. Domínguez-García, "Analysis of power system dynamics subject to stochastic power injections," *IEEE Trans. Circuits Syst. I*, vol. 60, no. 12, pp. 3341–3353, 2013.

[74] M. Střelec, K. Macek, and A. Abate, "Modeling and simulation of a microgrid as a stochastic hybrid system," in *2012 3rd IEEE PES Innovative Smart Grid Technologies Europe (ISGT Europe)*, 2012, pp. 1–9.

[75] G. Mpembele and J. Kimball, "Analysis of a standalone microgrid stability using generic markov jump linear systems," in *2017 IEEE Power and Energy Conference at Illinois (PECI)*, 2017, pp. 1–8.

[76] A. Rodríguez, A. Vázquez, D. G. Lamar, M. M. Hernando, and J. Sebastián, "Different purpose design strategies and techniques to improve the performance of a dual active bridge with phase-shift control," *IEEE Trans. Power Electron.*, vol. 30, no. 2, pp. 790–804, 2015.

[77] F. Zhang, M. M. U. Rehman, R. Zane, and D. Maksimović, "Improved steady-state model of the dual-active-bridge converter," in *2015 IEEE Energy Conversion Congress and Exposition (ECCE)*, 2015, pp. 630–636.

[78] S. Cooper, A. Klem, M. H. Nehrir, and H. Ga, "An improved state-space averaged model of a dual active bridge converter for use in acausal system modeling," in *2016 North American Power Symposium (NAPS)*, 2016, pp. 1–5.

[79] B. Zhao, Q. Song, and W. Liu, "Power characterization of isolated bidirectional dual-active-bridge dc-dc converter with dual-phase-shift control," *IEEE Trans. Power Electron.*, vol. 27, no. 9, pp. 4172–4176, 2012.

[80] D. Gonzalez-Agudelo, A. Escobar-Mejía, and H. Ramirez-Murrillo, "Dynamic model of a dual active bridge suitable for solid state transformers," in *2016 13th International Conference on Power Electronics (CIEP)*, 2016, pp. 350–355.

[81] B. Zhao, Q. Song, W. Liu, and Y. Sun, "Dead-time effect of the high-frequency isolated bidirectional full-bridge dc-dc converter: Comprehensive theoretical analysis and experimental verification," *IEEE Trans. Power Electron.*, vol. 29, no. 4, pp. 1667–1680, 2014.

[82] D. Segaran, D. G. Holmes, and B. P. McGrath, "Enhanced load step response for a bidirectional dc-dc converter," *IEEE Trans. Power Electron.*, vol. 28, no. 1, pp. 371–379, 2013.

[83] J. A. Mueller and J. Kimball, "An improved generalized average model of dc-dc dual active bridge converters," *IEEE Trans. Power Electron.*, vol. PP, no. 99, pp. 1–1, 2018.

[84] Z. Wang and G. Zheng, "Residential appliances identification and monitoring by a nonintrusive method," *IEEE Trans. Smart Grid*, vol. 3, no. 1, pp. 80–92, March 2012.

[85] D. He, W. Lin, N. Liu, R. Harley, and T. Habetler, "Incorporating non-intrusive load monitoring into building level demand response," *IEEE Trans. Smart Grid*, vol. 4, no. 4, pp. 1870–1877, Dec 2013.

[86] M. Zeifman and K. Roth, "Nonintrusive appliance load monitoring: Review and outlook," *IEEE Trans. Consum. Electron.*, vol. 57, no. 1, pp. 76–84, February 2011.

[87] C. Laughman *et al.*, "Power signature analysis," *IEEE Power Energy Mag.*, vol. 1, no. 2, pp. 56–63, Mar 2003.

[88] M. Berges, E. Goldman, H. S. Matthews, L. Soibelman, and K. Anderson, "User-centered nonintrusive electricity load monitoring for residential buildings," *J. Comput. Civ. Eng.*, vol. 25, no. 6, pp. 471–480, May 2011.

[89] L. Rabiner, "A tutorial on hidden Markov models and selected applications in speech recognition," *Proc. IEEE*, vol. 77, no. 2, pp. 257–286, Feb 1989.

[90] J. Z. Kolter and T. Jaakkola, "Approximate inference in additive factorial HMMs with application to energy disaggregation," in *Proc. 15th Int. Conf. Artificial Intelligence and Statistics*, vol. 22, 2012, pp. 1472–1482.

[91] J. A. Mueller and J. W. Kimball, "An accurate method of energy use prediction for systems with known composition," in *Proc. 3rd. Int. Workshop on Nonintrusive Load Monitoring*, May 2016.

[92] Z. Ghahramani, "An introduction to hidden Markov models and bayesian networks," *Int. J. Pattern Recognition and Artificial Intell.*, vol. 15, no. 1, pp. 9–42, Jun. 2001.

[93] A. Zoha, A. Gluhak, M. Nati, and M. Imran, "Low-power appliance monitoring using factorial hidden Markov models," in *IEEE 8th Int.l Conf. Intelligent Sensors, Sensor Networks and Information Processing*, April 2013, pp. 527–532.

[94] L. Wang, X. Luo, and W. Zhang, "Unsupervised energy disaggregation with factorial hidden Markov models based on generalized backfitting algorithm," in *Proc. IEEE Region 10 Conf.*, Oct 2013, pp. 1–4.

[95] Z. Ghahramani and M. I. Jordan, "Factorial hidden Markov models," *Mach. Learn.*, vol. 29, no. 2-3, pp. 245–273, Nov. 1997.

[96] J. Z. Kolter and M. J. Johnson, "REDD: A Public Data Set for Energy Disaggregation Research," in *Proc. 2011 Workshop on Data Mining Applications in Sustainability (SustKDD 2011)*, Aug 2011.

[97] M. Zeifman and K. Roth, "Viterbi algorithm with sparse transitions (vast) for nonintrusive load monitoring," in *Computational Intelligence Applications In Smart Grid (CIASG), 2011 IEEE Symposium on*, April 2011, pp. 1–8.

[98] S. Makonin, F. Popowich, and I. Bajic, "Efficient matrix processing for nonintrusive load monitoring (NILM)," in *Proc. 2nd. Int. Workshop on Nonintrusive Load Monitoring*, June 2014.

[99] J. Forney, G.D., "The Viterbi algorithm," *Proc. IEEE*, vol. 61, no. 3, pp. 268–278, March 1973.

[100] C. Beckel, W. Kleiminger, R. Cicchetti, T. Staake, and S. Santini, "The ECO data set and the performance of non-intrusive load monitoring algorithms," in *Proc. 1st ACM Int.l Conf. Embedded Systems for Energy-Efficient Buildings (BuildSys 2014)*, Nov 2014, pp. 80–89.

[101] S. Barker *et al.*, "Smart*: An open data set and tools for enabling research in sustainable homes," in *Proc. 2012 Workshop on Data Mining Applications in Sustainability (SustKDD 2012)*, Aug 2012.

[102] A. Monacchi, D. Egarter, W. Elmenreich, S. D'Alessandro, and A. Tonello, "GREEND: An energy consumption dataset of households in Italy and Austria," in *IEEE Int. Conf. Smart Grid Communications (SmartGridComm)*, Nov 2014, pp. 511–516.

[103] S. Makonin and F. Popowich, "Nonintrusive load monitoring (NILM) performance evaluation," *Energy Efficiency*, vol. 8, no. 4, pp. 809–814, 2014.

[104] F. Sultanem, "Using appliance signatures for monitoring residential loads at meter panel level," *IEEE Trans. Power Del.*, vol. 6, no. 4, pp. 1380–1385, Oct 1991.

[105] J. A. Mueller and J. W. Kimball, "Accurate energy use estimation for nonintrusive load monitoring in systems of known devices," *IEEE Trans. Smart Grid*, vol. PP, no. 99, pp. 1–1, 2017.

[106] G. Pola, M. L. Bujorianu, J. Lygeros, and M. D. Di Benedetto, "Stochastic hybrid models: An overview," *IFAC Proceedings Volumes*, vol. 36, no. 6, pp. 45–50, 2003.

[107] J. A. Mueller and J. Kimball, "Modeling dual active bridge converters in dc distribution systems," *IEEE Trans. Power Electron.*, 2018.

[108] I. R. Savage, "Probability inequalities of the tchebycheff type," *Journal of Research of the National Bureau of Standards*, vol. 65B, no. 3, pp. 211–226, 1961.

VITA

Jacob Andreas Mueller was born and raised in St. Louis, Missouri. In December 2012, he received BS degrees in Electrical and Computer Engineering from Missouri University of Science and Technology. He received the MS and PhD degrees in Electrical Engineering from Missouri S&T in December 2014 and May 2018, respectively. Following the completion of his PhD he joined Sandia National Laboratories as a postdoctoral appointee in the Energy Storage Technology and Systems Department.